# On-Surface Chemistry of Organometallic Complexes

---

Dissertation

zur

Erlangung der naturwissenschaftlichen Doktorwürde
(Dr. sc. nat.)

vorgelegt der

Mathematisch-naturwissenschaftlichen Fakultät

der

Universität Zürich

von

**Alexandra H. Rieger**

aus

Fischenthal ZH

Promotionskommission

Prof. Dr. Karl-Heinz Ernst (Vorsitz)

Prof. Dr. Roger Alberto

Prof. Dr. Greta Patzke

Zürich, 2018

“Think critically about what you are told. Do not accept the word of authority unthinkingly. Science is not a belief system: no belief system instructs you to question the system itself. Science does. (There are many scientists, however, who treat it as a belief system. Be wary of them.)”
— Sir Terry Pratchett, The Science of Discworld II: The Globe

# 1 Abstract

Reactions involving organic molecules at inorganic interfaces are of increasing importance for organic light emitting diodes (OLEDs), organic solar cells and catalytic coupling reactions allowing for the fabrication of novel materials. In these applications the reactive organic molecules are in contact with an inorganic substrate, e.g. a metal substrate and may undergo chemical reactions with the substrate or may undergo chemical reactions on the substrate. In the second case the metallic substrate often acts as catalyst facilitating reactions between the adsorbed molecules. It is therefore essential to further the knowledge about the metal-organic interactions. The best way to study metal-organic interactions is on a clean and well defined single crystalline surface in vacuum, where contaminations such as e.g. adsorbates on the metal surface are ruled out. And in contrast to a solution, in vacuum no ligand coordination through solvatisation occurs. Therefore, working in vacuum on a metal surface facilitates the understanding of the metal-organic interactions.

The methods of choice in this thesis to investigate metal-organic reactions on a single crystalline flat surface in ultra-high vacuum (UHV) are X-ray photoelectron spectroscopy (XPS) and the related technique of X-ray photoelectron diffraction (XPD), scanning tunnelling microscopy (STM) and thermal desorption spectroscopy (TDS). XPS gives information on the adsorbed species and their chemical environment, XPD gives structural information, STM is an imaging technique that maps the electron density on the surface and in TDS the evolution of masses over time during the heating-up of the sample is monitored.

The first part of the thesis focusses on the coordination of a metal ion into an organic macrocycle, so-called pyrphyrin which is similar to porphyrin. By metal coordination the chemical reactions of pyrphyrin can be controlled. Upon annealing pyrphyrin loses its two cyano groups in the form of HCN. This reaction can be suppressed by coordination of Fe prior to the annealing step. Furthermore, it is investigated if the coordinated metal centres can be exchanged with other metal ions and if a hierarchical order of stability can be established between metal coordinating complexes. Such metal centre exchange reactions are often observed in solution, but on surfaces no convincing studies of metal centre exchange reaction exists. The results presented in this thesis are that Cu ions coordinated by pyrphyrin can be exchanged with Ni ions which in turn can be exchanged by Fe ions. The reverse reactions do not occur.

The second part of the thesis focusses on the binding of an oxygen-rich organic molecule, tartaric acid, to a metal surface. Tartaric acid occurs in different diastereomers: the chiral enantiomers, the achiral diastereomer and the racemic mixture of the chiral enantiomers.

It is investigated how the geometry of the metal surface impacts on the adsorption and desorption properties of tartaric acid. Depending on the geometry of the metal surface all the diastereomers desorb at the same temperature or the racemic mixture desorbs at a lower temperature than the chiral enantiomers. Furthermore, it is investigated how the adsorption of chiral tartaric acid imprints its chirality onto the top layer of the copper surface. These results remain inconclusive as to whether the effect of the chiral imprinting is present. Therefore, more experiments need to be undertaken.

# 2 Zusammenfassung

Reaktionen, die organische Moleküle an Grenzflächen beinhalten, werden immer wichtiger für organische licht-emittierende Dioden (OLEDs), organische Solarzellen und katalytische Kupplungsreaktionen, die die Erschaffung von neuen Materialien ermöglichen. In diesen Anwendungen kommen die reaktiven organischen Moleküle in Kontakt mit dem anorganischen Substrat, beispielsweise dem Metallsubstrat und können mit oder auf dem Substrat reagieren. Im zweiten Falle agiert das metallische Substrat als Katalysator, der die chemischen Reaktionen zwischen den adsorbierten Molekülen vereinfacht. Es ist daher ganz wichtig das Wissen über die metall-organischen Wechselwirkungen auszuweiten. Die beste Art und Weise wie solche metall-organischen Wechselwirkungen untersucht werden können, ist auf einer sauberen und wohl-definierten Einkristalloberfläche im Vakuum, wo Kontaminationen beispielsweise durch adsorbierte Stoffe auf der Metalloberfläche ausgeschlossen werden können. Und im Gegensatz zur Lösung gibt es im Vakuum keine Ligandenkoordination durch Solvatation. Deshalb ist es einfacher die metall-organischen Wechselwirkungen auf einer Metalloberfläche im Vakuum zu untersuchen und zu verstehen.

Die Methoden der Wahl in dieser Doktorarbeit, um die metall-organischen Reaktionen auf einer flachen Einkristalloberfläche im Ultrahochvakuum (UHV) zu untersuchen sind: Röntgenphotoelektronenspektroskopie (XPS) und die damit verwandte Methode der Röntgenphotoelektronenbeugung (XPD), Rastertunnelmikroskopie (STM) und die thermische Desorptionsspektroskopie (TDS). XPS gibt Informationen über die adsorbierten Atome und Moleküle und ihre chemische Umgebung. XPD gibt Informationen über die Strukur. STM ist eine bildgebende Technik, welche die Verteilung der Elektronendichte auf der Oberfläche abbildet und mit TDS kann die Evolution der Massen über die Zeit hinweg während dem Aufwärmen der Probe überwacht werden.

Im ersten Teil dieser Doktorarbeit wird der Fokus auf die Koordination eines Metallions in einen organischen Makrozyklus gelegt, dem sogenannten Pyrphyrin, welches dem Porphyrin ähnlich ist. Durch die Koordination des Metalls können die chemischen Reaktionen von Pyrphyrin kontrolliert werden. Beim aufheizen verliert Pyrphyrin seine zwei Cyanogruppen als HCN. Diese Reaktion kann unterdrückt werden durch die Koordination eines Fe Atoms vor dem Aufheizen. Darüber hinaus wurde untersucht, ob die koordinierten Metallzentren durch andere Metallionen ausgetauscht werden können und ob eine Rangordnung der Stabilität zwischen den metallkoordinierten Komplexen gibt. Solche Austauschreaktionen der Metallzentren wurden häufig beobachtet in Lösung, aber auf Oberflächen gibt es bis jetzt keine überzeugenden Studien solcher Reaktionen. Die hier präsentierten Resultate sind, dass Cu Ionen, die von Pyrphyrin koordiniert sind, von Ni Ionen ausgetauscht werden können und diese wiederum können von Fe Ionen ausgetauscht werden. Die umgekehrten Reaktionen finden nicht statt.

Im zweiten Teil dieser Doktorarbeit liegt der Fokus auf der Bindung eines sauerstoffreichen organischen Moleküls, der Weinsäure, zur Metalloberfläche. Die Weinsäure kann in der Form von verschiedenen Diastereomeren vorliegen: als chirale Enantiomere, als achirales Diastereomer und als razemische Mischung der chiralen Enantiomere.

Die Auswirkung der Geometrie der Metalloberfläche auf die Adsorptions- und Desorptionseigenschaften der Weinsäure wurde untersucht. Je nach Geometrie der Metalloberfläche desorbieren alle Diastereomere bei der gleichen Temperatur oder die razemische Mischung desorbiert bei einer tieferen Temperatur als die chiralen Enantiomere. Des Weiteren wurde untersucht ob durch die Adsorption der Weinsäure ihre Chiralität auf die oberste Schicht der Kupferoberfläche geprägt werden kann. Die Resultate dieser Untersuchung sind unklar, ob der Effekt der chiralen Prägung gemessen wurden oder nicht. Um das zu klären müssen weitere Experimente durchgeführt werden.

# 3 Table of Content

1 Abstract ........ iv

2 Zusammenfassung ........ vi

4 Introduction ........ 1

4.1 Central metal exchange and metalation induced chemistry in surface adsorbed macrocycles ........ 2

4.2 Interaction between metal surface and organic molecule ........ 4

5 Experimental ........ 7

5.1 Sample preparation in UHV ........ 7

5.2 X-ray Photoelectron Spectroscopy ........ 7

5.3 X-ray Photoelectron Diffraction ........ 8

5.4 Scanning-Tunneling Microscopy ........ 10

5.5 Thermal Desorption Spectroscopy ........ 11

5.6 Reflection absorption infrared spectroscopy ........ 11

6 Controlled Decyanisation Reaction of Pyrphyrin on Ag(111) ........ 12

6.1 Results and Discussion ........ 13

6.1.1 Annealing without Fe ........ 13

6.1.2 Annealing in the presence of Fe ........ 18

6.1.3 Identification of desorption products by TDS ........ 24

6.2 Discussion ........ 25

6.3 Conclusion and Outlook ........ 27

7 Metal Centre Exchange in Surface-adsorbed macrocycles ........ 29

7.1 Results and Discussion ........ 31

7.1.1 Cu to Fe exchange ........ 32

7.1.2 Cu to Ni exchange ........ 34

7.1.3 Potentially occurring reverse reactions ........ 36

7.1.4 Ni to Fe exchange ........ 37

7.1.5 Direct metalation from 2HPyr to NiPyr and FePyr ..... 41
7.2 Conclusion and Outlook ..... 42
8 Tartaric Acid Diastereomers on Cu(111) ..... 44
8.1 Results and Discussion ..... 46
8.1.1 Adsorption of TA on Cu(111) at room temperature ..... 46
8.1.2 Adsorption of TA on Cu(111) at elevated temperature ..... 52
8.1.3 XPS analysis of TA diastereomers on Cu(111) ..... 54
8.1.4 Desorption of TA diastereomers from Cu(111) ..... 57
8.2 Conclusion and Outlook ..... 61
9 XPD Study on Tartaric Acid on Cu(110) ..... 62
9.1 Theoretical consideration ..... 62
9.2 Experimental consideration ..... 64
9.3 Results and Discussion ..... 65
9.3.1 XPS on (*S*,*S*)-TA and (*R*,*R*)-TA ..... 65
9.3.2 XPD on (*S*,*S*)-TA and (*R*,*R*)-TA ..... 68
9.3.3 Discussion ..... 70
9.4 Conclusion and Outlook ..... 71
10 Summary and Outlook ..... 73
11 References ..... 76
12 Appendix ..... 84
13 List of Publications ..... 86
14 Curriculum Vitae ..... 87
15 Acknowledgements ..... 89

# 4 Introduction

In the past decades, various applications using organic molecules such as OLEDs [1–3], solar cells [4–6] were developed and investigations on many different coupling reactions were continued. One example for such a coupling reaction involving organic molecules and metals is the Ullmann coupling [7–9].

In many applications such as OLEDs and solar cells, and even in catalysis, the organic molecules come in contact with metals, *e.g.* with electrodes. Metals in devices are either used for electrical transport or as the cage in which the reaction takes place. Therefore, a metal-organic interface exists. It is important to know how the organic molecules influence the metals and how the metals influence the organic molecules at these interfaces to prevent parasitic reactions and to increase the reaction output.

Sn nanoparticle batteries are a good example of how parasitic reactions at the metal-organic interface can become a problem [10]: The organic electrolyte fluoroethylene carbonate decomposes on the Sn nanoparticles due to potential differences and forms a patina through which the $Li^+$ ions have to diffuse to be incorporated into the Sn nanoparticles upon charging of the battery. Due to the uptake of $Li^+$ ions the Sn nanoparticle size increases by up to 400%. More of the electrolyte decomposes on the newly exposed Sn nanoparticle surface and the patina becomes thicker [11]. After more than 100 charging cycles the patina at the metal-organic interface is so thick that the $Li^+$ ions have difficulty diffusing through it and thus the capacity of the battery decreases [12]. A solution to this problem could be to cage the Sn nanoparticles into a carbon frame where the metal nanoparticle does not come in direct contact to the organic electrolyte [13].

Reactions of organic molecules on metal surfaces can also be a route to new interface materials. An emerging field of such reactions at the organic/metal interface is covalent polymerisation, leading for example to graphene nanoribbons [14,15]. These nanoribbons are predicted to have interesting electrical properties for the fabrication of nanoscale electronic devices. Cai et al. [14] found a bottom up way of fabricating nanoribbons of precise topologies and widths. By thermal activation of a dibromo-bianthryl precursor a bi-radical is formed. This bi-radical undergoes C-C coupling with another bi-radical molecule on the surface. In a second thermal activation step the linear polymer undergoes cyclodehydrogenation that produces an extended aromatic system, the nanoribbon. This formation of nanoribbons is catalysed by the surface.

Principles of interactions between metals and organic molecules are best studied in vacuum. In ultra-high vacuum (UHV) the possibility of side-reactions that an organic molecule can undergo is very limited as in vacuum reactive gases and materials such as oxygen, water or carbon monoxide are not present. Usually, reactions in UHV are carried out on a metal surface of a single crystal. These surfaces serve as model systems, as they have only few defects and thus also limit the number of possible side reactions. This is contrary to reactions carried out in solution and at solid-liquid interfaces. In solution, counter ligands can stabilise the oxidation state of a metal atom or in protic solvents the protons can impact the reaction path, e.g. metal exchange reactions can proceed via transient protonation of the macrocycle [16].

## 4.1 Central metal exchange and metalation induced chemistry in surface adsorbed macrocycles

In 2004 Lingenfelder et al. [17] started investigating metal-organic coordination networks in vacuum where the metal is the link between two or more organic molecules. They showed that a metal-organic network made of terephthalic acid and Fe on Cu(100) can be obtained. Several researchers [18–20] have shown that these and similar metal-organic networks can be made in-situ in vacuum giving well-ordered domains. In addition, there was longstanding interest in macrocyclic molecules at surfaces [21,22]. Porphyrin and its derivatives came into the focus of attention as these molecules have a cavity in the middle that can be filled with transition-metal atoms. Many studies in UHV were conducted up to now using porphyrins [23–28] and phthalocyanines [21,25,28–31] which are also macrocyclic molecules with a cavity in the middle. The focus of this thesis is on a lesser known macrocyclic molecule the so-called pyrphyrin.

This molecule was first used by Ogawa et al. in 1984 [32] in order to show that upon metalation with Li it changes its colour. In 2015 Gurdal et al. [33] used Ogawa's molecule, named it "pyrphyrin" and proposed it as a model catalyst for water splitting devices. Pyrphyrin is a macrocyclic molecule containing four nitrogens in the inner macrocycle (Figure 4.1a). It resembles porphine (Figure 4.1b) which is the simplest representative of the porphyrin family. Porphyrins are made up of four pyrrol units that are linked by methine groups forming a macrocycle. Pyrphyrin on the other hand is made up of four pyridines of which two are linked directly and the other two are linked over a spacer carbon atom at which two cyano groups are attached. Both molecules, pyrphyrin [33–36] and porphyrins [24,26,37–45] are known to be able to incorporate metal atoms into the cavity. The diameter of the cavity of porphine is 4.1Å [46] whereas the cavity size of pyrphyrin is smaller by ~0.2 Å.

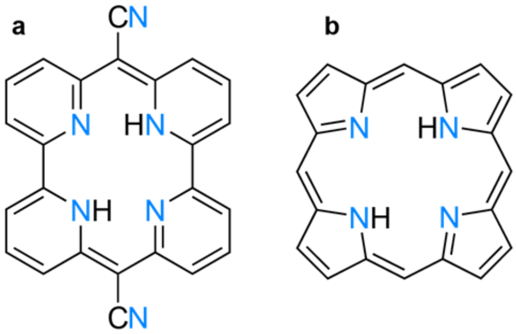

**Figure 4.1:** Tetraaza macrocycles: pyrphyrin, in short 2HPyr (a), and porphine, in short 2HPor (b).

In chapter 6 we show that the metalation reaction of pyrphyrin can be used to dissociate HCN off the molecule in a controlled fashion. Specifically, annealing of the molecule on an Ag(111) surface leads to the scission of both cyano groups whereas metalation of pyrphyrin with Fe ions prior to annealing does not lead to the scission of the cyano groups. This is because the iminic hydrogen (=NH) is available after tautomerisation for 'decyanisation', so that the cyano groups are released as HCN. If the molecule is coordinated with a metal ion, such as Fe at lower temperature, the hydrogen becomes released and is not available anymore for the decyanisation reaction.

In chapter 7 pyrphyrin is used again to show that some weakly bound transition-metal centres can be exchanged with other, more strongly binding, transition metals. This reaction is of course well known in solution. However, no convincing demonstration of atom exchange in surface-adsorbed macrocycles exists [31,47]. Specifically, we show that Cu in copper pyrphyrin (CuPyr) can be exchanged with Ni and Ni in nickel pyrphyrin (NiPyr) can be exchanged with Fe giving iron pyrphyrin (FePyr). The reverse reactions do not occur, which is consistent with the significantly stronger coordination of Fe and Ni compared to Cu.

## 4.2 Interaction between metal surface and organic molecule

Tartaric acid (TA) is a small organic molecule consisting of a 4-C chain with two carboxylic acid functionalities at the ends of the chain and two hydroxyl functionalities bound to the two carbons in the middle of the chain (Figure 8.1). This leads to three stereoisomers of TA: chiral (*R*,*R*)-TA and (*S*,*S*)-TA enantiomers, achiral (*R*,*S*)-TA diastereomer and the racemic mixture of the chiral enantiomers (*rac*-TA). These molecules are used as model systems in UHV for studying the adsorption and desorption of chiral molecules on metal surfaces and their assembly. Over a decade ago the group of Raval investigated the adsorption properties of chiral TA on Cu(110) and found that TA can adsorb in two different ways on the Cu(110) surface: as monotartrate, where one carboxylic acid is deprotonated and interacts with the Cu surface or as bitartrate, where both carboxylic acids are deprotonated and interact with the Cu surface [48–51]. Theoretical calculation gave an idea how TA is adsorbed on the Cu surface [52,53]. Further investigations on the adsorption and chiral crystallisation were conducted with TA on Ni [54–56] and on Cu(110) where the main focus was on the chiral assembly of a layer of TA diastereomers [57–60]. Moreover, an X-ray photoelectron spectroscopy (XPS) study was conducted of chiral TA on a Cu surface [61].

These molecules are oxygen-rich and can decompose autocatalytically into $CO_2$ and $H_2O$. This has been called "surface explosion" [62,63]. It has been shown that vacancies on the surface catalyse the decomposition, leaving behind more vacancies, which then further catalyse the decomposition of more molecules. The term "surface explosion" showed up first in 1973 for a decomposition reaction of formic acid on Ni(110) [64–66]. The kinetics of the surface explosion of TA on Cu(110) and on chiral copper surfaces was investigated in details by Mhatre et al. [62]. During the surface explosion process, in the densely packed monolayer, the thermal stability of the molecules is enhanced compared to a (sub)-monolayer coverage of the TA molecules due to steric constraint. Therefore, the decomposition reaction does not start at the usual decomposition temperature. When the temperature is considerably above the usual decomposition temperature the decomposition reaction starts. In initial steps of the surface explosion free active surface sites are created. On these active sites the decomposition of the TA is catalysed which creates more free active surface sites that in turn can react further. Thus the decomposition reaction proceeds auto-catalytically in a well-defined and narrow temperature window. Typically, the decomposition products of this reaction are $CO_2$, $H_2$, CO and $H_2O$ which desorb swiftly from the surface and which can be easily monitored with a mass spectrometer.

Romer et al. and Bezhadi et al. investigated the surface explosion mechanism of TA on Cu(110) finding that a racemic mixture of TA has it surface explosion at a lower temperature than the chiral TA [57,58,60]. Another geometry of the Cu surface such as Cu(111) was only recently investigated. These studies mainly focus on the packing of a chiral TA layer on Cu(111) [67,68]. In Chapter 8 we show that the TA diastereomers adsorb the same way on Cu(111) as they do on Cu(110) and that the desorption of the diastereomers happens at the same temperature on Cu(111) which is in contrast to the results found on Cu(110).

The investigation of the binding of TA to the Cu(111) surface allows to learn how the metal surface geometry influences the chemistry of the adsorbate. But also the metal surface is changed by the adsorption of a chiral molecule. For this the effect on the surface geometry through the adsorption with (*R*,*R*)-TA is investigated using X-ray photoelectron diffraction (XPD). The XPD method exists since the mid-1970s [69–71]. In this method the photoelectrons are elastically scattered by the surface layers and the angular dependence of the photoelectrons using an energy dispersive analyser in a narrow range of binding energy is recorded. Therefore XPD has two major advantages: one gains structural information about a surface atom species of interest and at the same time one also gains chemical information on the non-equivalent states because the intensity of the scattered photoelectrons depends on the energy of the core level atoms.

XPD is often used to find nanostructures of materials on a metal surface: Muntwiler et al. used XPD to find the distances between surface adsorbed atoms in h-BN/Ni system [72], Fasel et al. used XPD in order to determine if $C_{60}$ molecules bind with a 5-C ring or a 6-C ring to the surface [73] and Kim et al. used XPD to find how FeO films grow on Pt(111) [74]. And Fasel et al. studied the adsorption of the chiral TA enantiomers of the bitartrate adsorbate on Cu(110) through the C1s XPD

[75]. Using single-scattering cluster (SSC) calculations they determined the absolute handedness of the adsorbed chiral molecules together with the molecular distortion due to adsorption.

In chapter 9 we present a XPD study on how the geometry of the top Cu(110) layer is affected by the adsorption of chiral TA. However, no chiral Cu signal is observed within the signal to noise ratio and the limitations of background subtraction. This implies that the induced chirality in the Cu(110) surface layer is too small to be detected with this approach. And further experiments need to be undertaken in order to see this chiral Cu signal with XPD.

# 5 Experimental

## 5.1 Sample preparation in UHV

All experiments were conducted in ultra-high vacuum conditions where the base pressure was below $5 \cdot 10^{-10}$ mbar. The single crystals that were used throughout this study (Ag(111), Cu(111), Cu(110)) were purchased from MaTeck. The polished crystal surfaces were cleaned by several cycles of $Ar^+$ sputtering and annealing. In the case of Ag(111) the annealing temperature was 773 K and in the case of Cu(111) and Cu(110) the annealing temperature was 723 K. All molecules were sublimed from evaporator cells. The post-deposition annealing duration was 10 min if not stated otherwise. Pyrphyrin (2HPyr) was re-sublimated for purification in vacuum and deposited at 626 K evaporator temperature. The tartaric acid diastereomers were used without further purification. The evaporation temperatures were: 397 K for the meso TA ((*R*,*S*)-TA, 98%, Fluka), 388 K for the chiral TA ((*R*,*R*)-TA, 99.5% Aldrich) and 403 K for the racemic mixture (*rac*-TA, 99%, Fluka).

## 5.2 X-ray Photoelectron Spectroscopy

In an X-ray photoelectron spectroscopy (XPS) experiment, or electron spectroscopy for chemical analysis (ESCA), the core levels of the analysed atoms are excited with X-rays. X-ray absorption can lead to the ejection of a photoelectron from the deep core levels where the kinetic energy of this photoelectron depends on the atom from which the photoelectron is ejected and on the chemical environment of that atom. From the kinetic energy the binding energy is calculated. Through chemical shifts information about the composition and the chemical species can be gained. The high surface sensitivity of XPS (~10 nm) due to the very short mean free path of the photoelectrons makes XPS a powerful method for surface analysis [76,77].

XP spectra were recorded using a Specs PHOIBOS 100 electron analyser and by excitation with non-monochromatic Al $K_\alpha$ X-rays in normal emission. In the case where the measurements were conducted on Ag(111), the binding energy scale was calibrated to the $Ag2d_{5/2}$ signal at 368.3 eV. When using the Cu(111) crystal, the binding energy scale was calibrated to the $Cu2p_{3/2}$ signal at 932.7 eV. For analysis, the background obtained on a clean crystal, was subtracted from the binding energy areas of interest. In order to determine the peak areas a polynomial background plus Shirley step was fitted. For further analysis the so obtained XP spectra were deconvoluted into symmetric Voigt functions.

## 5.3 X-ray Photoelectron Diffraction

The X-ray photoelectron diffraction mechanism is explained in Figure 5.1. When irradiated with X-ray photons, the ejected core-level photoelectron of the emitter atom propagates as a spherical particle wave (2). This propagating wave can be scattered by a neighbouring atom resulting in a secondary spherical wave (3). These two waves can constructively and destructively interfere with each other (4). The to be investigated surfaces can be of different types: either perfect single crystals where the atoms are long-range ordered or clusters that are of the same type and orientation though they do not need to be periodically arranged or even adsorbed molecular layers where the molecules are situated at the same positions relative to the atoms of the first substrate layer (5). The interference pattern (6) is mapped with an electron analyser. From this interference pattern the geometric structure around the emitter can be found by comparing the experimental data with simulations [78,79].

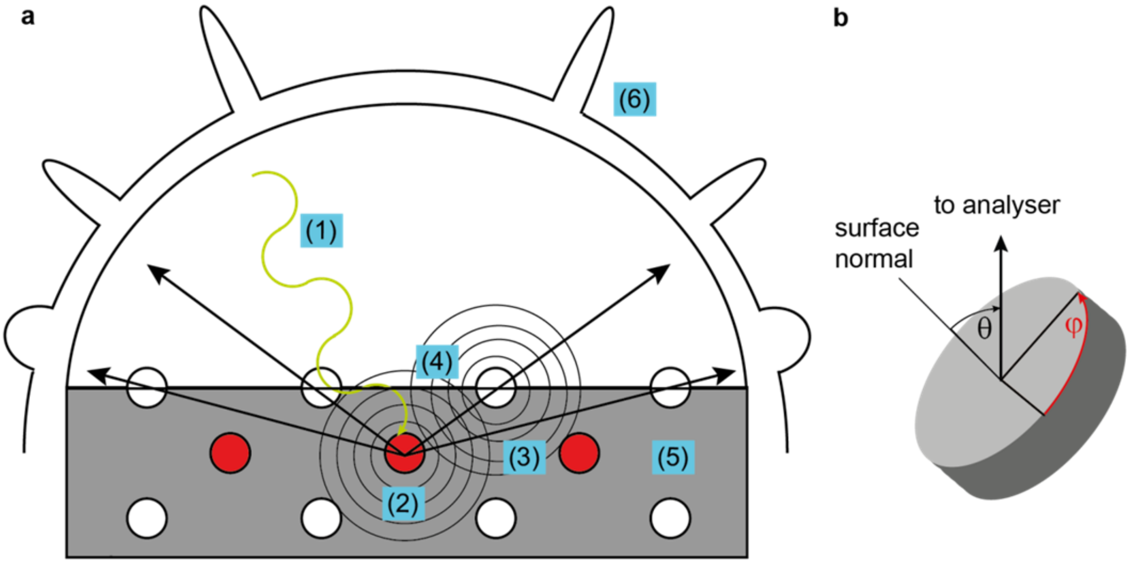

**Figure 5.1:** a) Description of the X-ray photoelectron diffraction method: the incoming X-ray photon (1) ejects a photoelectron from the emitting atom which propagates as a spherical wave (2). This spherical wave ejects a secondary photoelectron which propagates as well as a spherical wave (3). These two waves interfere with each other (4) giving the interference pattern (6). Enhanced intensity is recorded if the surface atoms are orientated in the same direction with respect to the analyser (5) [79,80]. b) θ denotes the polar angle from the surface normal and φ (azimuthal angle) denotes the rotation of the crystal around its axis.

The intensity that is measured in an XPD experiment is proportional to the squared sum / difference of the source particle wave amplitude ($\varphi_0$) and the amplitude of the electron wave scattered of the neighbouring atom ($\varphi_{sc}$).

$$I \propto |\varphi_0 \pm \varphi_{sc}|^2$$

This intensity is strongly angle dependent: it is peaked into the forward direction which coincides with the 0th order diffraction peak and which is also the most prominent peak seen at higher kinetic energies of the photoelectrons. Higher order diffraction peaks, together with the scattering in the other directions becomes more dominant at lower photoelectron energies. In a typical XPD experiment, the intensity is mapped stereographically by the variation of polar (θ) and azimuthal (φ) emission angles of the photoelectrons with respect to the surface normal.

In order to record this angle resolved emission pattern, the crystal is rotated around the polar angle θ (0° to 83°) with an increment of 2° and around the azimuthal angle φ (0° to 360°) with an increment of 1°. More than 83° θ were not achievable in the present experimental setup. At every position the intensity at the binding energy of choice is measured. In particular, the binding energy of 932.8 eV was used corresponding to the binding energy of the $Cu2p_{3/2}$ peak. In the spectrometer used (Omicron EA 125 HR electron analyser) the binding energy of $Cu2p_{3/2}$ was calibrated to 932.8 eV.

XPD is a powerful and diverse method for surface analysis. It is surface sensitive, it gives structural information about the local atomic environment around the emitting atom and it delivers information of the chemical states of the emitting atom. This means, that XPD is one of the few techniques that gives structural and chemical information at the same time. And it is possible to investigate different kinds of surfaces and surface adsorbates. This makes XPD a good method to investigate how a single layer of a chiral molecule such as tartaric acid (TA) imprints its chirality on the non-chiral metal surface.

The main disadvantage of an XPD experiment is its duration. In these experiments a dwell time of 4 seconds is chosen which leads to a total experimental duration of 8 - 9 hours. Irradiation with X-rays for such a long time might lead to damage of the organic layer by the X-ray beam.

## 5.4 Scanning-Tunneling Microscopy

In a scanning tunnelling microscope, an atomically sharp tip scans laterally over the surface. Essentially, the surface electron density in the range between the Fermi level and the set bias voltage is measured and the surface electronic states are imaged. On surfaces that have relatively uniform electronic properties, like a metal surface, the STM contrast corresponds mainly to the topography of the sample. If the scanned surface is electronically inhomogeneous, e.g. transition metals on an organic layer at high resolution, the interpretation of the STM image in the view of topography and electronic states gets more complicated [76,77].

STM images were acquired with a Specs Aarhus 150 instrument in constant current mode with a mechanically cut and in-situ sputtered PrIr (90% Pt) tip. The sample temperature was 295 K unless specified otherwise. The exact imaging conditions can be found in the appendix. For further data analysis the STM images were processed using the WSxM software [81].

## 5.5 Thermal Desorption Spectroscopy

Thermal desorption spectroscopy (TDS) is a method to analyse desorption processes of molecules from a surface. The crystal surface containing adsorbed molecules is placed in front of a mass spectrometer, typically with the surface normal pointing towards it. Then the crystal is warmed up at a constant heating rate. During the heating the mass spectrometer is set to scan the masses of molecular fragments or molecules leaving the metal surface. This simple method allows to identify the desorbing material and gives insight into the activation energy for desorption and the kinetic order of this reaction. For the molecules studied here, TDS is destructive which means that all the molecules will either be destroyed and only fragments will stay on the metal surface or all the fragments leave the surface. In many cases, the molecule-metal bond was stronger than the intramolecular bonds, which means that the molecule decays into fragments which are detected [62,76,77].

During the metalation and metal centre exchange experiments TD spectra were recorded using a quadrupole mass spectrometer from Balzers (QME 200) and for the tartaric acid experiments a Hiden Analytical mass spectrometer HAL 511/3F was used.

## 5.6 Reflection absorption infrared spectroscopy

In reflection absorption infrared spectroscopy experiments (RAIRS), a beam of infrared light is shown onto a reflective sample near grazing incidence angle. Only the component of the beam that is polarised perpendicular to the plane of the surface interacts with the adsorbates on the surface. The component polarised parallel to the surface cancelled out through the 180° phase shift in the reflection process. Therefore, only the molecular vibrations that create a change of dipole moments perpendicular to the surface can be detected by the RAIRS [76].

RAIR spectra were obtained with a Bruker Vertex 70 FT-IR spectrometer at 7° grazing incidence (*i.e.* 93° with respect to the surface normal). Spectra obtained on a clean crystal sample were used for background correction by division through the background spectra. A polynomial background was subtracted in order to flatten the spectra.

# 6 Controlled Decyanisation Reaction of Pyrphyrin on Ag(111)

Results reported in this chapter have been also published in "Identification of On-Surface Reaction Mechanism by Targeted Metalation", by A. Rieger, S. Schnidrig, B. Probst, K.-H. Ernst and C. Wäckerlin, *J. Phys. Chem. C* **2017**, *121*, 27521-27527 [82].

Porphyrins are a common species of molecules for studying surface reactions in UHV because they are easily available and have a wide range of application in biology, chemistry and physics. The molecules are flat and therefore easy to study with STM on metal surfaces. The porphyrin macrocycle can coordinate a transition-metal atom in the cavity of the organic molecule. Metalloporphyrins have a wide range of application depending on the derivatisation of the organic macrocycle and the incorporated transition-metal ion. Other macrocyclic compounds, such as phthalocyanine species, can incorporate a transition-metal ion into their cavity [25,26,29,30]. Depending on the coordinated metal atom and on eventually present axial ligands, metalloporphyrins possess different physical properties and chemical reactivity. At the solvent free vacuum metal interface, Gottfried et al. metalated a tetraphenylporphyrin monolayer adsorbed on a Ag(111) surface with Co atoms [23] in 2006. In 2007 Auwärter et al. [39] metalated the same porphyrin with Fe. Subsequently, other researchers showed that different porphyrin species and other macrocycles can coordinate a variety of transition-metals [24,25,28,39,83]. Also "self-metalation", in which the porphyrin coordinates a metal adatom from the single crystal surface it is adsorbed on, is observed [42]. Wurster et al. used a network of tetrapyridylporphyrin that coordinate a $Co^{2+}$ in the cavity and are linked to each other through the coordination of the pyridinic nitrogen to a $Fe^{2+}$ ion to catalyse the oxygen evolution in the water splitting reaction [84]. Wäckerlin et al. showed that the spin of cobalt-tetraphenylporphyrin can be switched between the magnetic *on* and *off* states by the adsorption of a chemical stimulus [85].

During the metalation process the hydrogens attached to the iminic nitrogen atoms on the inner macrocycle leave the molecule [23,39]. As the activation barrier for the desorption of atomic hydrogen on noble metal surfaces is low, e.g. on an Ag(111) surface it is 23 kJ $mol^{-1}$ [86], hydrogen is generally considered to be irrelevant for further on-surface chemistry. However, there are some observations that show that hydrogen is not as irrelevant to on-surface chemistry as assumed. Specifically, the thermally activated exchange of fluorine bound to carbon with hydrogen and the exchange of carbon-bound hydrogen to deuterium were recently observed [87,88]. And the production of hydrogen by cyclodehydrogenation was proposed to be the rate-limiting step for the desorption of bromine [89].

Here we show that the formation of hydrogen during the metalation of pyrphyrin, a macrocyclic molecule similar to porphyrin, leads to a controlled decyanisation reaction where HCN is dissociated from the molecule. Scheme 6.1 gives an overview over the organometallic complexes and the reaction conditions that will be explained later in this chapter.

**Scheme 6.1:** Reactions that 2HPyr upon metalation with i) Ag and ii) with Fe can undergo.

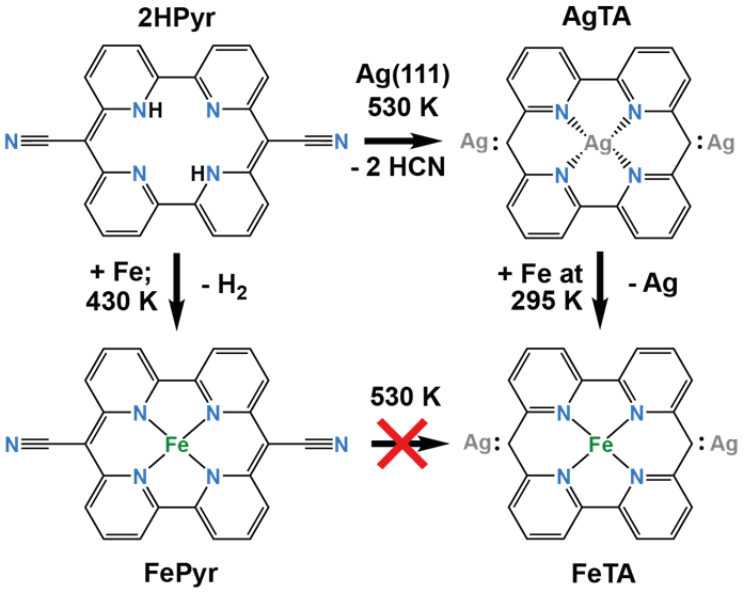

## 6.1 Results and Discussion

### 6.1.1 Annealing without Fe

An STM study on an annealed monolayer of 2HPyr on Ag(111) shows that with increasing temperature more and more molecules appear dark, Figure 6.1a-c. After annealing at 560 K about 80% of the molecules appear dark in STM. Large-scale images of 1 ML of such annealed layers show self-assembled well-defined molecules.

Through these images it can be concluded that the macrocycles remain intact throughout annealing to 560 K. In some images areas of mobile molecules are detected but this is only the case if the coverage of the Ag surface was slightly below 1 ML.

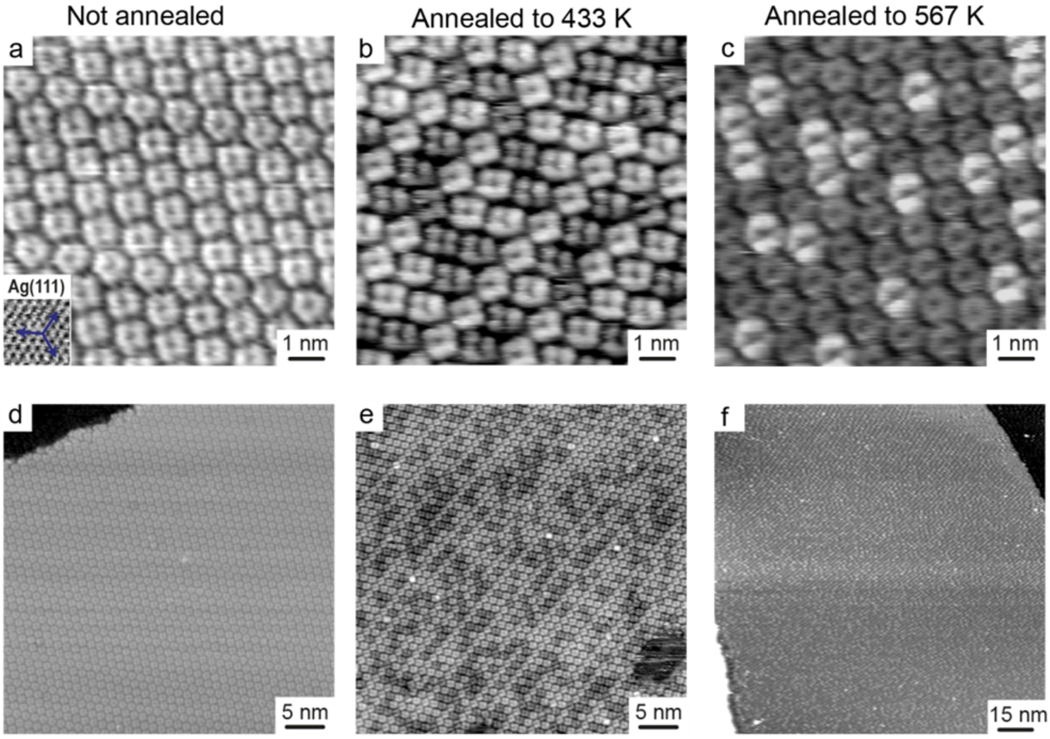

**Figure 6.1.** 1 ML of 2HPyr on Ag(111) images are shown in a-c as small-scale image and as an overview in d-f for increasing annealing temperatures. In a and d the monolayer is not annealed, 100% of the molecules are bright. When the monolayer is annealed to 433 K (b and e), 66% bright and 34% dark molecules are observed. When the monolayer is annealed to 567 K (c and f), 26% bright and 74% dark molecules are observed. The tunnelling conditions are summarised in Table 12.1.

The XP spectrum of the N1s region of 1 ML of 2HPyr deposited on Ag(111) kept at 295 K is shown in Figure 6.2a). It exhibits the characteristic double peak line that is already known for other free-base tetraaza macrocycles (TA) such as porphyrins [40,42], phthalocyanines [25] and pyrphyrin on Cu(111) [35,36,90]. Pyrphyrin has three different nitrogen atoms but due to the small difference in the chemical shifts of the cyano group (-CN, 398.8 eV) and the iminic nitrogen (=N-, 399.4 eV), only two peaks are observed in the raw data [35,36]. The pyridinic nitrogen peak is found at 400.8 eV [35,36]. Table 6.1 gives an overview over the C1s and N1s areas and the C / N ratio seen in Figure 6.2. After annealing to 527 K (Figure 6.2 middle), only one peak at 398.4 eV with reduced intensity is observed. The overall intensity of this peak is reduced by about a third of the spectral weight, which indicates that one nitrogen-containing moiety (most-likely the cyano groups) has desorbed. Because there is only one peak observed implies that the four nitrogens in the inner macrocycle are now equivalent, *i.e.* the pyridinic nitrogen atoms are deprotonated, which corresponds to metalation reactions [23,27]. The only metal with which the organic molecule can be metalated is Ag. The C / N ratio in a monolayer of not annealed 2HPyr molecules is set to be 4 (24 carbons to 6 nitrogens). The C / N ratio of the sample annealed to 527 K is 4.93, which corresponds to 58% AgTA molecules. AgTA is identified as a pyrphyrin molecule that lost its two cyano groups and is therefore present as a formal dicarbene molecule which coordinates to an Ag adatom (Scheme 6.1). This agrees well with the abundance of dark molecules seen in the STM image in Figure 6.1.

A proposed mechanism how such a dicarbene can be obtained is tautomerisation of the molecular structure. By tautomerisation the hydrogen atoms attached to the iminic nitrogen atoms become located next to the cyano groups [91]. By thermal activation the hydrogen and the cyano group detach from the molecule as HCN leaving behind a formal dicarbene (Scheme 6.2). This dicarbene is presumably stabilised by the coordination to an Ag adatom. Later on in this chapter the dissociation of HCN upon annealing is investigated using thermal-desorption spectroscopy (TDS).

**Scheme 6.2:** The proposed tautomerisation pathway that leads to the thermally induced HCN formation is shown here.

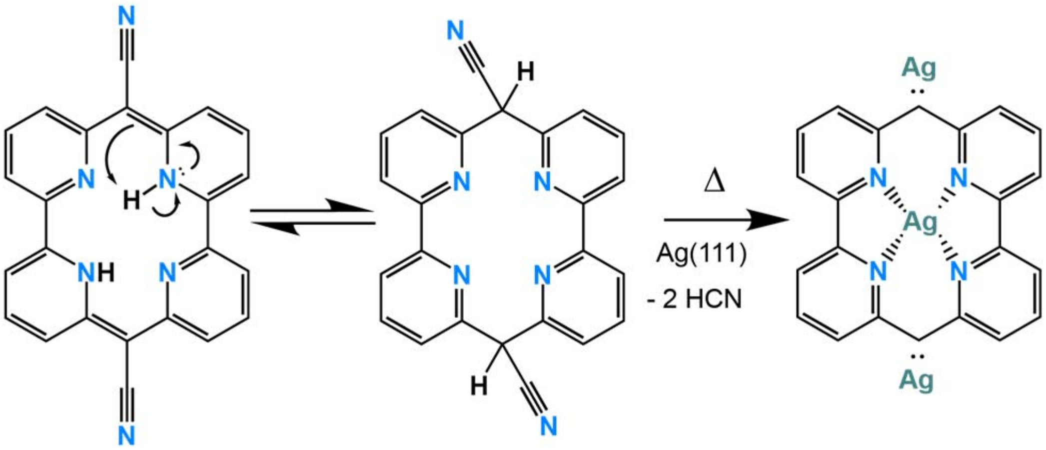

Metalation with Ag has already previously been observed for other tetraaza macrocycles on Ag surfaces [29,30,92,93]. The position of this peak (398.4 eV) agrees with a nitrogen-silver bond in Ag-phthalocyanine that is obtained by self-metalation on Ag(110) [29]. This pyrphyrin species, where the cyanogroups are dissociated and the remaining nitrogen atoms are equivalent, is the AgTA species from Scheme 6.1.

Subsequent sublimation of about 1 Fe per 2HPyr molecule creates an upshift of the N1s peak to 399.25 eV. This higher binding energy agrees well with a N-Fe bond seen in Fe-phthalocyanine on Ag(111) [49] or a N-Co bond in Co-pyrphyrin on Au(111) [36]. The reason for the upshift of the peak position is a stronger N-Fe interaction [56] than the N-Ag interaction. Hence we conclude that a FeTA species has been formed.

.

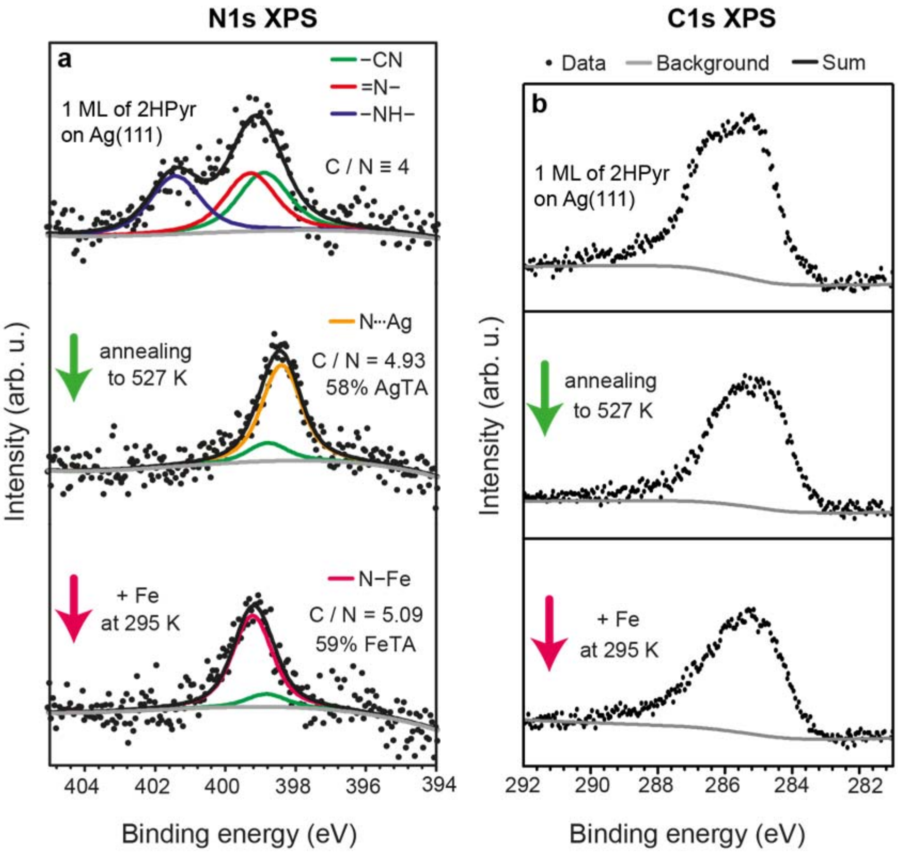

**Figure 6.2.** N1s (a) and C1s (b) XP spectra of 1 ML of 2HPyr on Ag(111). The ML of 2HPyr was annealed to 527 K in the first step (middle). In the second step ~1 Fe per molecule was added (bottom). The XP spectra are off-set for clarity.

**Table 6.1:** N1s and C1s areas with respect to the first XP spectra in Figure 6.2 (1 ML of 2HPyr). The C / N ratio (x) for the 1 ML sample was set to 4. The abundances (A) of AgTA and of FeTA are determined like that: $\boldsymbol{A} = (\boldsymbol{x} - \boldsymbol{c_1})/(\boldsymbol{c_2} - \boldsymbol{c_1})$, where $c_1$ = 4 and $c_2$ = 5.5. These are the C / N ratios for Pyr (deprotonated pyrphyrin) and TA (deprotonated and decyanised pyrphyrin).

| Dataset | N1s area | C1s area | C / N ratio (x) | Abundance of AgTA and FeTA (A) |
|---|---|---|---|---|
| **2HPyr** | ≡ 100% | ≡ 100% | ≡ 4 | ≡ 0% |
| **+ann. 527 K** | 65% | 79% | 4.86 | 58% |
| **+ Fe** | 62% | 76% | 4.79 | 59% |

Figure 6.3 shows the difference spectrum of the C1s XP spectrum annealed to 527 K and the the C1s XP spectrum of 1 ML of 2HPyr taken at 300 K, that is, the

middle spectrum of Figure 6.2b minus the first spectrum of Figure 6.2b. The spectral weight at 286.5 eV, where the carbon of the cyano group should be found, is decreased and the spectral weight at 284.3 eV is increased. Low binding energies are characteristic for metal-organic bonds. For example, the metal organic bond found by methylacetylide with Ag has a C1s signal at 283.7 eV [94]. The lowered binding energy of Ag-methylacetylide compared to AgTA is not surprising due to the increased electron-withdrawing property of the tripple bond in the acetylide.

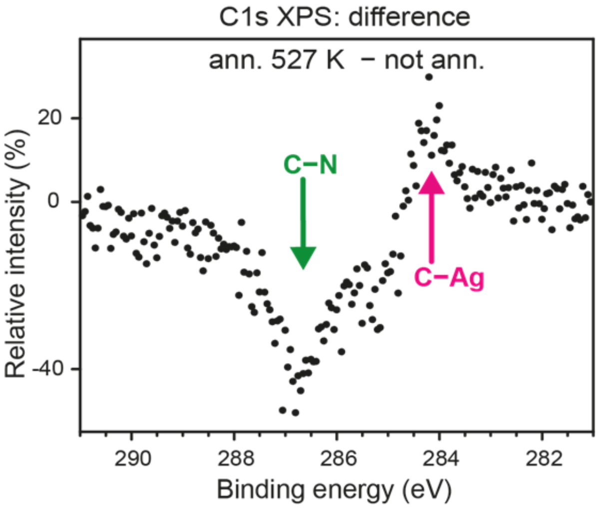

**Figure 6.3:** Difference spectrum of the C1s region, which is the C1s spectrum obtained after annealing to 527 K minus the C1s spectrum obtained from 1 ML of 2HPyr at 300 K.

### 6.1.2 Annealing in the presence of Fe

Figure 6.4 shows the case where Fe is added to a monolayer of 2HPyr while annealing to 433 K. Table 6.2 gives an overview over the areas of the C1s and N1s peaks and the respective C / N ratios. Addition of ~1 Fe atom per 2HPyr molecule and annealing to 433 K gives a different XP spectrum than the ones previously seen in Figure 6.2. The N1s peak intensity is not reduced. The N1s spectrum can be deconvoluted into two components. One is the Fe-N bond found at 399.3 eV in the inner macrocycle and the nitrogen of the cyano group at 397.7 eV. Similar behaviour after addition of Fe to tetraaza macrocycle molecules is observed in the N1s spectra of CoPyr [36] and CuPyr [35]. The C / N ratio remains unchanged compared to the not annealed sample. This indicates that the cyano group is still attached to the molecule. The C / N ratio of 3.89 shows all the organic molecules still contain their cyano groups. This pyrphyrin species which coordinates Fe and did not experience the loss of the cyano groups is called FePyr. This is consistent with the STM data (see below). Annealing this FePyr species to 527 K for 10 min leads to minimal changes in the N1s and C1s spectra. The low binding energy component that was identified as C-Ag bond in the case where the sample was first annealed and then metalated with Fe is not found in the second case. This means that the majority of the metal coordinating pyrphyrin species is present as FePyr not as FeTA. The slight increase from no AgTA molecules to 4% AgTA molecules can be explained with native molecules that are not yet coordinating Fe and lose their cyano groups upon further annealing.

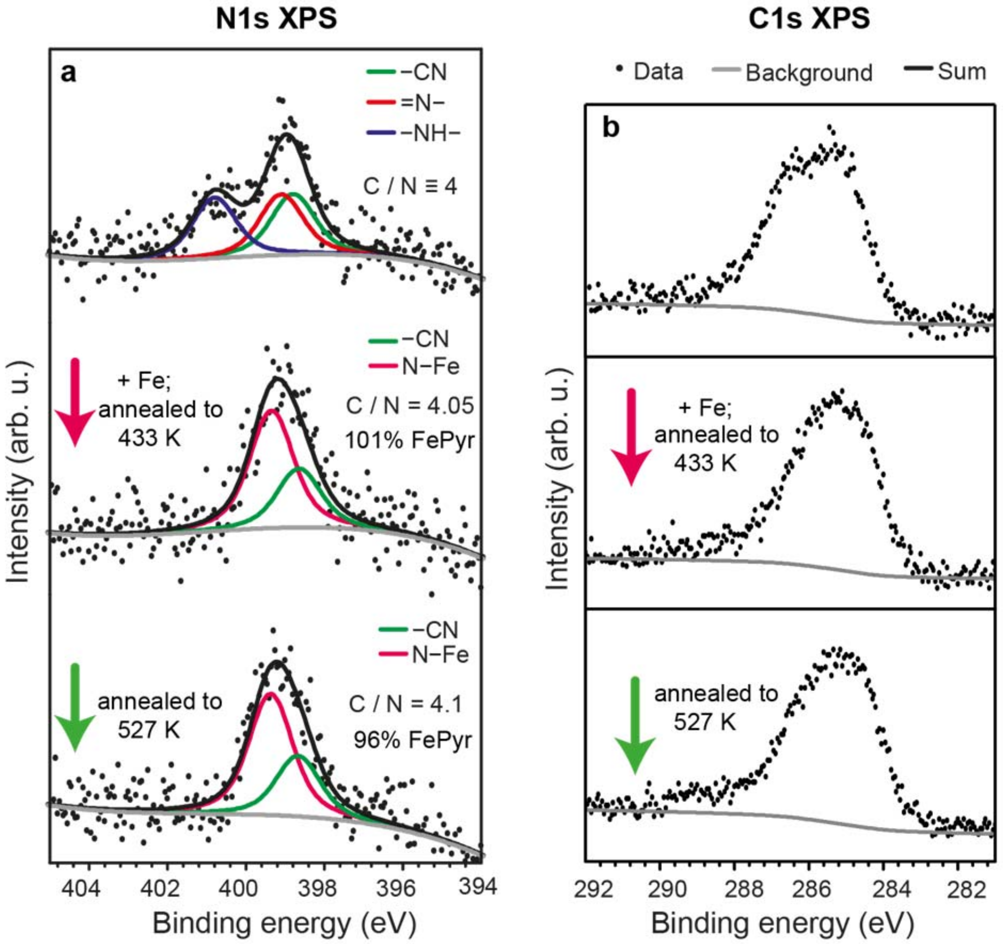

**Figure 6.4:** N1s (a) and C1s (b) XP spectra of 1 ML of 2HPyr on Ag(111). Fe was added to the ML of 2HPyr while annealing at 433 K (middle). In the last step the sample was annealed to 527 K (bottom). The XP spectra are off-set for clarity.

**Table 6.2:** N1s and C1s peak areas with respect to the 1 ML of 2HPyr sample. The C / N ratio (x) for the initial sample is set to 4. From this the abundances (A) of AgTA and of FeTA are determined by $A = (x - c_1)/(c_2 - c_1)$, where $c_1$ = 4 and $c_2$ = 5.5 which are the C / N ratios for Pyr (cyano groups attached to the molecule) and TA (cyano groups dissociated).

| Dataset | N1s area | C1s area | C / N ratio (x) | Abundance of AgTA and FeTA (A) |
|---|---|---|---|---|
| **2HPyr** | ≡ 100% | ≡ 100% | ≡ 4 | ≡ 0% |
| **+ Fe; ann 433 K** | 99% | 98% | 3.98 | -1% |
| **+ ann. 527 K** | 99% | 101% | 4.01 | 4% |

An STM study is conducted on all the different combinations of annealing and Fe addition (Figure 6.5). In Figure 6.5a-c the monolayer of 2HPyr is annealed at 487 K in the case of b and in the case of c it is annealed at 567 K. Fe is not added to these samples. The following samples (d-i) are exposed to an increasing amount of Fe. In samples with high abundance of dark AgTA molecules (e, f, h, i), the addition of Fe leads to the appearance of bright spots in the middle of the molecules. These are the Fe-coordinating molecules (FePyr). In the samples that remain not annealed (d, g) the addition of Fe leads to the formation of Fe-clusters.

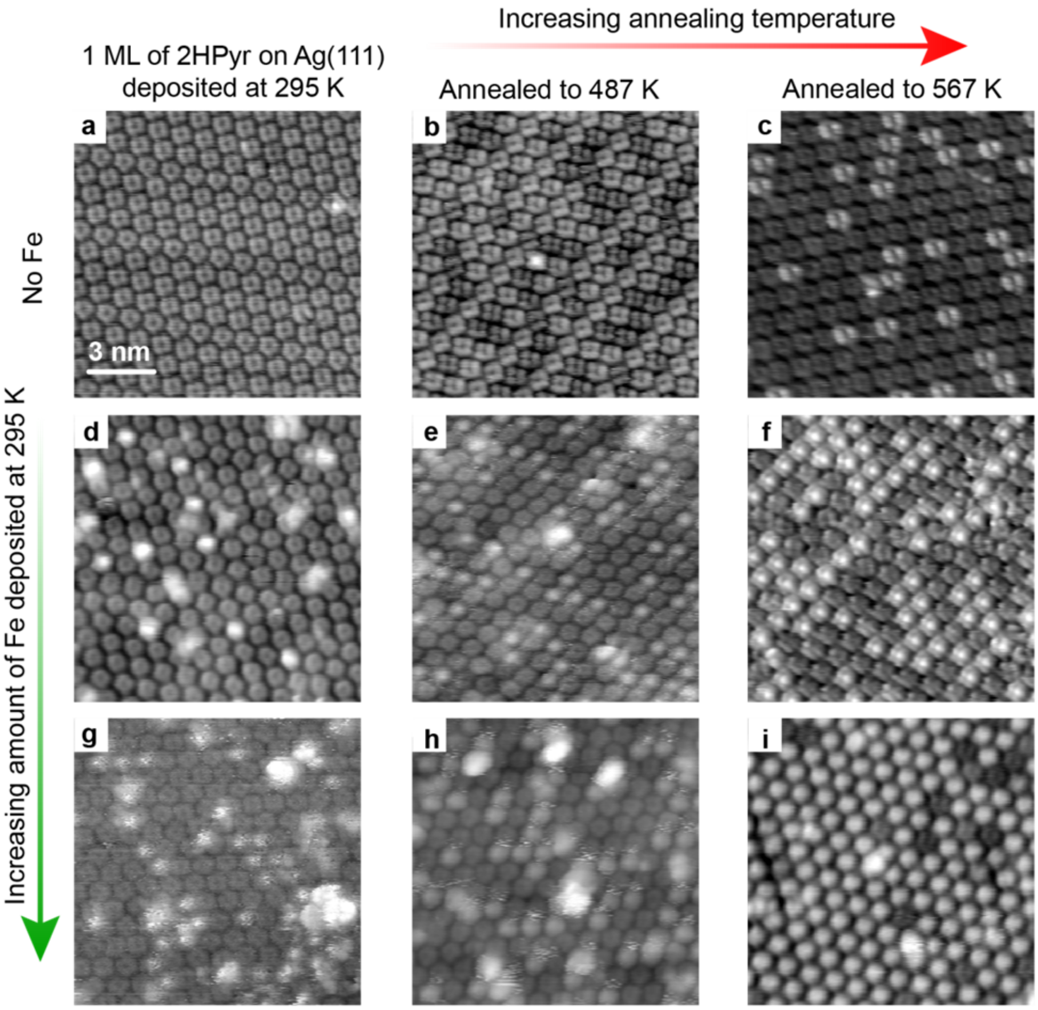

**Figure 6.5:** STM images of 1 ML of 2HPyr on Ag(111) annealed to different temperatures as indicated in the figure and exposed to increasing amount of Fe. a-c) No Fe added to the samples. d-i) An increasing amount of Fe is added to the samples. The scale bar shown in a) applies to all images. The images were obtained at approximately –1.2 V bias. The complete overview over the imaging conditions can be found in the appendix.

If a sample, like the one in Figure 6.5g, where Fe is evaporated onto a monolayer of 2HPyr without annealing, is kept at room temperature for several hours, *i.e.* overnight, then no change is observed, see Figure 6.6. The Fe clusters are imaged as large bright spots. This implies that in order to metalate pyrphyrin with Fe a kinetic barrier needs to be overcome.

There are some molecules that appear brighter than others around them. They are interpreted as Fe coordinating molecules (FePyr or FeTA) or intermediately metalated molecules, as previously described in [34,36]. In intermediately-metalated molecules the metal atom is not yet placed within the macrocycle but is placed on top of a pyridine ring of 2HPyr [36,90]. Such intermediately-metalated molecules appear with an asymmetric protrusion. Usually such molecules are observed in samples of relatively high 2HPyr abundance (Figure 6.6).

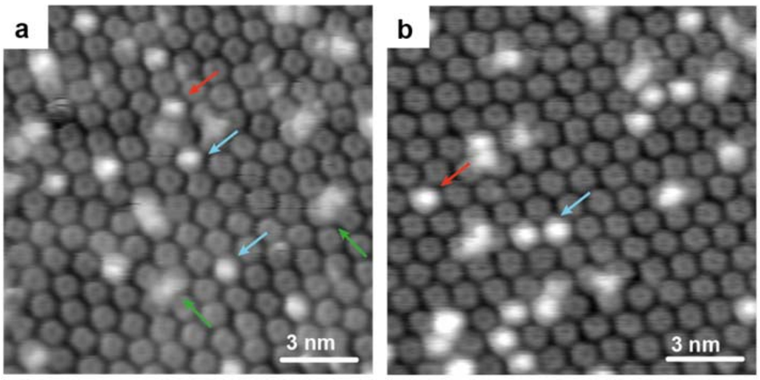

**Figure 6.6:** a) STM image of 1 ML of 2HPyr after the sublimation of ~0.15 Fe atoms per molecule leading to 25% bright (FePyr or FeTA) molecules, without annealing. b) STM image obtained of the same sample after keeping it at RT for 16 h.

Annealing at 433 K for 1 h of a 2HPyr monolayer with Fe clusters on top of the pyrphyrin layer leads to the case where all molecules appear bright, *i.e.* complete metalation of all 2HPyr molecules (Figure 6.7). A very similar observation was made for the metalation of 2HPyr on Au(111) with Co [36].

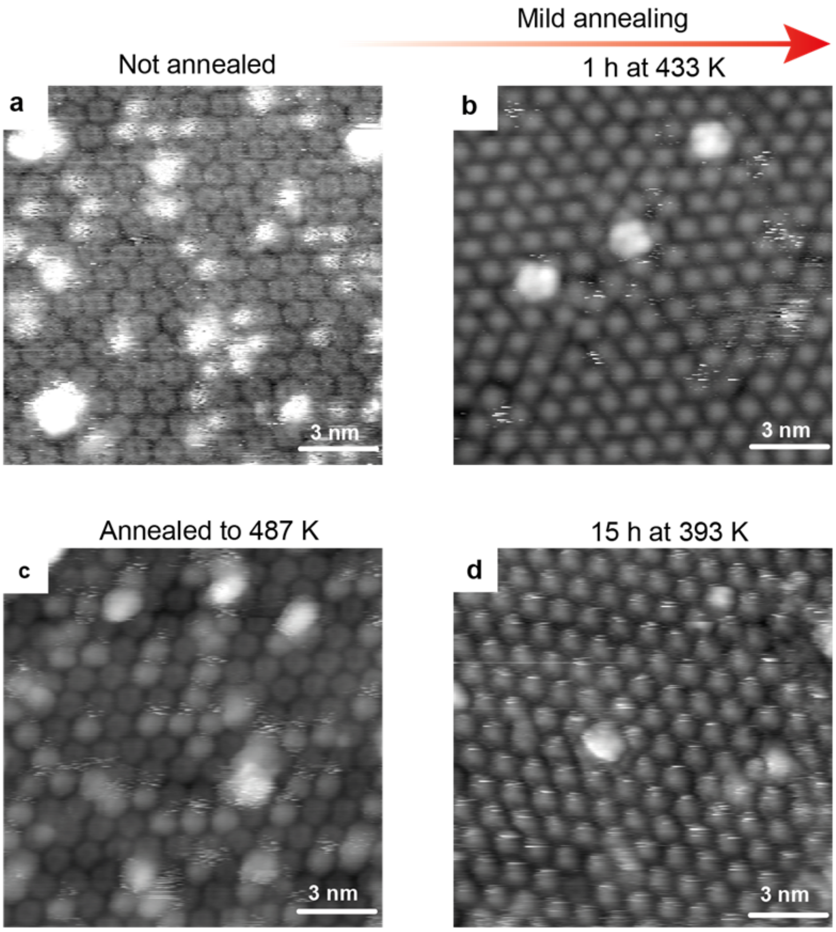

**Figure 6.7:** a) STM image of 1 ML of 2HPyr after the sublimation of 1.26 Fe atoms per molecule on the sample kept at RT. b) STM image of the same image after annealing for 1 h at 433 K. c) STM image of 1 ML of 2HPyr that was previously annealed to 487 K for 10min after the sublimation of ~1.3 Fe atoms per molecule. d) STM image of the same sample after mild annealing for 15 h at 393 K.

The abundances of native 2HPyr, bright species and dark species are presented in Figure 6.8a-c. Figure 6.8a summarises the abundances of the different species in Figure 6.5a, d and g, Figure 6.8b is the summary of Figure 6.5b, e and h and Figure 6.8 is the summary of Figure 6.5c, f and i. Upon the addition of Fe a decrease of native molecules and an increase of bright molecules are observed. In the cases where the samples were annealed and dark molecules are present, the addition of Fe leads to a rapid increase in bright molecules that coordinate Fe. So far a metal ion exchange has been observed for Co and Ni tetraaza macrocycles on Cu(111) surface only at elevated temperatures [47,95]. The fast exchange of Ag with Fe in this study can be explained by Ag being only weakly bound to the macrocycle, as it is most probably sitting below the molecular plane and does not fit into the macrocycle due to its size. Therefore, Ag is easily expelled in favour of the Fe metalation.

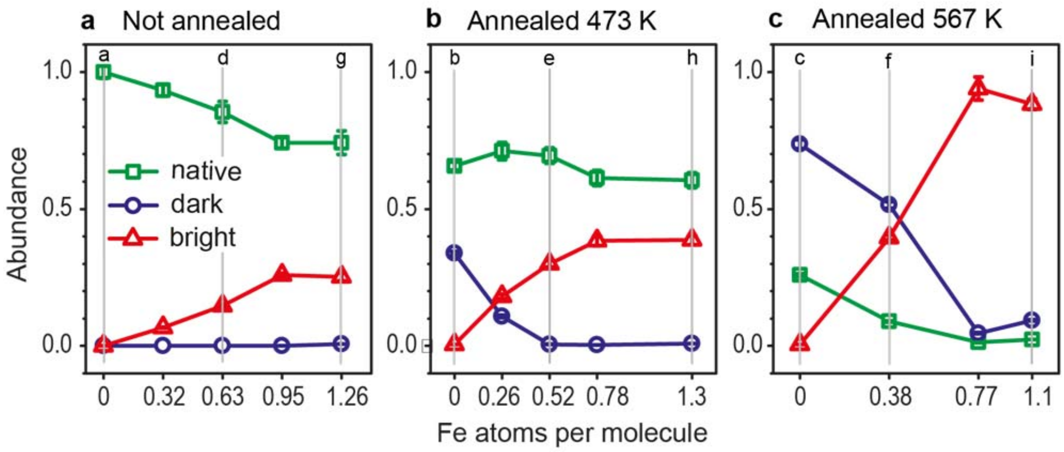

**Figure 6.8:** Relative abundances of native (2HPyr and AgPyr with cyano groups), bright (FePyr (with the cyano groups) or FeTA (without the cyano groups)) and dark (AgTA (no cyano groups)) molecules. a) is the summary of Figure 6.5a, d, g); b) is the summary of Figure 6.5b, e,h) and c) is the summary of Figure 6.5c, f, i).

### 6.1.3 Identification of desorption products by TDS

As discussed above on the basis of XPS and STM data, 2HPyr on Ag(111) loses the two hydrogens at the inner macrocycle and the cyano groups after annealing. However, if 2HPyr is first metalated with Fe giving FePyr, the cyano groups remain attached to the macrocycle and only hydrogen desorbs. Therefore, thermal desorption spectra for $m/z = 2$ ($H_2$) and $m/z = 27$ (HCN) are recorded for samples of 2HPyr on Ag(111) with and without trace amounts of Fe (Figure 6.9).

In the case without addition of Fe, one maximum (β, 620 − 630 K) is observed for the desorption of $H_2$ and two maxima are observed for desorbing HCN. The first HCN maximum is observed at 550 K (α) and the second maximum is again observed at 620-630 K (β). The β maximum, which is observed for the desorption of $H_2$ and of HCN is attributed to the thermal decomposition of the molecules [96,97]. Therefore, the first maximum, α, at 550 K is attributed to the elimination of the cyano groups from the molecule and the desorption as HCN. This is consistent with the XPS data where the formation of AgTA is observed after annealing to 527 K for 10 min.

The HCN curve in Figure 6.9b gives the impression that at 527 K already minor decomposition can happen. However, the large-scale STM images of the annealed monolayers in Figure 6.1d, e and f show extended arrays of molecules with the same appearance as in the not-annealed image. It is therefore concluded that at 527 K most of the macrocycles remain intact.

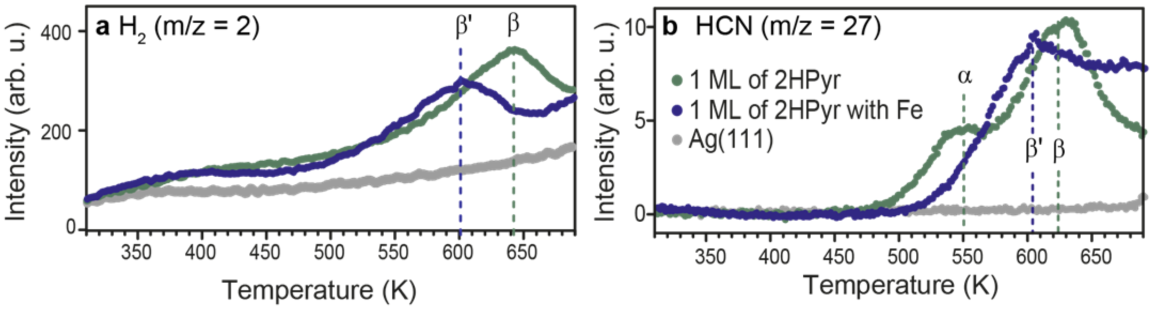

**Figure 6.9:** TD spectra of m/z = 2 (a) and m/z = 27 (b) in case one where 1 ML of 2HPyr is annealed without Fe (green) and in case two where 1 ML of 2HPyr is annealed with Fe (blue). The grey line is the background measured on clean Ag(111).

When 1 ML of 2HPyr is annealed in the presence of Fe only one maximum at 600 K (β') is found. The maximum at 550 K is absent, which is consistent with the findings in the N1s spectrum (Figure 6.4) after annealing the sample to 527 K. The slightly lowered decomposition temperature in presence of Fe (β' *vs.* β) is attributed to the catalytic activity of unreacted Fe or to a lower thermal stability of FePyr. Contrary to TD spectra acquired for the metalation of 2HPyr [35] and 2H-porphyrin [88] with Cu on a Cu(111) surface, no clear peak in the $H_2$ curve for the metalation with Fe is found. This indicates that the rate of metalation of 2HPyr with heteroatoms may be limited by the diffusion of Fe [36] giving a very broad $H_2$ TD curve. Cyanogen, $(CN)_2$, was not observed during these experiments [98]. The reason for the gradual increase in the $H_2$ spectra specifically seen in Figure 6.9a is the warming-up of the sample holder and therefore also an increase in the partial pressure of $H_2$.

## 6.2 Discussion

It is unlikely that only one cyano group detaches from the molecule. The reason is the abundance (A) in the formula $A = (x - c_1)/(c_2 - c_1)$ where $c_1$ and $c_2$ are the C / N ratio for native 2HPyr ($c_1 = 4$) and the pyrphyrin molecule that has lost one cyano group as HCN ($c_2 = 4.6$) or both cyano groups as HCN ($c_2 = 5.5$) and with x is taken from Table 6.1, would be greater than unity (Figure 6.10). The model where two HCN groups leave the molecule corresponds well to the observed data, whereas the model where only one HCN group leaves the molecule does not correspond to the data at all. Therefore, the conclusion is that upon annealing pyrphyrin loses both its cyano groups as HCN.

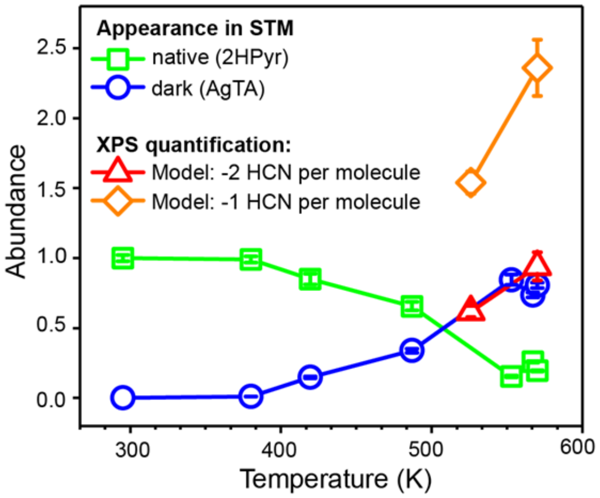

**Figure 6.10:** The two models (loss of one cyano group or loss of both cyano groups) are compared to the abundance of dark (AgTA) molecules and native molecules (2HPyr). In the first model (red triangles) the loss of two cyano groups is assumed. In the second model (orange rhomboids) the loss of only one cyano group is assumed. The calculated abundances of the first model correspond well with the experimental abundances.

Data of the TDS study support the proposed tautomerisation mechanism. Upon annealing of a 2HPyr monolayer HCN dissociates from the molecule. The left-behind organic molecule is a formal dicarbene that is stabilised by the coordination with an Ag adatom. If metalation already happened before the thermal scission of HCN, *e.g.* with Fe giving FePyr, then dehydrogenation of the inner macrocycle already took place so that the Fe atom could be incorporated. The dehydrogenation reaction through metalation with Fe takes place at a lower temperature than dehydrogenation through metalation with Ag, presumably due to the higher reactivity of Fe compared to Ag. Because of the prior dehydrogenation, the hydrogens in the inner macrocycle are not available anymore and therefore tautomerisation and HCN formation are suppressed.

## 6.3 Conclusion and Outlook

An STM study showed an increasing amount of dark molecules with increasing annealing temperature. From XPS we learned that annealing to 530 K leads to dehydrogenation of the pyridinic nitrogen in the inner macrocycle and the loss of the cyano groups. The molecule is stabilised by interaction with an Ag atom from the surface. TD spectra show that the loss of the cyano group happens through desorption of HCN at 550 K. The resulting molecule is a formal dicarbene tetraaza macrocycle denoted as AgTA.

If on the other hand, ~1 Fe atom per molecule is added to a monolayer of 2HPyr, the molecules coordinate Fe by annealing to 433 K giving FePyr molecules. In this case the cyano groups remain attached to the molecule even after annealing to 530 K. Accordingly, no HCN desorption is observed in TD spectra at 550 K.

We explain the observed HCN elimination by tautomerisation. As shown in [91] the two hydrogens from the inner macrocycle get attached to the same carbon where also the cyano groups are attached. In this form the scission of HCN at 530 K is facilitated. If the macrocycle is already metalated before reaching 530 K, *i.e.* FePyr, the hydrogens in the inner macrocycle are already missing, therefore the tautomerised form that makes HCN scission much easier cannot be formed and therefore the FePyr molecule remains stable at 530 K and no HCN desorption is observed.

Decyanation does not occur at lower temperatures when the molecules are metalation with Fe, which indicates that the tautomerised form is not accessible at lower temperature.

The AgPyr and FePyr without the cyano groups are formally dicarbene species. The dicarbene is considered to be stabilised by Ag adatoms or binding to the surface. It would be interesting to see how the formal dicarbene is stabilised. Even though the dicarbene might be stabilised somehow if could still be a reactive species which would offer a possibility for carbene chemistry. Unfortunately, direct polymerisation of two carbene molecules is sterically hindered by C-H repulsion.

Having the oxygen binding and carbon dioxide desorbing properties of the Fe-porphyrin system in haemoglobin in mind, it would be interesting to use the FePyr with or without the cyano groups for oxygen or carbon dioxide binding reactions. This would open the field of metalation in UHV to applications.

# 7 Metal Centre Exchange in Surface-adsorbed macrocycles

Results reported in this chapter have been also published in "Ranking the Stability of Transition Metal Complexes by On-Surface Atom Exchange", by A. Rieger, S. Schnidrig, B. Probst, K.-H. Ernst and C. Wäckerlin, *J. Phys. Chem. Lett.* **2017**, *8*, 6193-6198 [99].

In solution, it is well known that the central metal atoms in porphyrins and porphyrin-like macrocycles can be exchanged with one another according to the reaction $M_1(II)P + M_2(II) \rightarrow M_2(II)P + M_1(II)$ [38,45]. This has been called "transmetalation" in older works. In new literature the terms "ion exchange" or "atom exchange" is more common. In this chapter, in contrast to the previous one, the exchange of the metal centre rather than the chemistry at the ligand is of interest. However note that on Cu(111), where these experiments are conducted, the cyano groups remain attached [35]. This reaction is here called "central metal exchange". At the solid-vacuum interface this exchange reaction involves reduction and oxidation of the involved metals: $M_1(II)P + M_2(0) \rightarrow M_2(II)P + M_1(0)$. This is a redox reaction, in contrast to the reaction mechanism in solution. There counter-ligands are available and therefore the oxidation state of the metals does generally not change. Furthermore, if the ion exchange reaction is conducted in protic solutions, then the reaction proceeds via transient protonation of the macrocycle [16].

The occurrence of the central metal exchange reaction depends on the change in the Gibbs free energy of the two metal porphyrins with respect to the Gibbs free energy of the free metals and also on the height of the reaction barrier. To calculate the energies of the reactants during the exchange reaction is very challenging for macrocycles adsorbed at the solid-vacuum interface because high-level *ab-initio* calculations for the macrocycle-substrate system are required. Previously published density functional theory (DFT) calculations on metal-macrocycle complexes in vacuum can show a trend to whether a given central atom exchange occurs or not. These calculations rank the binding energies for M(II)-porphyrins [100–102], M(II)-phthalocyanines [100] and M(II)-porphyrazines [100] as {Fe, Co, Ni} > Cu > Zn. This order of binding energies is found with respect to the neutral M(0) atom contrary to ref. [101] where the binding energies are referenced against the M(II) ions. The data on the M(II)-

porphyrin coordinate bond strengths calculated from infra-red spectroscopy [37] and on the stability order found in demetalation experiments [45] support the trend in binding energies found with DFT calculations. The reported stability orders for the Fe, Co or Ni coordinating macrocycle differs for different macrocycles and also for the same M(II)-macrocycles that are studies with different DFT methods. This indicates that Fe, Co and Ni macrocycles are rather close in binding energy. But still, the general stability order {Fe, Co, Ni} > Cu > Zn is due to the increasing orbital occupation of the $3d_{x^2-y^2}$ orbital in the series of the square-planar complexes of Ni(II) ($3d^8$), Cu(II) ($3d^9$) and Zn(II) ($3d^{10}$) [100,103]. Such hybrid organo-metallic - metal interfaces are of significant scientific and technological interest. Therefore, it is surprising that the atom exchange reaction at the solid-vacuum interface was not studied up to great depth. Until present, the atom exchange has been only studied by X-ray spectroscopic techniques such as X-ray photoelectron spectroscopy (XPS) and X-ray absorption spectroscopy (XAS) [47]. The exchange of the central metal ion in Ni-bromo-porphyrin species from Ni to Cu giving Cu-bromo-porphyrin species on a Cu(111) substrate was studied by monitoring the changes in the Ni2p XP spectrum and the Ni $L_3$ edge in XAS. Unfortunately, the exact role of the bromine anion on the surface under the used experimental conditions was not explored in great detail [104,105]. As the formation of $NiBr_2$ is preferred over the formation of $CuBr_2$ ($\Delta H_f^0 = -212$ kJ mol$^{-1}$ *vs.* $-141.8$ kJ mol$^{-1}$) [106] this could be the driving force for the exchange of Cu with Ni. Similar effects seen for metalation reactions in the presence of an oxygen layer [107] supporting the idea that the formation of $NiBr_2$ might be the driving force. Furthermore, the authors do not explain why the exchange of Ni as the central metal ion in Ni-bromo-porphyrins with Cu − despite the vast excess of Cu − does not happen for all the porphyrin molecules. Another study reported the exchange reaction of Co to Cu for the CoPc on Cu(111) system [31]. The reaction was claimed to occur at higher temperature. Moreover, the atom exchange was claimed only on the basis of a very small shift in the Co $2p_{3/2}$ core level, which does not make this study very convincing. Both abovementioned studies, the Ni to Cu and the Co to Cu exchanges, were reported to be endothermic [31,47], which is consistent with the previously discussed relative stability order. Also at the metal-solvent interface metal centre exchange reactions were studied, *e.g.* the Zn to Cu exchange [44]. But it has to be considered, that in the presence of protic solvents the metal exchange reaction can proceed via transient protonation [16] which is a different reaction path than the reaction path at the solid-vacuum surface. Therefore, exchange reactions at the solid-solution interface cannot be taken as an analogy to the reactions at the solid-vacuum interface.

In this chapter the central metal atom exchange reaction of Cu, Ni and Fe in the previously described pyrphyrin molecule adsorbed in monolayer coverage at the metal-vacuum interface are investigated using STM and XPS. Scheme 7.1 gives an overview over the metal centre exchange reactions.

**Scheme 7.1:** Metal centre exchange reaction. Pyrphyrin (2HPyr) is metalated with Cu, Ni or Fe. The relative stability is tested by exchanging the existing metal centre, *e.g.* Cu with another metal, *e.g.* Fe. If not mentioned otherwise, the duration of the annealing steps is 10 minutes.

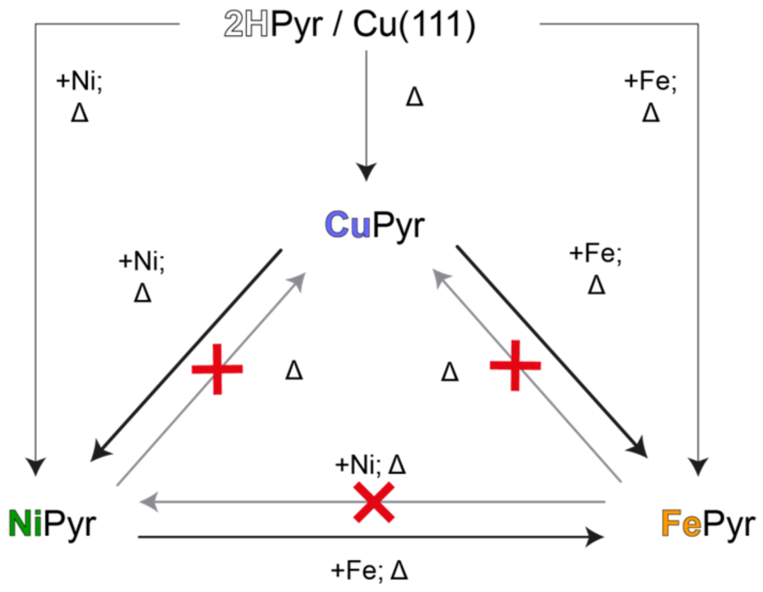

## 7.1 Results and Discussion

All the central metal atom exchange experiments start from 1 ML of 2HPyr on Cu(111). Such a monolayer is obtained by evaporation of 2HPyr onto the Cu(111) crystal kept at 295 K and annealing for 10 minutes to 423 K. This leads to metalation with Cu from the substrate giving CuPyr. Using what we call "normal tunnelling conditions", *i.e.* $U_t$ = [–0.9 to –1.2] V and $I_t \approx -100$ pA, the CuPyr molecule appears dark in the centre because the 3d orbitals of the Cu in this square-planar complex lack out-of-plane states around the Fermi energy [21,22,35,108,109]. As low-spin Ni(II) complexes do not have 3d states around the Fermi energy either they are also seen with a dark centre in STM images [22,108,109]. On the other hand complexes of Mn(II), Fe(II) and Co(II) have out-of-plane 3d states and are therefore imaged with a bright centre in STM [21,22,108,109]. Using what we call "low bias voltage tunnelling conditions" with a suitable and stable STM tip a shallow protrusion in the centre of a CuPyr molecule can be seen. Typical values for these "low bias voltage tunnelling conditions" are $U_t$ = [–50 to –200] mV and $I_t$ = [–0.2 to –1] nA. In NiPyr molecules this protrusion is brighter than the one in CuPyr [35], therefore at these "low bias voltage tunnelling conductions" NiPyr can be distinguished from CuPyr. Normal tunnelling conditions are used to distinguish FePyr from CuPyr or NiPyr and "low bias voltage tunnelling conditions" are used to distinguish NiPyr from CuPyr.

### 7.1.1 Cu to Fe exchange

Adding trace amounts of Fe to a CuPyr layer (dark centre) and subsequent annealing to 423 K (for 10 minutes) gives rise to a bright feature in the middle of the macrocycle of some of the pyrphyrin molecules (Figure 7.1a,b,c). This is characteristic for central metal atoms with out-of-plane 3d states such as Fe(II) [21,22,36,108,109]. Hence, the molecules with the bright centre are identified as FePyr. With increasing amount of Fe addition the number of bright-centred molecules increases as well (Figure 7.1d). Throughout the central metal atom exchange process of CuPyr to FePyr very little cluster formation takes place (Figure 7.1c).

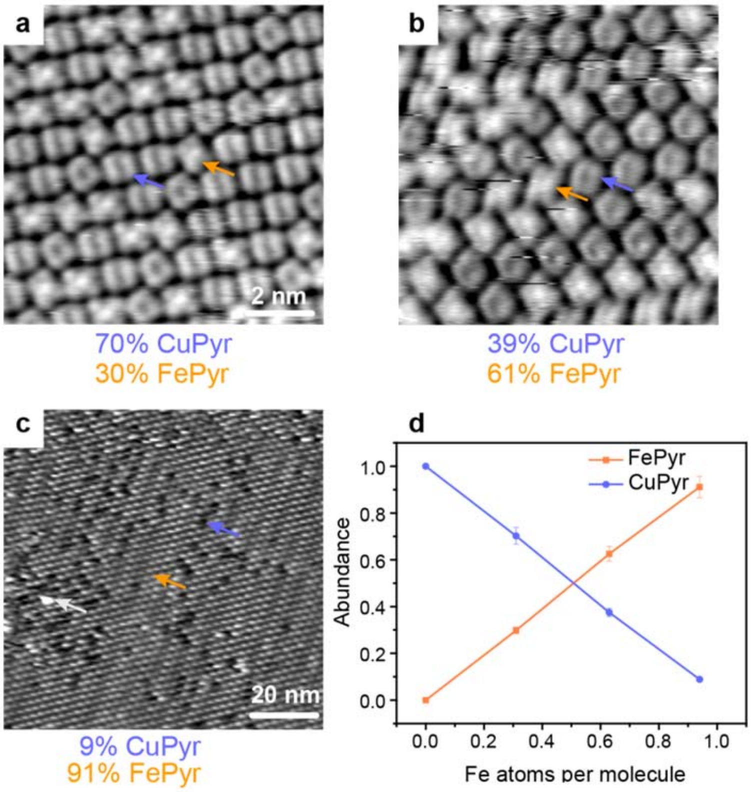

70% CuPyr
30% FePyr

39% CuPyr
61% FePyr

9% CuPyr
91% FePyr

**Figure 7.1:** STM images of the metal exchange reaction of CuPyr to FePyr where Fe is supplied by sublimation. The yellow arrow indicates FePyr molecule. The respective amount of FePyr is written in yellow below the STM images. The blue arrow indicates the CuPyr molecules and again the respective amount of CuPyr is written in blue below the STM images. The STM images a), b) and c) were obtained at increasing amount of supplied Fe and annealing to 423 K. FePyr molecules have a bright centre while CuPyr molecules have a dark centre. The large-scale image in c) shows that more than 90% of the molecules are present as FePyr and there are only very few clusters (the white arrow in (c) indicates one of the few metal clusters). d) shows the abundances of FePyr and CuPyr for increasing amount of Fe atoms. Calibration of the supplied amount of Fe took place by counting the bright centred FePyr molecules. The amount of Fe where only FePyr molecules (no more CuPyr) and no metal clusters could be detected is assigned as 1 eq. (= 1 Fe atom per pyrphyrin molecule).

Figure 7.2 shows the XP spectra of metallic Fe on Cu(111) (bottom) and of Fe(II) in FePyr (top). The binding energy of metallic Fe is 707.0 eV which is almost identical with the binding energy of Fe in FePyr (707.2 eV). That the difference between the binding energy of M(II) atoms in tetrapyrrols to the binding energies of the metals is very small (< 0.3 eV) was already reported before, *e.g.* for (sub)ML coverages of FePc on Ag(111) [25], for CoTPP on Ag(111) [23,83] or for CoPc on Cu(111) [31]. The low binding energy difference is explained to be a consequence of electronic interaction between the metal ions and the substrate [83]. Due to the low binding energy difference XPS is not the method of choice to distinguish FePyr from CuPyr. Due to the bright contrast in the centre of the macrocycle, however, it is easy to distinghish FePyr from CuPyr and NiPyr in STM images.

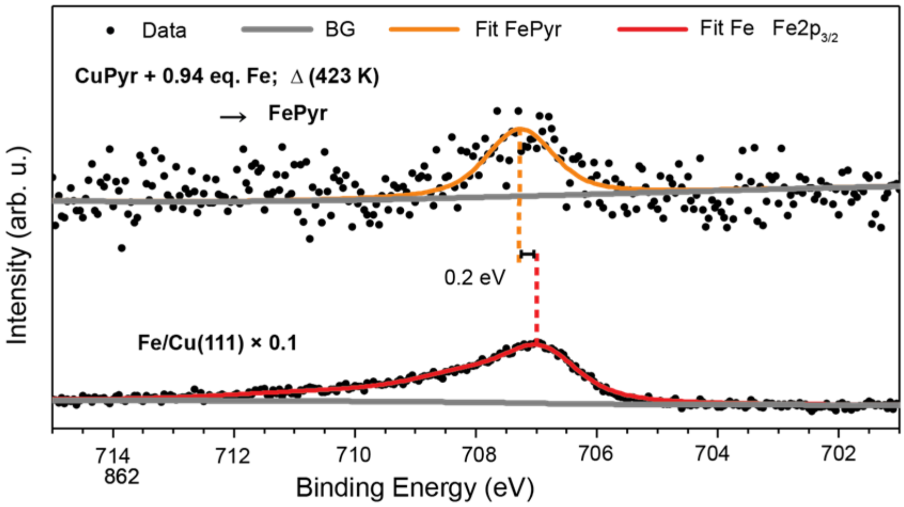

**Figure 7.2:** Metal atom exchange from CuPyr to FePyr as studied by XPS. The spectrum of the metallic Fe$^0$ (bottom) is compared to the spectrum of Fe(II) in FePyr (top). The binding energy of metallic Fe (707.0 eV) is very close in energy to the binding energy of Fe(II) in FePyr (707.2 eV). Due to the small shift XPS is not a good method to distinguish between CuPyr and FePyr. The XP spectra are vertically off-set for clarity.

### 7.1.2 Cu to Ni exchange

In order to investigate the central metal atom exchange from CuPyr to NiPyr the starting material was again 1 ML of CuPyr to which increasing amounts of Ni are added. Figure 7.3 shows the corresponding STM images after annealing at 423 K. As already mentioned, low spin Ni(II) square-planar complexes, like the here shown Ni-Pyr complexes, do not have significant out-of-plane 3d state density, therefore the centre of theses complexes is imaged dark under the here applied tunnelling conditions, just like for CuPyr [21,22]. Thus, "high current and low bias voltage" tunnelling conditions are used (see Table 12.1) in order to distinguish CuPyr from NiPyr complexes. Now CuPyr appears darker in the centre than NiPyr, although this contrast may also depend on the STM tip condition, e.g. radius of the tip and what is adsorbed on the tip. Like in the case of the metal atom exchange of Cu with Fe a linear increase of the NiPyr abundance with increasing amount of supplied Ni is observed.

Hence in analogy to the Cu to Fe exchange, the Cu to Ni exchange reaction for pyrphyrin is very efficient.

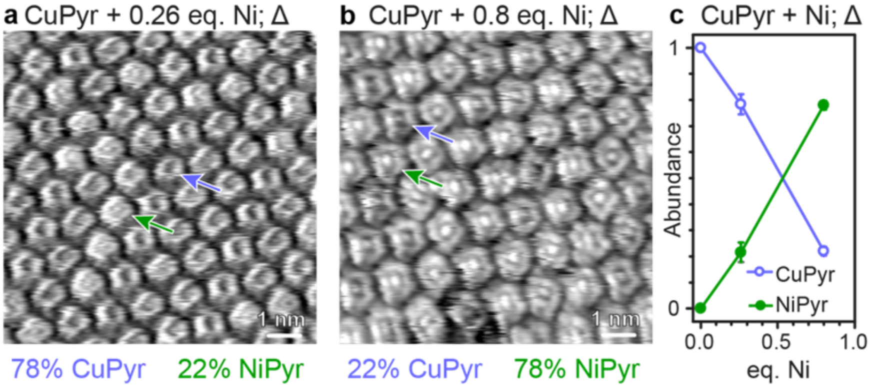

**Figure 7.3:** The STM images of the central metal atom exchange reaction of CuPyr to NiPyr with increasing amount of Ni, deposited by *in vacuo* sublimation. The green arrows indicate NiPyr molecules and the respective amount of NiPyr molecules is written below the STM images in green. The blue arrows indicate CuPyr molecules and again the respective amount of CuPyr is written below the images in blue. The amount of deposited Ni is given above the images a) and b). Images are taken after annealing to 423 K for 10 minutes. The high current and low bias voltage tunnelling conditions (see text) are used to observe a different contrast for the Ni and Cu centres. CuPyr molecules have a darker centre while NiPyr molecules have a brighter centre. c) shows the abundance of NiPyr which increases linearly with the increasing amount of supplied Ni. Calibration of the supplied amount of Ni took place by counting the bright centred NiPyr molecules. The amount of Ni where only NiPyr molecules (no more CuPyr) and no metal clusters could be detected is assigned as 1 eq. (= 1 Ni atom per pyrphyrin molecule).

The central metal atom exchange from CuPyr to NiPyr can also be monitored in the Ni $2p_{3/2}$ XP spectrum (Figure 7.4). Again, the monolayer of CuPyr was annealed to 423 K (for 10 minutes) in the presence of Ni. Metallic $Ni^0$ on Cu(111) has a binding energy of 852.8 eV. Ni(II) in NiPyr experiences a chemical shift and its binding energy is 3 eV higher (855.8 eV) than in the $Ni^0$ case. Similar binding energies and energy shifts were found for formal Ni(II) in NiBrTPP on Cu(111) [110] and in NiTPP on Au(111) [41]. Therefore, the formation of NiPyr in the present case is confirmed. The sift to higher binding energies reflects the situation that the central atom turns normally into a cation, donating electrons to the ligand.

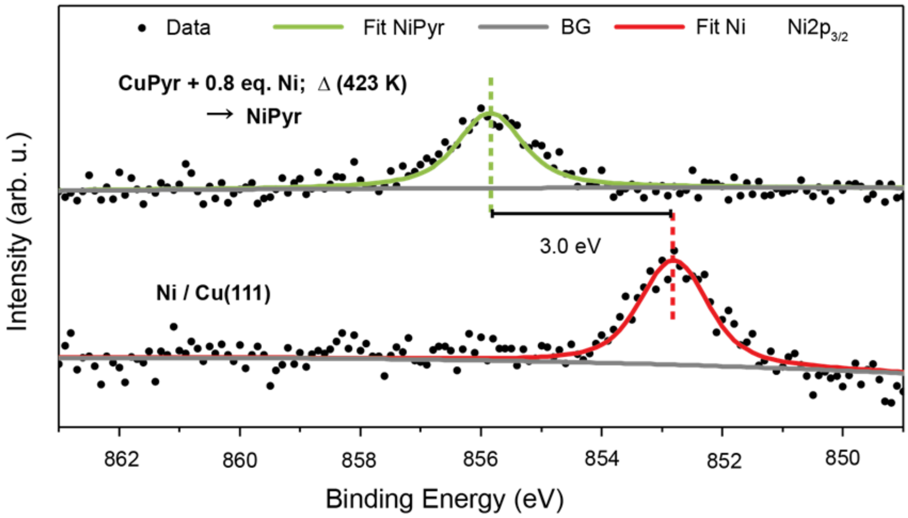

**Figure 7.4:** Central metal atom exchange reaction from CuPyr to NiPyr starting from 1 ML of CuPyr as studied by XPS. The spectra are normalised with respect to the substrate signal and vertically offset for clarity. The bottom spectrum shows the Ni $2p_{3/2}$ region for metallic Ni (852.8 eV). The top spectrum shows the same region for Ni(II) in NiPyr (855.8 eV). The two Ni species are easily distinguishable by their peak positions.

### 7.1.3 Potentially occurring reverse reactions

The possibility of reverse reactions from FePyr back to CuPyr and NiPyr back to CuPyr were evaluated. Figure 7.5 shows the an STM study of prolonged annealing of FePyr on Cu(111). Starting with a 91% fraction of FePyr molecules in the monolayer plus annealing this sample at 473 K for 1 h does not convert the FePyr back to CuPyr. Only the FePyr content increases a bit to 94%.

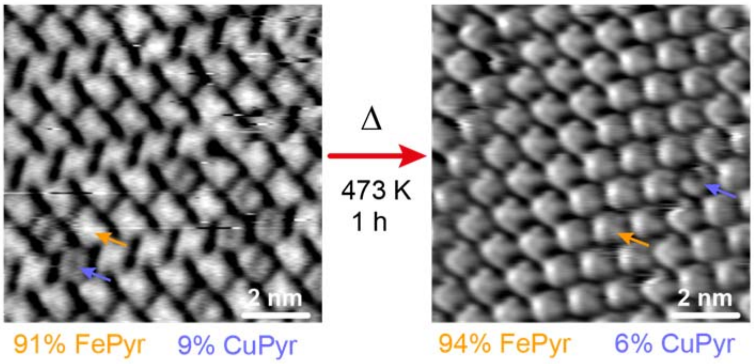

**Figure 7.5:** STM study on the assumed reverse reaction from FePyr to CuPyr. Starting with 91% FePyr (and 9% CuPyr, left image) and annealing the sample at 473 K for 1h does not lead to in increased amount of CuPyr. After annealing 94% of the molecules are present as FePyr (and 6% as

CuPyr). The yellow arrows indicate FePyr molecules with the respective amount of FePyr molecules written in yellow below the STM images. The blue arrows indicate CuPyr molecules and again the respective amount of CuPyr molecules is written below the STM images.

The presumed reverse reaction from NiPyr to CuPyr was also investigated. Figure 7.6 gives an overview over the conducted XPS study. The Ni $2p_{3/2}$ peak of NiPyr is located at 855.8 eV. Annealing 1 ML of NiPyr at 473 K for 1 h does not lead to a shift in binding energy. The peak for metallic Ni is expected to be found at 852.8 eV but it is not found after the annealing. This gives rise to the conclusion that the reverse reaction from NiPyr to CuPyr does not occur under the applied conditions. These two results imply that NiPyr and FePyr are both more stable than CuPyr.

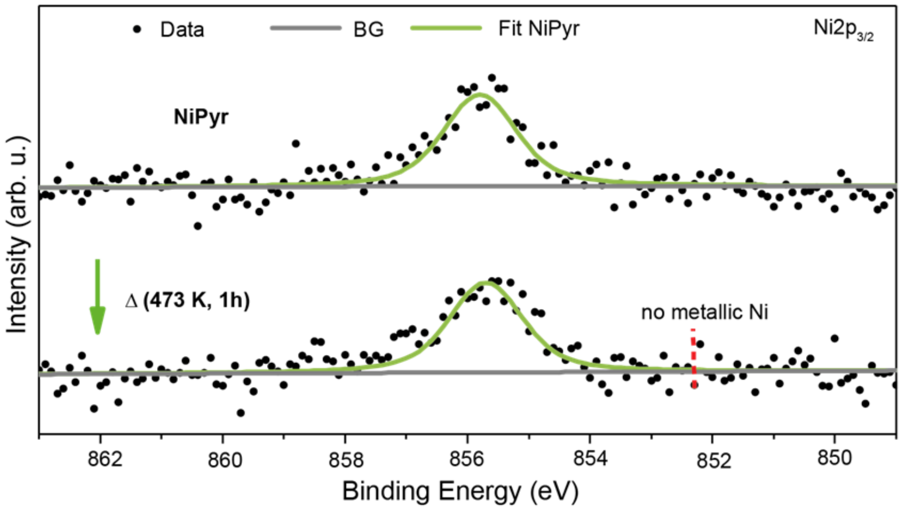

**Figure 7.6:** XPS study on the reverse reaction of NiPyr to CuPyr. The Ni$2p_{3/2}$ peak of NiPyr is found at 855.8 eV (top). After annealing this sample at 473 K for 1 h no metallic Ni (852.8 eV) is found (bottom). This implies that the reverse reaction does not occur. The XP spectra are vertically off-set for clarity.

### 7.1.4 Ni to Fe exchange

What remains is the relative ranking of the stability of NiPyr with respect to FePyr. In order to do this, metal atom exchange experiments (Figure 7.7) were conducted such that Fe is added to NiPyr and Ni is added to FePyr. Starting from a layer containing 84% NiPyr and 16% CuPyr (Figure 7.7a), 0.9 Fe atoms per molecule are added and the sample is annealed to 423 K for 10 minutes. After annealing 50% of the molecules are present as FePyr (Figure 7.7c). Under normal tunneling conditions that are applied here it is not possible to distinguish between CuPyr and NiPyr. Metallic Ni is observed in XPS after addition of Fe to NiPyr and annealing (Figure 7.8). This shows that Ni was expelled from the macrocycle by incorporation of Fe.

The reverse experiment was also conducted. The starting material is 1 ML of FePyr (Figure 7.7b). This is annealed to 423 K for 10 min in the presence of excess Ni. The resulting layer consists of nearly 100% FePyr (Figure 7.7d). From this result it can be concluded that FePyr is more stable than NiPyr. Though the difference in stability between FePyr and NiPyr may be smaller than the difference in stability between CuPyr and either FePyr or NiPyr (Figure 7.7a to c). It is also possible that the activation barriers for the Ni to Fe exchange are higher.

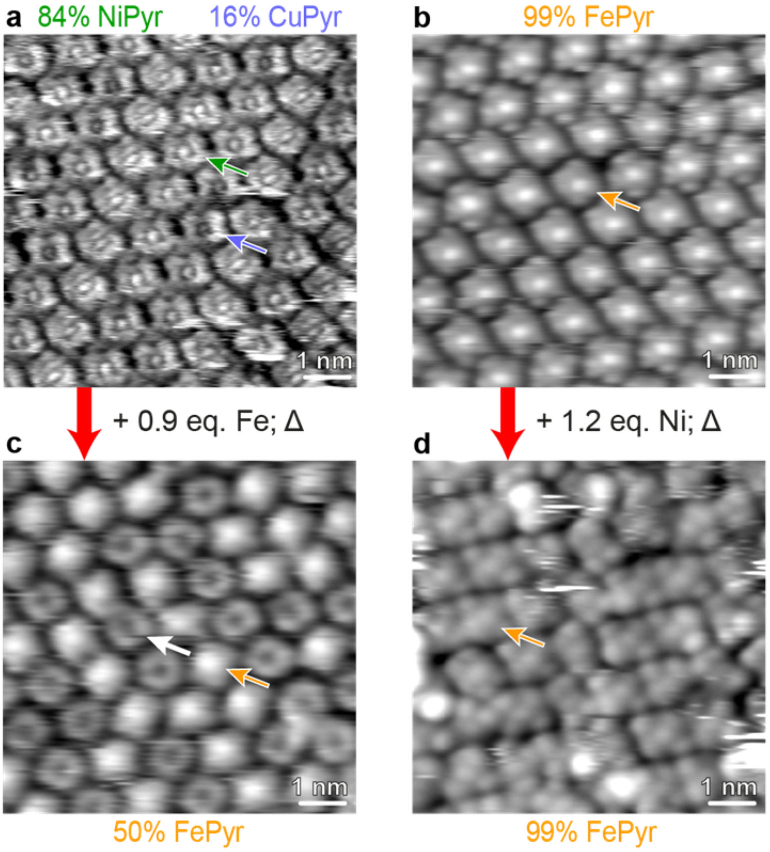

**Figure 7.7:** STM study of the central metal atom exchange experiments starting from a layer mostly consisting of NiPyr (a, 84% NiPyr and 16% CuPyr) and annealing for 10 minutes to 423 K in presence of Fe (c). After annealing 50% of the molecules present are FePyr molecules. In (b) the layer consists of 99% FePyr which is annealed to 423 K for 10 minutes in the presence of Ni resulting in image (d). The layer still consists of 99% FePyr, no NiPyr is detected. As described in the images above in this chapter the green arrow indicates a NiPyr molecule with the amount of NiPyr supplied above

the image (a) in green. The blue arrow indicates a CuPyr molecule with the amount of CuPyr supplied above the image (a) in blue. The arrow pointing from image (a) to image (c) indicates the annealing step (10 min, 423 K) in the presence of Fe (0.9 Fe atoms per pyrphyrin molecule). The white arrow in (c) indicates a molecule that is either CuPyr or NiPyr which cannot be identifies with the tunnelling conditions used (see Table 12.1). The yellow arrows indicate FePyr molecules with the respective amounts of FePyr molecules supplied above (b) and below (c, d) the STM images. The arrow from (b) to (d) indicates the annealing step (423 K, 10 min) in the presence of a small surplus of Ni, namely 1.2 eq. which are 1.2 Ni atoms per pyrphyrin molecule.

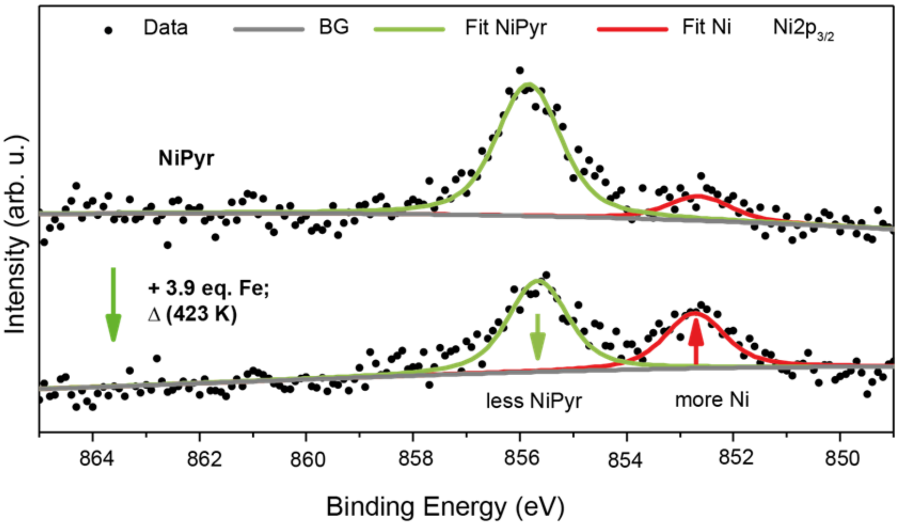

**Figure 7.8:** XPS study on the metal atom exchange reaction from NiPyr to FePyr. For this a monolayer of NiPyr with some excess metallic Ni is annealed in the presence of 3.9 eq. of Fe (= Fe atoms per molecule) at 423 K for 10 min. The NiPyr peak at 855.8 eV is reduced in intensity and the peak of metallic Ni at 852.8 eV is increased in intensity. The XP spectra are vertically off-set for clarity.

All the previous experiments are conducted with an annealing step. The next experiment shows that the exchange of Cu with Fe already partially takes place at room temperature. For this a monolayer of CuPyr is prepared. Onto this monolayer a trace amount of Fe is supplied (~0.9 Fe atoms per molecule). The resulting STM image shows that after the addition of Fe 30% of the pyrphyrin molecules are present as FePyr (Figure 7.9).

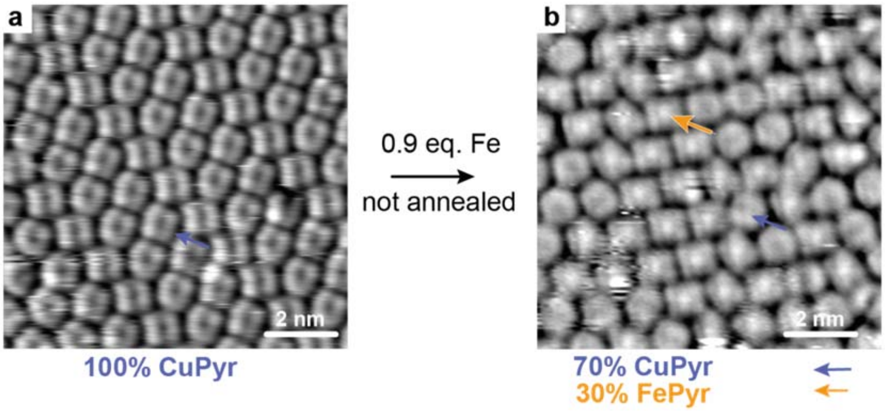

**Figure 7.9:** STM images obtained on a monolayer of CuPyr (a) onto which 0.9 eq. Fe (= Fe atoms per molecule) are evaporated (b). Without annnealing already ~30% of the molecules are present as FePyr. The blue arrows indicate CuPyr molecules with the respective amount of CuPyr molecules written in blue supplied below the STM images. The yellow arrow in (b) indicates an FePyr molecule with the respective amount of FePyr molecules written in yellow supplied below the STM image.

The last experiment showed that Cu can be exchanged with Fe already at room temperature to some extent. This experiment shows that also Ni can be exchanged with Fe at room temperature. For this an excess of Fe (~3 Fe atoms per molecule) is added to a monolayer consisting of 80% NiPyr and 20% CuPyr (Figure 7.10a). Already before annealing, about 50% of the molecules are present as FePyr. It is impossible to identify the remaining molecules as either NiPyr or CuPyr under the employed STM conditions (see Table 12.1). Many metal clusters are present (Figure 7.10b). Annealing this sample to 423 K for 10 minutes leads to an increase of the FePyr amount to 60% (Figure 7.10c).

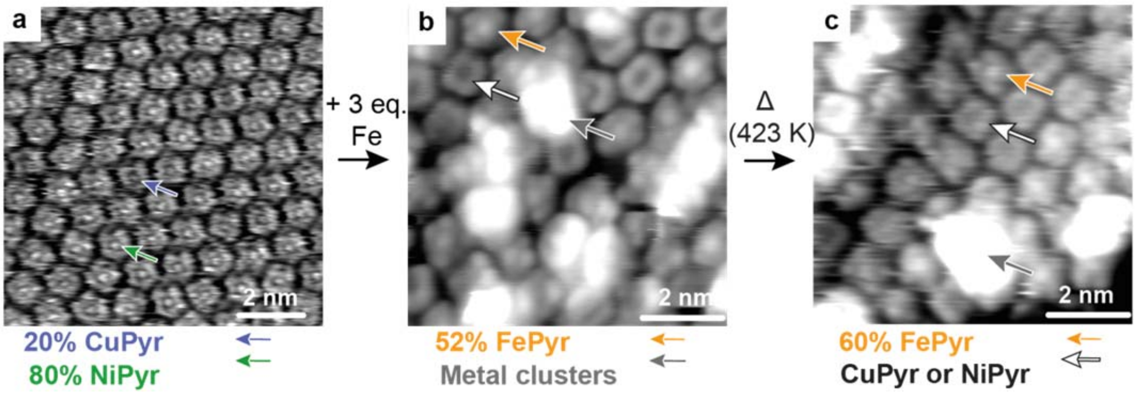

**Figure 7.10:** STM images obtained on a monolayer that consists of 80% NiPyr and 20% CuPyr (a) on which a surplus of ~3 eq. Fe (= Fe atoms per molecule) are added (b). Before annealing (b) already ~50% of the molecules are present as FePyr. Annealing to 423 K for 10 minutes leads to a small increase in the FePyr abundance to 60% (c). The blue arrow indicates a CuPyr molecule with the respective amount of CuPyr molecules supplies below the STM image. The green arrow indicates a NiPyr molecule with the respective amount of NiPyr molecules indicates below the image. The yellow arrows indicate FePyr molecules with the respective amounts of FePyr molecules indicated below the images. The white arrows indicate either CuPyr or NiPyr molecules that cannot be identified with the applied STM tip conditions (see Table 12.1). The grey arrows indicate metal clusters.

These two experiments, where Fe is added to a monolayer of CuPyr (Figure 7.9) and a layer consisting mostly of NiPyr (Figure 7.10) and even before annealing FePyr molecules are found, show that atoms evaporated from the electron beam evaporator are more reactive than Fe on the surface. The occurrence of the central metal exchange may depend on the place where the incoming Fe atom lands with respect to the central metal atom. Note that similar reactions have been observed for the metalation reactions of porphyrins: if the metal atoms are deposited on a molecular layer the metalation reaction is already observed at room temperature. Incorporation of Fe already adsorbed at the surface only occurs if the sample is annealed to about 500 K [40,41].

### 7.1.5 Direct metalation from 2HPyr to NiPyr and FePyr

In all the previous experiments a monolayer of CuPyr was prepared on which the reactions then were carried out. But NiPyr and FePyr can also be easily obtained by direct metalation of 2HPyr. For this, pyrphyrin is evaporated until a monolayer coverage is reached. Onto this monolayer Ni or Fe is sublimated and subsequently annealed to 423 K for 10 min. Figure 7.11a shows a layer consisting of 100% NiPyr and Figure 7.11b shows a layer consisting of 100% FePyr. From the results presented in the previous subchapters it is known that the central metal atom exchange reaction from CuPyr to NiPyr or FePyr is facile. It is therefore possible that the metalation reaction from 2HPyr to NiPyr or FePyr proceeds via CuPyr as an intermediate during the annealing step. Metalation reactions with different transition metals (also Ni and Fe) are already previously reported on Ag and Au surfaces [25,27,28,36,39,40,111].

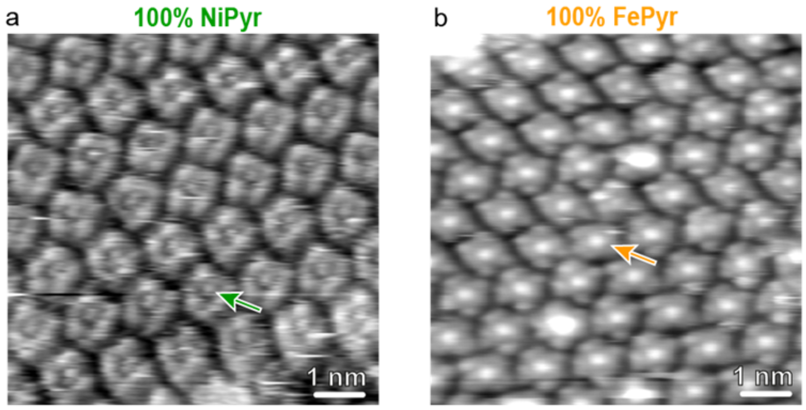

**Figure 7.11:** STM images obtained by (a) the addition of 1 eq. of Ni (1 Ni atom per 1 pyrphyrin molecule) to 2HPyr and annealing to 423 K for 10 min. Image (b) is obtained by the addition of 1 eq. of Fe (1 Fe atom per 1 pyrphyrin molecule) to 2HPyr and annealing to 423 K for 10 min. The green arrow indicates a NiPyr molecule with the respective amount of NiPyr molecules supplied above the image (a) and the yellow image indicates an FePyr molecule with the respective amount of FePyr molecule supplied above the image (b).

## 7.2 Conclusion and Outlook

The above shown experiments on the metalation atom exchange reaction of the central metal atom in pyrphyrin adsorbed at monolayer coverage on Cu(111) allow to rank the stabilities of CuPyr, NiPyr and FePyr. The central metal atom exchange reactions of CuPyr to NiPyr and CuPyr to FePyr proceed easily and with high yield. This means that after annealing a CuPyr monolayer in presence of Ni or Fe nearly all pyrphyrin molecules have the new metal centre instead of Cu. The reverse reaction from NiPyr back to CuPyr was not observed. Annealing NiPyr in the presence of Fe leads to FePyr but with only a moderate yield. The reverse reaction, namely the central metal atom exchange from FePyr to NiPyr, was tried and was found not to occur as well. These findings give rise to the following qualitative stability order: FePyr > NiPyr > CuPyr. This is consistent with the findings from porphyrin chemistry in solution and DFT calculations.

The detailed mechanism of the atom exchange reaction at the solid-vacuum interface remains unknown. It is however likely that the mechanism involves a metal-metal dimer complex where the metal ligand bond switches from the weaker binding to the stronger binding. Such an intermediate state may be similar to the previously found metal-porphyrin complex with a hetero metal atom at cryogenic temperature [112]. In the present case however, it is more likely that the second metal atom arrives from below the macrocycle.

Overall, important thermodynamic and kinetic effects are still unknown. It is unclear if the activation barrier for the metalation of tetrapyrrols such as pyrphyrin is of similar height as in porphyrins or if the tetrapyrrol ligand presents very low reaction barriers. Also the enthalpy and entropy of the metal atoms that are expelled during the atom exchange reaction still need to be investigated [31,47].

# 8 Tartaric Acid Diastereomers on Cu(111)

Results reported in this chapter have been also published in "Chiral Molecules Adsorbed on a Solid Surface: Tartaric Acid Diastereomers and their Surface Explosion on Cu(111)", by A. Rieger, C. Sax, T. Bauert, C. Wäckerlin and K.-H. Ernst, *Chirality* **2018**, *1*,1-9 ([113]).

Tartaric acid (TA) is often used as a model organic molecule for studying adsorption properties such as chirality, self-assembly and desorption properties. It contains two carbon acid groups with which it can bind to the metal surface by deprotonation. TA exists in three different forms that are investigated in this study: the chiral form (either (*R*,*R*)-TA or (*S*,*S*)-TA), the achiral form ((*R*,*S*)-TA) and the racemic form (*rac*-TA), see Figure 8.1a. This molecule is used as a model system mostly on Cu(110) [48,62,114,115] or on Ni(110) [54–56] to understand the chiral crystallisation and its physical properties. Theoretical calculations were also conducted for TA adsorbed on the Cu(110) surface [52,53]. Previous works by Raval [48–51,54] and Ernst [57–60] revealed extended two-dimensional chiral domains and two principle binding modes of the TA diastereomers with the Cu(110) surface. At low coverage and mild annealing the TA molecule is deprotonated at both carboxylic acid groups which both bind to the copper surface. This is the bitartrate form (Figure 8.1b, left). With increasing coverage the incoming TA acids, which are biacids, deprotonate at one carboxylic acid group and the hydrogen is used to protonate one of the bitartrate molecules. This leads to the transition from a bitartrate layer to a monotartrate layer (Figure 8.1b, right). While the chiral and the achiral diastereomers ((*R*,*R*)-TA, (*S*,*S*)-TA and (*R*,*S*)-TA) form homochiral adsorbate layers of the form (4 1, 5 2) in the case of (*R*,*R*)-TA [57,58] the racemate shows a different crystallisation behaviour. The low-coverage bitartrate species forms a 2D conglomerate with homochiral domains [51,59] while the high-coverage monotartrate species forms a 2D racemate lattice of the form (4 0, 2 1) [58]. This difference in packing of the racemate compared to the pure enantiomers leads to the fact that the packing density of the racemate is lower on Cu(110) and the pure enantiomers at identical coverage and lattice periodicity are more stable towards the thermally induced autocatalytic reaction called surface explosion than the racemic layer [57,58,62,116]. On chiral Cu surfaces the surface explosion was also investigated [61,116]. Chiral vacancies are formed which in turn form more chiral vacancies during the autocatalytic decomposition reaction. This gives rise to high enantiospecificity, e.g. (*R*,*R*)-TA on $Cu(531)^R$ desorbs at lower temperature than (*S*,*S*)-TA on this surface.

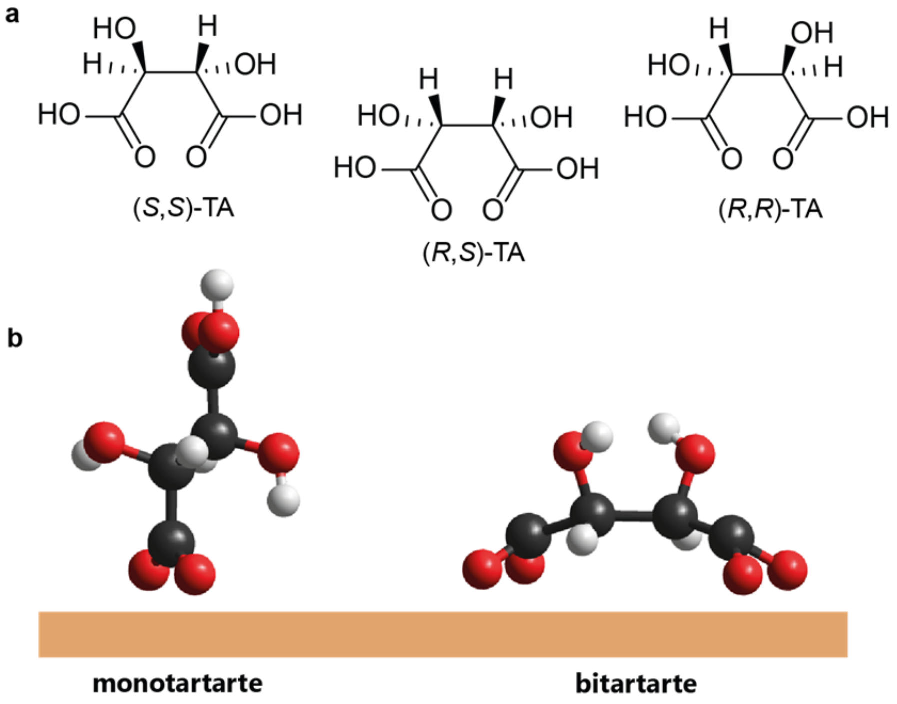

**Figure 8.1:** a) The molecular structures of the TA diastereomers are shown: the chiral enantiomers (*S*,*S*)-TA, (*R*,*R*)-TA and the achiral diastereomer (*R*,*S*)-TA. *rac*-TA which is also used in this study, is a 1:1 mixture of the two chiral enantiomers. b) The two forms in which TA can be present on the Cu(110) surface (monotartrate and bitartrate) are shown.

Two studies of TA diastereomers on Cu(111) were conducted up to now [67,68]. Yan et al. [68] investigated the adsorption and coordination of TA enantiomers on Cu(111) in aqueous solutions. They found that chiral TA adsorbs in a c(4x4) unit cell. Therrien et al. [67] investigated (*R*,*R*)-TA on Cu(111) in vacuo. They found that upon annealing the pure enantiomers form a (10 7, -7 3) phase. This is supported by low electron energy diffraction (LEED) experiments conducted in the group of Ernst [113]. For (*R*,*S*)-TA no structure could be determined using LEED. The surface explosion experiments conducted by Therrien et al. could not be reproduced in this study (see below). They found quite broad surface explosion peaks for coverages from 0.78 ML to 1 ML of (*R*,*R*)-TA. Broad surface explosion peaks indicate that the surface layer is not yet in equilibrium. Unfortunately, no study is found that compares the different enantiomers on Cu(111). Therefore, the question that we investigated is whether the geometry of the copper surface has an influence on the binding of the TA diastereomers to the metal surface and if that is the case, if this discrepancy leads to different chemical behaviour. Thus, the diastereomers (*R*,*R*)-TA, (*R*,*S*)-TA and *rac*-TA are investigated on Cu(111). The focus lies on the comparison between the diastereomers and on the comparison to the previously published data on TA diastereomers on Cu(110). Especially, the adsorption on and desorption from Cu(111) are investigated.

In this chapter the focus lies on the binding of the tartaric acid diastereomers to the copper surface. A specific point of interest is the difference in binding and due to that also the difference in chemical reactions of tartaric acid deposited onto Cu(111) surface compared to deposited onto Cu(110) surface.

## 8.1 Results and Discussion

### 8.1.1 Adsorption of TA on Cu(111) at room temperature

As previously explained in the introduction chapter the three diastereomers of tartaric acid are investigated, namely the chiral (*R*,*R*)-TA, the achiral (*R*,*S*)-TA and the racemic mixture *rac*-TA of the two chiral enantiomers (*R*,*R*)-TA and (*S*,*S*)-TA.

In order to investigate the adsorption chemistry of TA on Cu(111) reflection absorption infrared spectra (RAIRS) are acquired at 320 K (Figure 8.2). The two main features of interest in RAIR spectra are the C=O stretch vibration ($v_{C=O}$) around 1700 $cm^{-1}$ and the symmetric stretch vibration of the carboxylate group ($v_{s(COO)}$) around 1400 $cm^{-1}$. The asymmetric stretch vibration of the carboxylate group, expected at 1594 $cm^{-1}$ [48,117], is not observed in Figure 8.2. This indicates that the two O atoms are equally high above the surface. The RAIRS technique allows to only detect the vibrations where the dipole moment of the investigated molecules changes perpendicularly to the surface. As both oxygens in the carboxylate group interact strongly with the copper surface the change in dipole moment for the asymmetric stretch vibration of the carboxylate is expected to be very small. The area of the two main peaks ($v_{C=O}$ at ~1700 $cm^{-1}$ and $v_{s(COO)}$ at ~1400 $cm^{-1}$) correspond to the surface concentrations of the carboxyl groups (COOH) and the carboxylate (COO) groups. Keeping the Cu(111) substrate at 320 K during the evaporation and the in-situ RAIR measurement both IR vibrations saturate for all three diastereomers. For the evaporation temperatures used here (between 388 K and 403 K depending on the diastereomer) saturation of both IR vibrations are reached after 10 to 20 min.

For the RAIR data acquired for (*R*,*R*)-TA on Cu(111) this indicates that at low coverage, *i.e.* before saturation of the $\nu_{C=O}$ vibration peak, the TA molecules are present as H-bonded structure and upon reaching saturation the H-bonds are dissolved. This behaviour is restricted to the chiral TA and the racemic mixture of the chiral TA enantiomers.

The peak at 1400 cm$^{-1}$ has a low-energy shoulder at 1384 cm$^{-1}$ which is attributed to the OH deformation mode (Table 8.1) [48].

As the experiment was conducted with a cold MCD detector water adsorbed on it and therefore the OH stretch region was not considered reliable for analysis.

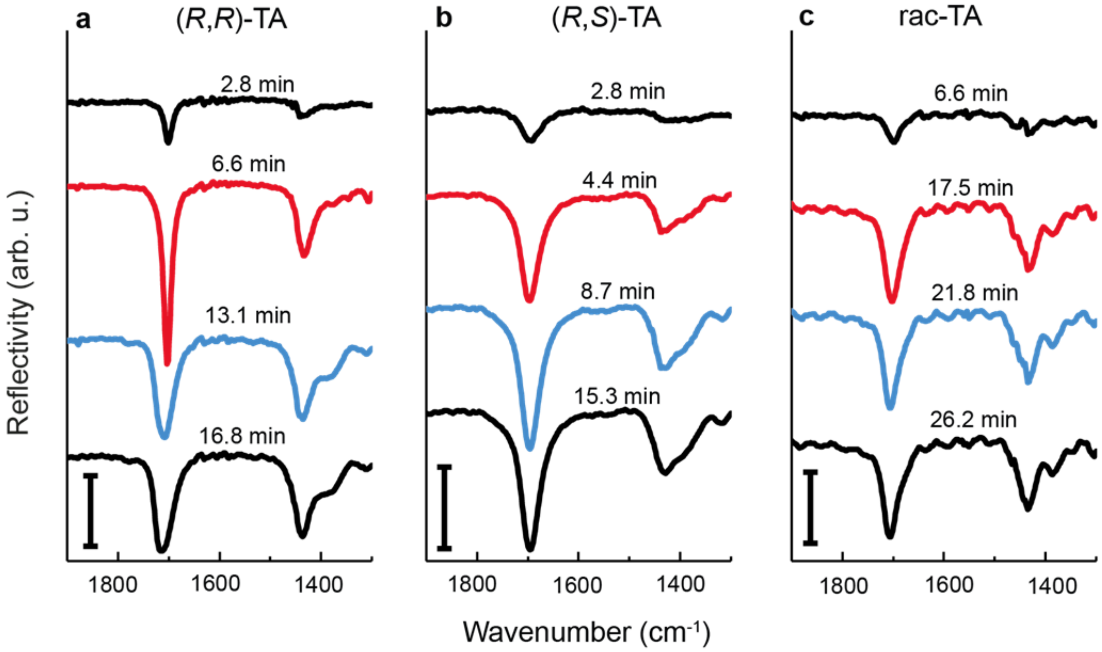

**Figure 8.2:** RAIR spectra obtained *in-situ* during the deposition of the TA diastereomers onto the Cu(111) crystal kept at 320 K. The deposition times are indicated above and the spectra are vertically off-set for clarity. The vertical bars correspond to ΔR/R = 1‰. The fringes in c are due to a measurement artefact.

The integrated peak intensities of the $\nu_{C=O}$ and the $\nu_{s(COO)}$ vibrations at 1700 $cm^{-1}$ and 1400 $cm^{-1}$ respectively are shown in Figure 8.3. The integrated peak areas of the $\nu_{C=O}$ peak at 1700 $cm^{-1}$ saturates (red arrow) before the integrated peak area of the $\nu_{s(COO)}$ peak at 1400 $cm^{-1}$ (blue arrow). This indicates that the deprotonation of the carboxyl group happens slower than the surface adsorption. This is attributed to the kinetics of adsorption close to the saturation of a monolayer. It seems that finding a free surface site for deprotonation takes a longer time than the plain adsorption of the molecule into the layer itself.

As at saturation both vibrations are observed, namely the $\nu_{C=O}$ vibration at 1700 $cm^{-1}$ that is only observed if a carboxyl group is present and the $\nu_{s(COO)}$ vibration at 1400 $cm^{-1}$ which is only observed if a carboxylate group is present, it can be concluded that at 320 K the TA diastereomers are present as monotartrates on the Cu(111) surface.

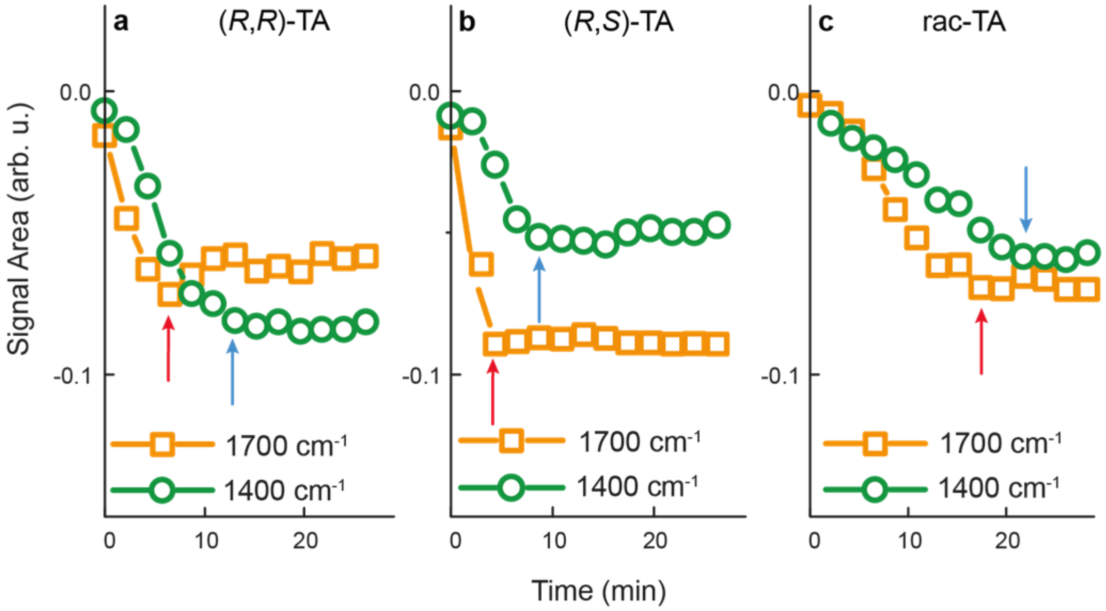

**Figure 8.3:** The peak areas of the $\nu_{C=O}$ and the $\nu_{s(COO)}$ vibration measured at 320 K are plotted versus deposition time. The red arrow marks where the $\nu_{C=O}$ vibration saturates while the blue arrow marks the saturation point of the $\nu_{s(COO)}$ vibration.

Table 8.1 presents the vibrational bands shown in Figure 8.2. "Low coverage" refers to the first or the second spectrum where the integrated intensity of the ~1400 $cm^{-1}$ peak has not jet saturated (submonolayer regime). "High coverage" refers to the spectra where both intensities have saturated (monolayer regime). The vibrational mode at ~1700 $cm^{-1}$ increases in intensity going from low to high coverage which is consistent with the increasing amount of molecules on the surface. This mode experiences a small shift to higher wavenumbers which is due to a different degree of intramolecular hydrogen bonding [48]. However, the shift is small and it is only observed for the chiral (*R*,*R*)-TA and in a lesser degree for *rac*-TA. It seems to be an effect that depends on the stereomer of TA. That the shift is also seen in *rac*-TA indicates that *rac*-TA grows in chiral self-assembled islands.

The symmetric stretch vibration of the carboxylate group $v_{s(COO)}$ which is found at 1435 ± 5 $cm^{-1}$ for all three diastereomers does not show any shift with increasing coverage. This implies that adding more molecules to the surface does not change the binding of the carboxylate oxygen atoms to the Cu(111) surface.

**Table 8.1:** Vibrational modes ($cm^{-1}$) that are extracted from the spectra shown in **Figure 8.2**.

| | **Mode** | **Low coverage** | **High coverage** |
|---|---|---|---|
| **(*R*,*R*)-TA** | $v_{C=O}$ | 1701 | 1714 |
| | $v_{s(COO)}$ | 1435<br>1409 (weak) | 1440<br>- |
| | $\delta_{OH}^{alc}$ | 1384 | 1384 |
| | $\delta_{OH}^{acidic}$ | 1342 | 1347 |
| **(*R*,*S*)-TA** | $v_{C=O}$ | 1695 | 1697 |
| | $v_{s(COO)}$ | 1429<br>1405 (weak) | 1429<br>- |
| | $\delta_{OH}^{alc}$ | 1386 | 1387 |
| | $\delta_{OH}^{acidic}$ | 1343 | 1343 |
| ***rac*-TA** | $v_{C=O}$ | 1695 | 1706 |
| | $v_{s(COO)}$ | 1430<br>- | 1436<br>- |
| | $\delta_{OH}^{alc}$ | 1382 | 1388 |
| | $\delta_{OH}^{acidic}$ | 1338 | 1338 |

The same RAIR experiment was also conducted with the crystal kept at 300 K (Figure 8.4). Table 8.2 gives an overview over the vibrational modes extracted from the spectra shown in Figure 8.4. This experiment shows essentially the same features with the difference that no saturation in the $v_{C=O}$ stretch vibration is observed.

The $\nu_{s(COO)}$ vibration on the other hand saturates after similar exposure times as in the experiment conducted at 320 K. The observation that the $\nu_{C=O}$ vibration does not saturate is assigned to the formation of multilayers. In multilayers, these are layers that are not in direct contact to the Cu(111) surface, the acids are present as neutral biacids. In biacids the C=O double bond is present at both ends of the molecule. The peak of the carboxylate (1400 cm$^{-1}$ region, $\nu_{s(COO)}$ vibration) reflects the interaction of the molecule with the Cu(111) surface and it saturates when the monolayer is completed.

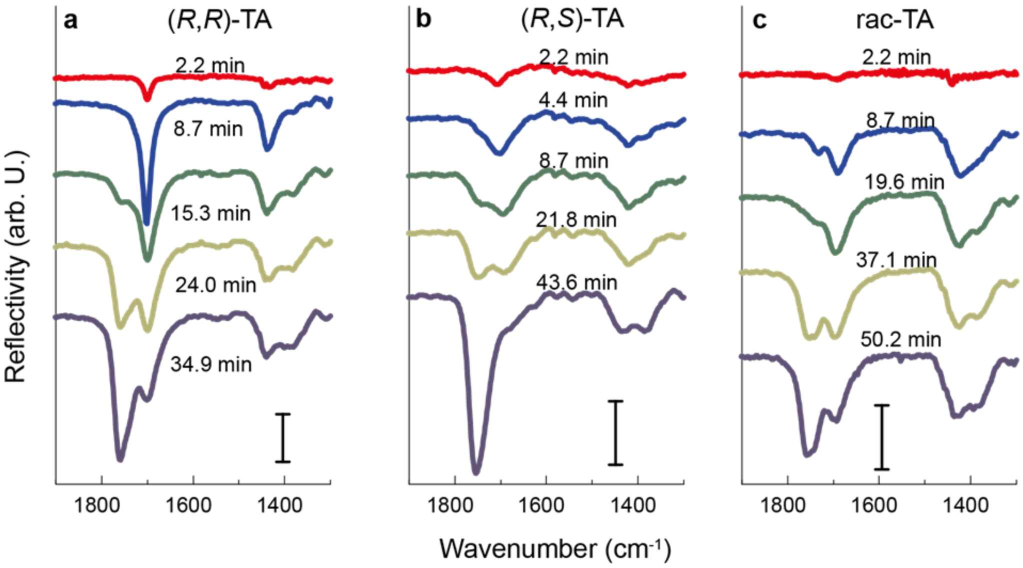

**Figure 8.4:** RAIR spectra obtained in-situ during the deposition of the TA diastereomers onto the Cu(111) crystal kept at 300 K. The deposition times are indicated above and the spectra are vertically off-set vertically for clarity. The vertical bars correspond to ΔR/R = 1‰.

The vibrational modes are summarised in Table 8.2. What can be observed here is that the $\nu_{s(COO)}$ and the $\delta_{OH}$ vibrations remain unchanged compared to the experiment conducted at 300 K. The largest change can be seen in the $\nu_{C=O}$ vibration. At low coverage only one peak is observed at 1700 cm$^{-1}$ in the cases of (*R*,*R*)-TA and (*R*,*S*)-TA. In the case of *rac*-TA already at low coverage this vibration is at lower wavenumbers (1687 cm$^{-1}$) and already a high energy shoulder can be observed. In the cases of (*R*,*R*)-TA and (*R*,*S*)-TA at high coverage a high energy shoulder at 1750-1759 cm$^{-1}$ emerges. The peak at low energy remains unchanged at 1691-1700 cm$^{-1}$. The emergence of the high energy leak is due to the growth of the second layer of TA molecules which is present as biacid. In the second layer the carboxyl group remains not hydrogen bonded and is therefore seen at a higher energy.

**Table 8.2:** Vibrational modes (cm$^{-1}$) that are extracted from the spectra shown in Figure 8.4.

| | **Mode** | **Low coverage** | **High coverage** |
|---|---|---|---|
| **(*R*,*R*)-TA** | $\nu_{C=O}$ | 1701 | 1700 |
| | | - | 1759 |
| | $\nu_{s(COO)}$ | 1439<br>1411 | 1439<br>- |
| | $\delta_{OH}^{alc}$ | 1380 | 1383 |
| | $\delta_{OH}^{acidic}$ | 1343 | 1344 |
| **(*R*,*S*)-TA** | $\nu_{C=O}$ | 1711 | 1691 |
| | | - | 1753 |
| | $\nu_{s(COO)}$ | 1423<br>- | 1434<br>- |
| | $\delta_{OH}^{alc}$ | 1389 | 1385 |
| | $\delta_{OH}^{acidic}$ | 1336 | 1345 |
| ***rac*-TA** | $\nu_{C=O}$ | 1687 | 1691 |
| | | - | 1749 |
| | $\nu_{s(COO)}$ | 1415<br>- | 1429<br>- |
| | $\delta_{OH}^{alc}$ | 1388 | 1385 |
| | $\delta_{OH}^{acidic}$ | 1339 | 1340 |

The integrated signal areas of the peaks in the 1700 cm$^{-1}$ and the 1400 cm$^{-1}$ regions presented in Figure 8.4 are shown in Figure 8.5. The difference in the signal areas compared to the experiment conducted at 320 K is that saturation of the $\nu_{C=O}$ vibration is not observed. The $\nu_{s(COO)}$ vibration saturates (blue arrow) after the same times as in the case at 320 K.

In the case where the TA diastereomers were evaporated onto the Cu crystal kept at 300 K the molecules are also present as monotartrates as in the before reported experiments conducted at 320 K. This is because both vibrations are present at low and at high coverage.

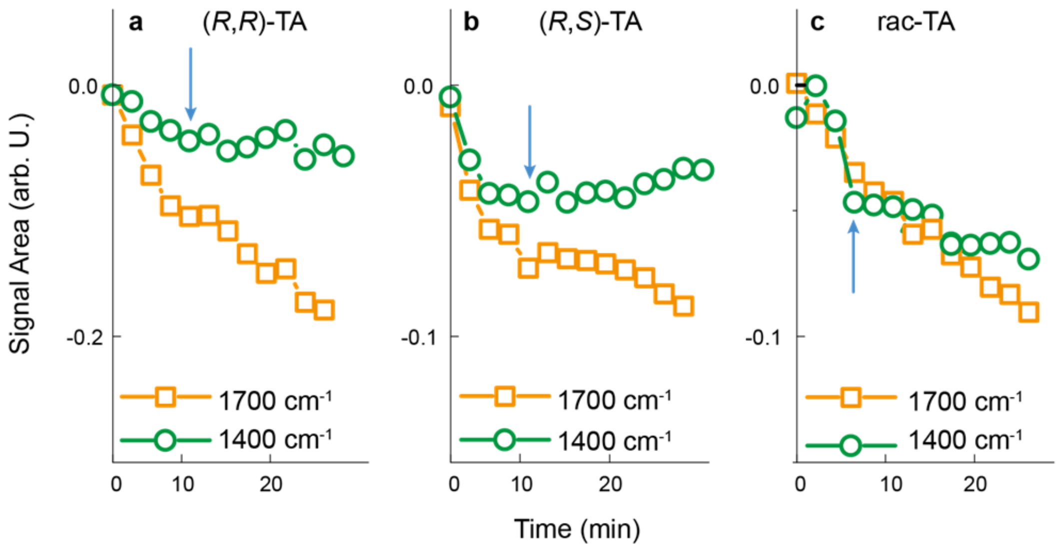

**Figure 8.5:** The peak areas of the $v_{C=O}$ and the $vs_{(COO)}$ vibration measured at 300 K are plotted versus deposition time. The blue arrow marks the saturation point of the $vs_{(COO)}$ vibration.

The above described adsorption chemistry (monotartrate at low and high coverage at room temperature) of the TA diastereomers on Cu(111) at room temperature is the same as for the TA diastereomers on the Cu(110) surface as it was previously investigated by other groups.

### 8.1.2 Adsorption of TA on Cu(111) at elevated temperature

In previously published literature where TA is adsorbed at 405 K on Cu(110) a difference to the adsorption at 300 K is seen [48]. Namely at low coverage at 405 K the acids are present as bitartrate where both acid functionalities are deprotonated and present as carboxylate groups which interact with the copper surface.

Here, the adsorption of (*R*,*R*)-TA on the Cu(111) surface held at 405 K is studied. It shows distinct features in RAIRS that are different from the previously shown data (Figure 8.6a). At low coverages only the vibrational modes in the 1400 $cm^{-1}$ region, namely at 1413 $cm^{-1}$ and 1386 $cm^{-1}$ (see Table 8.3) are seen. The vibrational mode in the 1700 $cm^{-1}$ region is completely missing. This form, where the peaks of the carboxylate vibration ($v_{s(COO)}$) are present and the peak the carboxyl group ($v_{C=O}$) are absent, is assigned to be the bitartrate form. This means that both carboxylate groups bind to the copper surface. At higher coverage the $v_{C=O}$ vibration emerges.

This indicates that at higher coverages a carboxyl group with the C=O bond is present. This is the case for monotartrate where one carboxylate group interacts with the copper surface. The $\nu_{C=O}$ vibrational mode saturates after 10 min (Figure 8.6b) of evaporation. It saturates after the $\nu_{s(COO)}$ vibrational mode reached saturation (6.5 min). This indicates that the protonation of the carboxyl group happens slower than the surface adsorption.

On Cu(110) the same adsorption behaviour was found: at 405 K and low coverages TA is present as bitartrate which turns to monotartrate with increasing TA surface coverage.

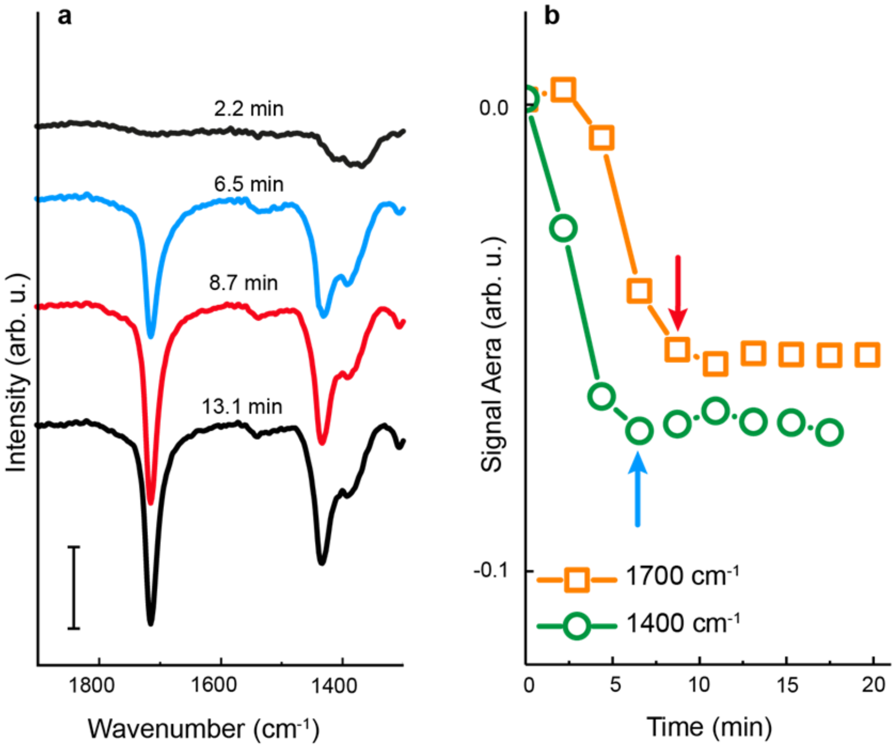

**Figure 8.6:** a) RAIR spectra obtained in-situ during the evaporation of (*R*,*R*)-TA onto the Cu(111) crystal kept at 405 K. The spectra are vertically off-set for visibility and the vertical bar corresponds to ΔR/R = 1‰. The signal areas of the two main regions of interest (1700 $cm^{-1}$ and 1400 $cm^{-1}$ regions) are shown in b. The blue and red arrows mark where the 1400 $cm^{-1}$ peak (blue arrow) and the 1700 $cm^{-1}$ peak respectively (red arrow) saturate.

**Table 8.3:** Vibrational modes (cm$^{-1}$) extracted from the Figure 8.6a for (*R*,*R*)-TA adsorbed on Cu(111) at 405 K.

| | **Mode** | **Low coverage** | **High coverage** |
|---|---|---|---|
| **(*R*,*R*)-TA** | $\nu_{C=O}$ | - | 1714 |
| | $\nu_{s(COO)}$ | 1413<br>1436 (weak) | 1433<br>- |
| | $\delta_{OH}^{alc}$ | 1386 | 1388 |
| | $\delta_{OH}^{acidic}$ | - | 1350 (weak) |

### 8.1.3 XPS analysis of TA diastereomers on Cu(111)

X-ray photo electron spectroscopy is used in order to understand the atomic composition of the molecules on the surface. The aim of using XPS on adsorbed TA diastereomers is to understand how the TA binds to the copper surface, in which form the molecule is present on the surface and if there is a difference between the diastereomers.

In XPS it is expected to see three signals in the C1s region because TA bound to copper in the form of monotartrate has three non-equivalent carbon atoms. In the O1s region it is expected to see 4 signals as monotartrate consists of four non-equivalent oxygen atoms. The non-equivalent carbon and oxygen atoms are indicated in Figure 8.7.

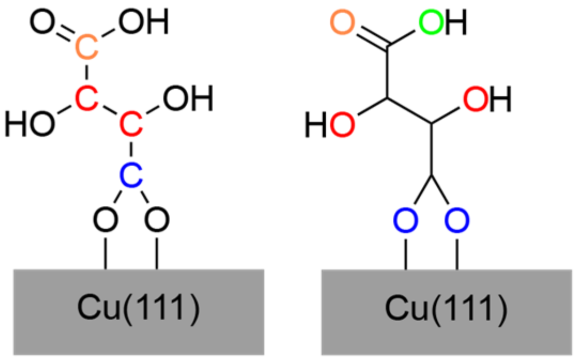

**Figure 8.7:** Indication of the non-equivalent carbon (left) and oxygen (right) atoms in TA bound to the copper surface in the monotartrate form. The colours correspond to the colour of the non-equivalent carbon and oxygen atoms in Figure 8.8.

Figure 8.8 shows the C1s and O1s XP spectra for all three diastereomers on Cu(111). The samples were prepared by evaporation of multilayers of the respective diastereomers onto the crystal kept at 300 K which is followed by an annealing step of 10 min at 363 K. Annealing led to the desorption of the multilayers of TA leaving a saturated monolayer behind. The absolute number of molecules on the surface in a saturated monolayer is similar for all three diastereomers (Table 8.4). The first thing that catches the readers eye is that the line shapes of the C1s and O1s spectra are very similar for all three diastereomers.

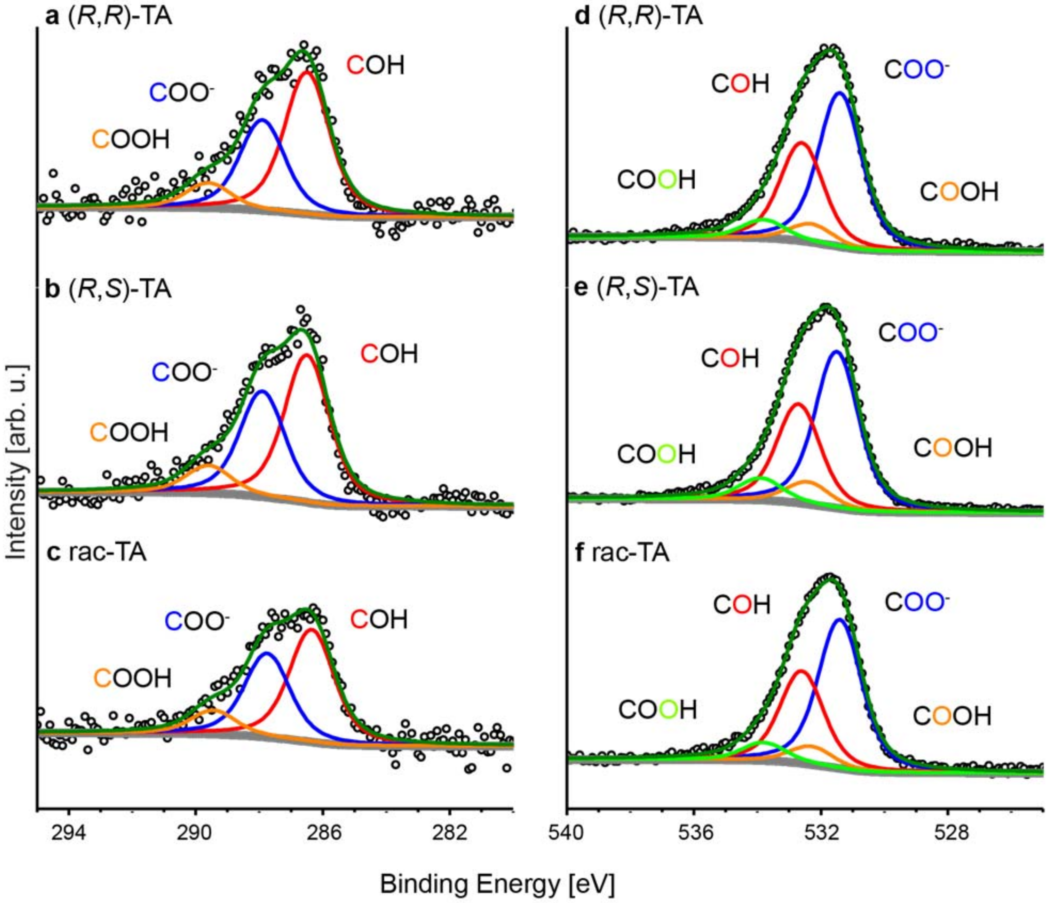

**Figure 8.8:** C1s (left) and O1s (right) spectra at monolayer coverage for (*R*,*R*)-TA (a, d) (*R*,*S*)-TA (b, e) and *rac*-TA (c, f). The coloured lines refer to the components in the C1s and O1s region that are attributed to the carbon and oxygen atoms that are non-equivalent. The grey line denotes the background measured on clean Cu(111) and the dark green line denotes the sum curve. The XP spectra are vertically off-set for clarity.

**Table 8.4:** C1s and O1s binding energies of the deconvoluted peaks in Figure 8.8 and the corresponding peak ratios. Background correction and peak areas are determined according to the procedure described in Chapter 5.2.

<table>
<tr><td colspan="12"><b>C1s binding energies (eV)</b></td></tr>
<tr><td colspan="4">C*OH</td><td colspan="4">C*(OO)-</td><td colspan="4">C*OOH</td></tr>
<tr><td colspan="4">286.5 (a)</td><td colspan="4">287.9 (a)</td><td colspan="4">289.6 (b)</td></tr>
<tr><td colspan="12"><b>O1s binding energies (eV)</b></td></tr>
<tr><td colspan="3">C(OO)*-</td><td colspan="3">CO*H</td><td colspan="3">CO*OH</td><td colspan="3">COO*H</td></tr>
<tr><td colspan="3">531.4[a,b]</td><td colspan="3">532.7[a]</td><td colspan="3">532.3[b]</td><td colspan="3">533.8[b]</td></tr>
<tr><td colspan="12"><b>Integrated intensities and intensity ratios</b></td></tr>
<tr><td colspan="3"></td><td colspan="3">C1s (cps)</td><td colspan="3">O1s (cps)</td><td colspan="3">C*OH:C*(OO)-:C*OOH</td></tr>
<tr><td colspan="3">(<i>R</i>,<i>R</i>)-TA</td><td colspan="3">7272</td><td colspan="3">38726</td><td colspan="3">2 : 1.28 : 0.36</td></tr>
<tr><td colspan="3">(<i>R</i>,<i>S</i>)-TA</td><td colspan="3">6701</td><td colspan="3">39996</td><td colspan="3">2 : 1.40 : 0.40</td></tr>
<tr><td colspan="3"><i>rac</i>-TA</td><td colspan="3">6196</td><td colspan="3">37010</td><td colspan="3">2 : 1.48 : 0.42</td></tr>
<tr><td colspan="9">Ratio expected for monotartrate</td><td colspan="3">2 : 1 : 1</td></tr>
</table>

a: from ref. [61], b: from ref. [19]

If the XPS data are fit with components of fixed binding energies that are previously reported in literature for (*R*,*R*)-TA on Cu(531) [61] and terephthalic acid on Cu(100) [19] (see Table 8.4), they can be fully explained. The XP spectra are deconvoluted with symmetric Voigt functions where the widths are fixed (Gaussian FWHM: 1.2 eV, Lorentzian FWHM: 0.8 eV). The ratio between the C*OH : C*OO- : C*OOH areas was the only free parameter in this deconvolution (see Table 8.4). The ratios in the C1s signal for the TA diastereomers are very similar. In the O1s region the data were deconvoluted with the intensities of the C(OO)*- : CO*H : CO*OH : COO*H which are previously known from the deconvolution of the C1s data and the fixed binding energies from literature. This deconvolution agrees very well with the experimental data and thus confirms also the ratios found from the C1s deconvolution.

Assuming that the TA diastereomers are present as monotartrate in a fully saturated monolayer one would expect to find 50% of the carboxylic acids to be deprotonated. The deprotonated group would interact with the copper surface while the other, still protonated group, points away from the surface. This should give a ratio of 2 : 1 : 1 for C*OH : C*(OO)- : C*OOH. But the experimental data show a different behaviour (Table 8.4): the experimentally acquired ratio is 2 : 1.4 : 0.4, which means that more carboxylic acid groups are deprotonated than expected. Even considering that the exact binding energy position of the C*OOH component can influence this ratio. In the end the amount of carboxylic acid groups is still significantly too low. Other researchers reported similar XP spectra for (*R*,*R*)-TA and (*S*,*S*)-TA at monolayer coverage where the C*OOH signal was also too low but they did not offer an explanation [61]. Malic acid which belongs to the same family of acids as tartaric acid (lacking one hydroxyl group compared to TA) also showed too low C*OOH signal in XPS but again the problem of the too low C*OOH signal is not addressed [118,119]. An idea would be to explain the lower-than-expected COOH signal by the coexistence of bitartrate and monotartrate. Unfortunately, the RAIRS data cannot help to resolve this issue. This is mainly because the visibility of vibrations in RAIRS depends on the angle of the said vibration compared to the surface normal. If the vibration has a change in its dynamic dipole moment perpendicular to the surface (parallel to the surface normal) then the vibration is seen in RAIRS data. With increasing angle compared to the surface normal the visibility of the vibration in RAIRS decreases. Therefore it is only possible to identify a functional group if a vibration is present but it is not possible to infer its absence if the vibration is not observed. The bitartrate phase is mainly characterised by the absence of the $v_{\mathrm{C=O}}$ vibration and the presence of the $v_{s(\mathrm{COO})}$ vibration. Unfortunately, the $v_{s(\mathrm{COO})}$ vibration of the monotartrate phase is in the same range as the $v_{s(\mathrm{COO})}$ vibration of the bitartrate phase. Thus, the explanation for the lower-than-expected COOH amount can only be given based on the low COOH signal inferred from the XPS signal.

As the puzzle of the missing hydrogen atoms could not be solved up to now, including the here presented data, more experiments need to be conducted to find out where the missing hydrogen is.

### 8.1.4 Desorption of TA diastereomers from Cu(111)

The easiest way to study the thermal desorption of small molecules from a metal surface is thermal desorption spectroscopy (TDS). TA is known for its surface explosion behaviour if desorbed from Cu(110) [58,62,116]. This means that for increasing coverage the peak of m / z = 44, which is the mass of $CO_2$, gets bigger but at the same time narrower and higher until, when the TA layer on the Cu surface is fully saturated, the m / z = 44 peak takes on the form of a δ peak with peak widths below 2 K [57,62].

In Figure 8.10 the desorption chemistry of the TA diastereomers on Cu(111) at increasing coverage until saturation is reached, is shown. The decomposition of the adsorbed TA molecule happens through a free site on the copper surface. The fragments leave the surface leaving behind new free sites that can in turn catalyse the decomposition of another adsorbed TA molecule. This process happens exponentially. In the decomposition process (Figure 8.9) the TA molecule beaks apart into the fragments $CO_2$, $H_2O$ and $H_2$. Especially $CO_2$ and $H_2$ can be recorded by mass spectrometry. With TDS, which monitors the evolution of the gases, the decomposition process can be traced.

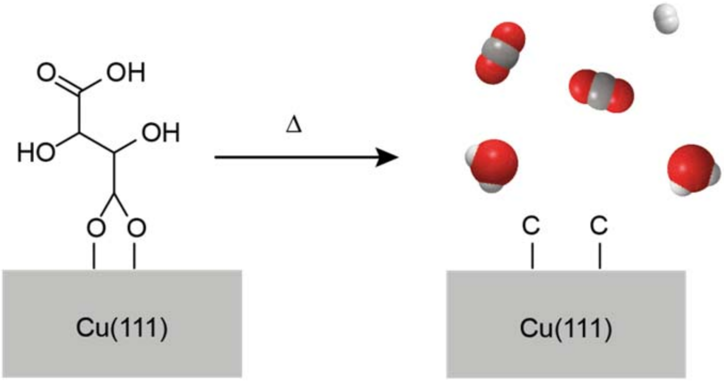

**Figure 8.9:** Decomposition process of TA adsorbed on a copper surface.

For the three diastereomers the TD spectra where the evolution of the partial pressure of $CO_2$ is monitored and they look practically identical (Figure 8.10). Even more, they look very similar to the TD spectra measured at increasing coverages of TA on C(110) [57,58,62]. At low coverages (red to yellow lines) the $CO_2$ partial pressure peaks are small and broad. The maxima of these peaks are found in the range of 450 to 460 K and do not shift to higher temperatures with increasing coverage. This is an indication for bitartrate at low coverages which is similar to the findings on Cu(110) [57,58].

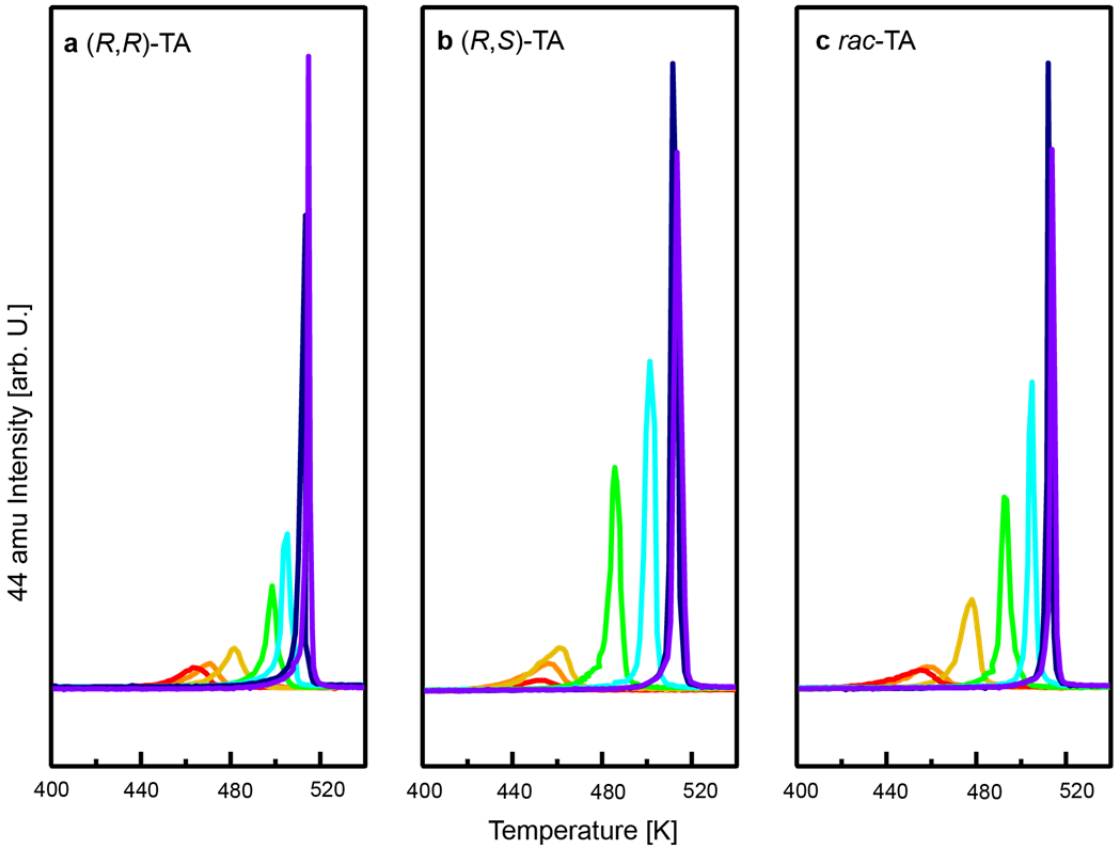

**Figure 8.10:** Temperature desorption spectra showing the $CO_2$ partial pressure versus temperature of (*R*,*R*)-TA (a), (*R*,*S*)-TA (b) and *rac*-TA (c). The red spectra are measured at low coverage. The coverage increases until saturation is reached (violet).

With increasing coverage the peak maxima start to shift strongly to higher temperatures. The line shape of the peaks becomes narrower and higher until at saturation, which is found between 512 and 514 K, the surface explosion peak is very narrow (FWHM ~2 K). Figure 8.11 shows a zoom-in on the surface explosion peaks of the three diastereomers.

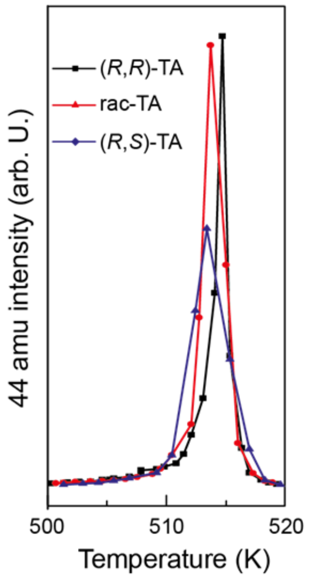

**Figure 8.11:** Comparison of the surface explosion peaks for the saturated monolayers of (*R*,*R*)-TA (black), (*R*,*S*)-TA (blue) and *rac*-TA (red).

The surface explosion for all three TA diastereomers happens between 512 to 514 K, which is different from the surface explosion on Cu(110) where the surface explosion of *rac*-TA happens 8 K lower than the one of (*R*,*R*)-TA [57]. What is obvious from Figure 8.11 is that the surface explosion happens faster than the measurement interval (ca. 0.25 s per point). This leads to undersampling of the surface explosion peak and therefore the peaks appear broad and, especially in the case of the (*R*,*S*)-TA peak, skewed. The fact that the surface explosion happens for all three diastereomers at the same temperature (within sampling resolution) indicates that the homogeneity of the surface assembly of (*R*,*R*)-TA, (*R*,*S*)-TA and *rac*-TA on Cu(111) are on the same order.

A previously published report on the surface explosion of (*R*,*R*)-TA on Cu(111) showed a different behaviour [67]. At intermediate coverages (0.78 - 0.93 ML) broad peaks with shoulders were found. Broad peaks are an indication of higher heterogeneity in the layer possibly due to transition from one lattice to another. The here presented data do not show this kind of heterogeneity suggesting that the (*R*,*R*)-TA layer could relax. In the previously published surface explosion the final peak is very broad (~10 K) and has its maximum at 506 K. It is unclear where the difference of the TD peak appearance between the data of Therrien et al. [67] and the TD data in this thesis comes from.

## 8.2 Conclusion and Outlook

The adsorption and the desorption chemistry of the three TA diastereomers, (*R*,*R*)-TA, (*R*,*S*)-TA and *rac*-TA on Cu(111) were studied. Through RAIR and XP spectroscopy experiments show that the adsorption chemistry is the same for the diastereomers and is very similar to the adsorption chemistry of the TA diastereomers found on Cu(110). RAIRS experiments showed the formation of monotartrate at low temperatures. At high temperatures bitartrate is formed at low coverage which then transforms into monotartrate at high coverage. XPS experiments performed on monolayers where first multilayers of TA were desorbed from, showed very similar C1s and O1s signals as they were previously published on the TA on Cu(531) system. They even showed a low amounts of the COOH component, where more than half of the monotartrate molecules are deprotonated at the carboxylic acid group. The here gathered data did not help to find out why that many monotartrates are deprotonated and where the missing hydrogen atoms went. Further studies need to be conducted to find an answer to this puzzle.

The decomposition chemistry of the three TA diastereomers, which was measured through the autocatalytic surface explosion decomposition reaction, does not show a difference. This contrasts the findings of TA on Cu(110). There, the racemic mixture has its surface explosion at an 8 K lower temperature than the chiral TA. In the here presented data all three diastereomers have their surface explosion at the same temperature.

Bicarboxylic acids are known to restructure the Cu(110) surface upon adsorption and annealing. It could be possible that the more closely packed Cu(111) surface also undergoes surface restructuring upon adsorption and annealing of TA.

The next step is to study the restructuring of the Cu(110) surface due to TA adsorption. The idea is to find a suitable method that allows to see how TA restructures the surface atoms.

# 9 XPD Study on Tartaric Acid on Cu(110)

Chiral organic molecules adsorbed on a metal surface can induce their intrinsic chirality onto the achiral surface. This can be used in the fabrication of chiral nanostructures that are made by the chiral etching method [120]. Many molecules with a carboxylic acid functionality also induce a faceting of the metal surface [121].

The pure tartaric acid (TA) enantiomers are known to self-assemble in chiral domains on Cu(110) [44,46,49–51]. It is even known that a small amount of a chiral sergeant ((*R*,*R*)-TA) can induce the growth of a chiral layer of an achiral molecule such as succinic acid [115]. Other biacids such as malic or fumaric acid are known to chirally reconstruct the Cu(110) surface they are adsorbed on [118,122]. On a nickel surface it is known that the adsorbed TA creates a chiral footprint [54,55]. It is therefore assumed that chiral TA also creates a chiral reconstruction of the Cu(110) surface. There are some indications that chiral TA if adsorbed on Cu(110) creates a reconstruction of the copper surface. Lawton et al. [114] found that chiral TA in the monotartrate state can chirally imprint the copper surface. Using scanning tunneling microscopy (STM) and LEED they found atom deep trenches in the copper surface that are created through the adsorption of (*R*,*R*)-monotartrate.

It is not known if by the adsorption of the chiral TA copper atoms from the top layer are moved from their original position. To discover such a repositioning a surface sensitive method that gives structural information is needed such as XPD. One would expect that only the Cu atoms experience a repositioning to which the TA molecule binds via its oxygen atoms. XPS allows focussing on these Cu atoms as they are expected to experience an upshift by 0.5 to 1 eV through the adsorption of TA via its oxygen atoms. Once the binding energy is identified at which the oxygen shifted Cu atoms are found, an XPD experiment could be run at this energy to get the structural information on the imprinting of the chiral TA on the top layer of the Cu atoms.

## 9.1 Theoretical consideration

It is expected that TA adsorbed on a Cu(110) surface reconstructs or imprints the copper surface making it chiral [114]. Before starting the XPD experiments it is important to get an impression of how prominent the imprinting effect is. For this, let us consider the surface assembly of a saturated bitartrate monolayer, where carboxylic acid functionalities are deprotonated and interact with the Cu surface as carboxylate (Figure 9.1). (*R*,*R*)-bitartrate assembles in a (1 2, −9 0) superstructure. The unit cell is indicated by red lines. In this unit cell, 3 TA molecules and 18 Cu atoms form the top layer (grey) are present. Assuming that every TA molecule on the surface moves two to four Cu atom out of place, this results in 6 to 12 atoms per unit cell to be displaced. Therefore, the reconstruction would effect to 1 / 3 to 2 / 3 of the surface Cu atoms.

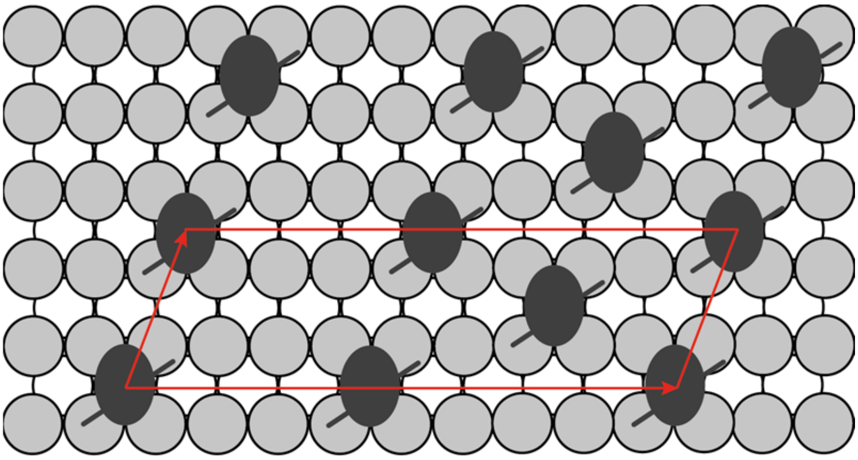

**Figure 9.1:** Surface arrangement of (*R*,*R*)-TA on a Cu(110) surface in the (1 2, −9 0) unit cell [52,53].

The next step is to analyse how much of the Cu XPS signal is due to the surface atoms and then of course how much of the surface Cu XPS signal arises from the reconstructed surface atoms. For this consideration, the attenuation length of photoelectrons in a Cu crystal is important. The attenuation length is by definition the thickness of a material where the photoelectrons can pass through with the probability of $e^{-1}$ withough undergoing inelastic scattering. It depends on the kinetic energy of the photoelectrons. The attenuation length (λ) of an electron with the kinetic energy of 554 eV in copper is 0.89 nm [123]. The kinetic energy of 554 eV corresponds to the difference between the excitation source energy of the Al $K_\alpha$ line and the binding energy of the Cu $2p_{3/2}$ peak. The effective sampling depth is angle dependant, it decreases by a factor of cos(θ) with increasing θ angles.

The lattice constant of Cu is 0.361 nm [124]. Therefore, considering that a Cu(110) crystal is face-centered cubic, the distance between the planes is 0.181 nm per layer. The sampling depth, which is defined as the depth from which 95% of the photoelectrons are scattered by the time they reach the surface, is three times the escape path (Λ), which is calculated by $\Lambda = \lambda \cos\theta$. Therefore, the XP signal in the Cu $2p_{3/2}$ peak measured in $\theta = 0°$ position comes from the top 15 layers of Cu(110) planes. In grazing emission ($\theta = 83°$) the XP signal comes from the top 4 layers. In the case of normal emission 2% to 5% of the XP signal arise from the reconstructed Cu atoms, whereas in the case of grazing emission 8% to 17% of the XP signal would arise from the reconstructed Cu atoms. This indicates that the expected effect is small but in grazing emission it should still be visible.

## 9.2 Experimental consideration

In the XPD experiments conducted in this study the data is collected by five chaneltrons. The centre channeltron, that is later on called channel 1, is set on the binding energy of interest, which is 932.8 eV. The other channeltrons are arranged around the centre at a fixed difference of ± 1.3 eV and ± 2.5 eV. Channel 4 is located at 934.1 eV, channel 3 at 931.5 eV, channel 2 at 932.3 eV and channel 5 at 930.3 eV. Channel 5 serves as internal background. This internal background is needed in order to normalise the data from the channels so that the XPD data collected from different experiments can be compared. The normalisation procedure is the following: the XPD data of channel 1, or any other channel of interest, is divided by the data of channel 5.

The binding energy of a Cu atom interacting with an oxygen atom from the TA molecule is expected to be upshifted by 0.5 to 1 eV. However due to the small amount of atoms interacting with TA and the huge contribution from the bulk Cu atoms, we could not resolve the exact position of this peak. Thus, the data of both channels, 1 and 4 (932.8 eV and 934.1 eV respectively) will be shown hoping that channel 4 contains some information on the Cu atoms that experience a shift due to the binding to the oxygen atoms of TA.

## 9.3 Results and Discussion

### 9.3.1 XPS on (*S*,*S*)-TA and (*R*,*R*)-TA

A full layer of (*S*,*S*)-TA in bitartrate form is created by evaporation of this molecule onto the Cu(110) crystal kept at 405 K. The evaporation at elevated temperature ensured that most of the TA assembled as bitartrate. Figure 9.2 shows the XP spectra taken before and after XPD measurement on a (*S*,*S*)-TA bitartrate layer on Cu(110). The XPS method is used in order to check if TA assembled as bitartrate and to check how strong the beam damage is after the long XPD scan. The XP spectra are deconvoluted into the different chemical groups of interest, *i.e.* C*OO$^{-}$, C*OH, C(OO)*$^{-}$ and CO*H. Table 9.1 summarises the peak positions and ratios.

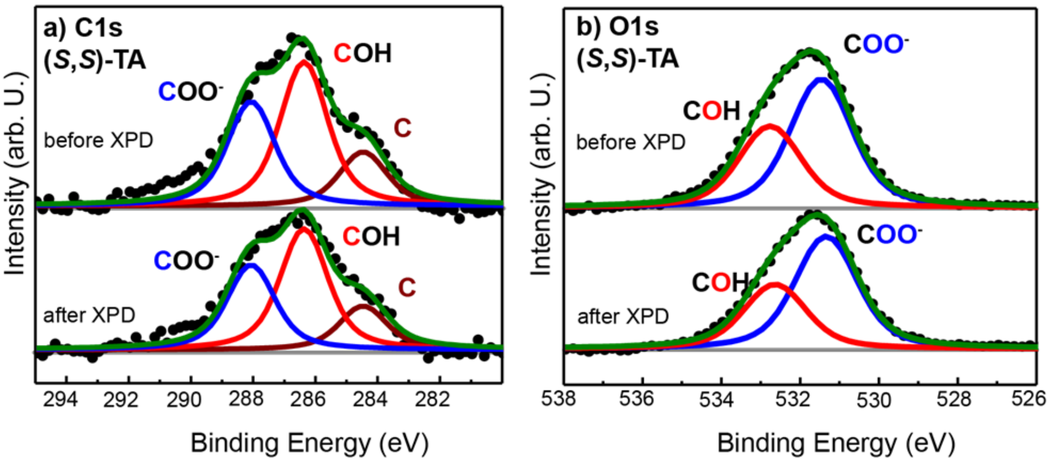

**Figure 9.2:** XP spectra of (*S*,*S*)-TA on Cu(110) in the bitartrate form (9 0, −1 2) showing the C1s region (a) before (top) and after (bottom) the XPD experiment and the O1s region (b) before (top) and after (bottom) the XPD experiment. The coloured lines refer to the components in the C1s and O1s region respectively which are attributed to the non-equivalent carbon and oxygen atoms (blue: C*OO$^{-}$ and C(OO)*$^{-}$, red: C*OH and CO*H, brown: carbon). The green line denotes the sum curve and the grey line denotes the background measured on clean Cu(110). The XP spectra are off-set for clarity. The XP peaks are normalised to the substrate.

**Table 9.1:** Summary of the peak positions and ratios of the fitted chemical groups in Figure 9.2. Background correction and peak areas are determined according to the procedure described in Chapter 5.2.

<table>
<tr><td><b>C1s binding energies (eV)</b></td><td>C*OH</td><td colspan="2">C*OO-</td><td>C</td></tr>
<tr><td>Before XPD</td><td>286.4</td><td colspan="2">288.1</td><td>284.4</td></tr>
<tr><td>After XPD</td><td>286.4</td><td colspan="2">288.1</td><td>284.5</td></tr>
<tr><td><b>O1s binding energies (eV)</b></td><td colspan="2">C(OO)*-</td><td colspan="2">CO*H</td></tr>
<tr><td>Before XPD</td><td colspan="2">531.5</td><td colspan="2">532.8</td></tr>
<tr><td>After XPD</td><td colspan="2">531.4</td><td colspan="2">532.7</td></tr>
<tr><td colspan="3"><b>Ratios C1s</b></td><td colspan="2">Expected</td></tr>
<tr><td>C*OH:C*OO-:C (before XPD)</td><td colspan="2">1 : 0.95 : 0.85</td><td colspan="2">2 : 2 : 0</td></tr>
<tr><td>C*OH:C*OO-:C (after XPD)</td><td colspan="2">1 : 0.67 : 0.37</td><td colspan="2"></td></tr>
<tr><td colspan="3"><b>Ratios O1s</b></td><td colspan="2">Expected</td></tr>
<tr><td>C(OO)*- : CO*H (before XPD)</td><td colspan="2">1 : 0.61</td><td colspan="2">4 : 2</td></tr>
<tr><td>C(OO)*- : CO*H (after XPD)</td><td colspan="2">1 : 0.55</td><td colspan="2"></td></tr>
</table>

Analysis of the peak ratios shows that before the XPD experiment the C*OH : C*OO$^-$ ratio is 1 : 0.95 which is very close to the expected 1 : 1 ratio of bitartrate. There is a carbon peak in the C1s spectra Figure 9.2a at 284.5 eV which is not identified but is present at a high ratio (1 : 0.85 for C*OH : C). This peak was already previously observed on (*R*,*R*)-TA and (*S*,*S*)-TA on Cu(531) [61], where it is identified as dissociation product. The origin of this dissociation product remains unclear.

The largest change from the XP spectra before the XPD experiment to the spectra after the experiment is seen in the C*OH : C*OO$^-$ ratio. Where before the XPD experiment the ratio was nearly 1 : 1 as it is expected for bitartrate, after the experiment it decreased to 1 : 0.67. This means that after the XPD experiment less of the chemical C*OO$^-$ group is found. This loss could indicate that the prolonged irradiation with X-rays result in the desorption of $CO_2$ from the molecule.

In the next step we repeated the same experiments with a saturated layer of (*R*,*R*)-TA in the bitartrate form (1 2, −9 0). For the preparation of the layer, the same procedure that was used to prepare the (*S*,*S*)-TA layer was employed. Figure 9.3 shows the deconvoluted XPS spectra of the bitartrate layer of (*R*,*R*)-TA before and after the XPD experiment. Table 9.2 gives an overview of the binding energies and the ratios of the C*OH : C*OO$^-$ : C areas and the CO*H : C(OO)*$^-$ areas obtained upon deconvolution.

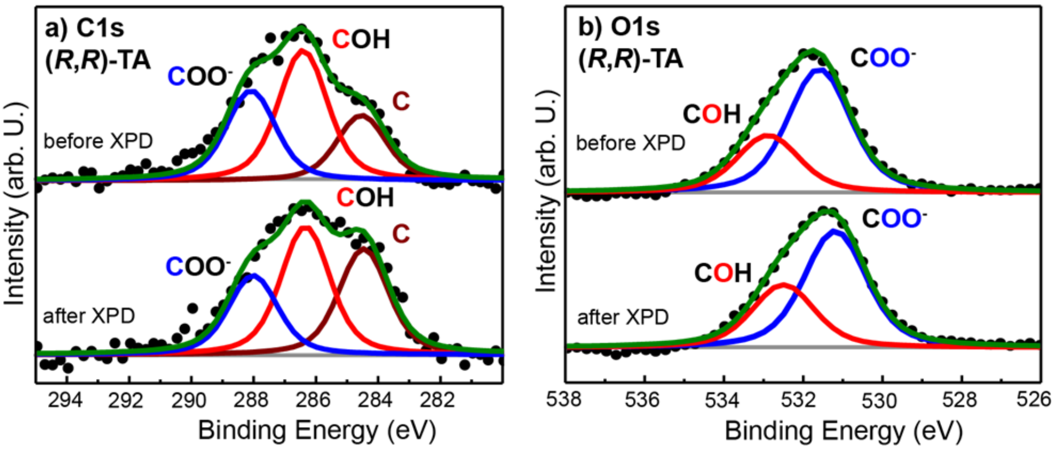

**Figure 9.3:** XP spectra of the C1s region (a) and O1s region (b) before (top) and after (bottom) of the XPD experiment of a bitartrate layer of (*R*,*R*)-TA in the (1 2, −9 0) form. The spectra are deconvoluted into the COH (red), the COO$^-$ carbon (blue) and an undefined carbon signal (brown). In the O1s region the signal is deconvoluted into the COO$^-$ oxygens (blue) and the COH oxygen (red). The green line denotes the sum curve while the grey line denotes the background measured on clean Cu(110). The XP spectra are off-set for clarity.

**Table 9.2:** Summary of the binding energies and the ratios of the fitted peaks in Figure 9.3 before and after the XPD experiment of a layer of bitartrate of (*R*,*R*)-TA on Cu(110). Background correction and peak areas are determined according to the procedure described in Chapter 5.2.

<table>
<tr><td><b>C1s binding energies (eV)</b></td><td>C*OH</td><td colspan="2">C*OO-</td><td>C</td></tr>
<tr><td>Before XPD</td><td>286.5</td><td colspan="2">288.1</td><td>284.5</td></tr>
<tr><td>After XPD</td><td>286.4</td><td colspan="2">288.0</td><td>284.5</td></tr>
<tr><td><b>O1s binding energies (eV)</b></td><td colspan="2">C(OO)*-</td><td colspan="2">CO*H</td></tr>
<tr><td>Before XPD</td><td colspan="2">531.6</td><td colspan="2">532.9</td></tr>
<tr><td>After XPD</td><td colspan="2">531.2</td><td colspan="2">532.5</td></tr>
<tr><td colspan="3"><b>Ratios C1s</b></td><td colspan="2">Expected</td></tr>
<tr><td>C*OH:C*OO$^-$:C (before XPD)</td><td colspan="2">1 : 0.94 : 0.91</td><td colspan="2">2 : 2 : 0</td></tr>
<tr><td>C*OH:C*OO$^-$:C (after XPD)</td><td colspan="2">1 : 0.58 : 0.79</td><td colspan="2"></td></tr>
<tr><td colspan="3"><b>Ratios O1s</b></td><td colspan="2">Expected</td></tr>
<tr><td>C(OO)*$^-$ : CO*H (before XPD)</td><td colspan="2">1 : 0.46</td><td colspan="2">4 : 2</td></tr>
<tr><td>C(OO)*$^-$ : CO*H (after XPD)</td><td colspan="2">1 : 0.54</td><td colspan="2"></td></tr>
</table>

Like in the case of (*S*,*S*)-TA the ratio before the XPD experiment is as it is expected for bitartrate (1 : 0.94 for C*OH : C*OO$^-$). Again a lot of the dissociation product at 284.5 eV is found. After XPD the ratio decreases to 1 : 0.58 (C*OH : C*OO$^-$), which indicates that the same process happens as for (*S*,*S*)-TA which is termed desorption of $CO_2$ during the XPD experiment.

### 9.3.2 XPD on (*S*,*S*)-TA and (*R*,*R*)-TA

In Figure 9.4 the collected XPD data are shown as stereographic representation. On the left the stereographic representation of the clean Cu(110) surface is shown. It is normalised by dividing the data collected at 932.8 eV (channel 1) with the data collected at 930.3 eV (channel 5). The same normalisation is used for the stereographical representations of a (*S*,*S*)-TA (middle) and a (*R*,*R*)-TA bitartrate layer (right). Apart from the slightly reduced brightness of the stereographical representations of a (*S*,*S*)- or (*R*,*R*)-bitartrate monolayer there is no difference visible to the stereographical representation of clean Cu(110). It is therefore important to do a background subtraction where the data obtained on the clean Cu(110) is subtracted from the data obtained on a (*S*,*S*)-TA or (*R*,*R*)-TA layer.

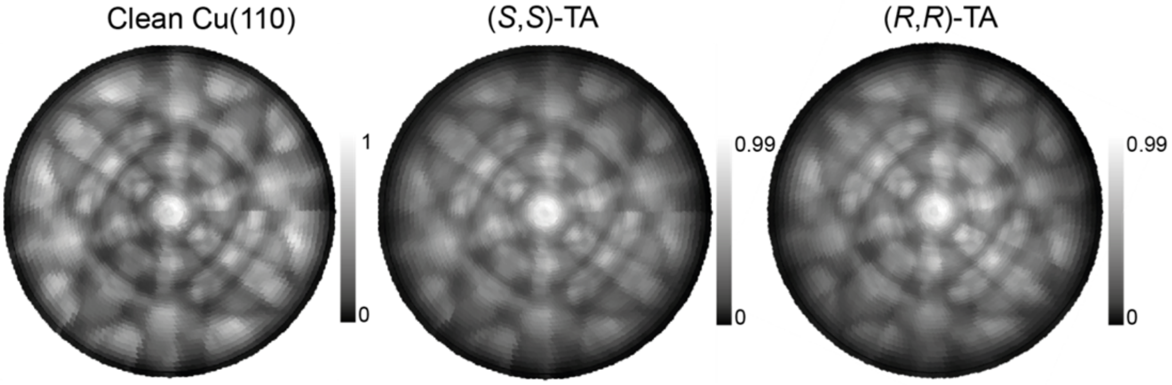

**Figure 9.4:** Stereographical representations collected at 932.8 eV (channel 1) of the clean Cu(110) surface, a layer of (*S*,*S*)-TA bitartrate and a layer of (*R*,*R*)-TA bitartrate on Cu(110). All images are background corrected by dividing the XPD data from channel 1 (932.8 eV) by the XPD data from channel 5 (930.3 eV) which serves as internal background. The intensity scales are normalised to the clean sample.

Background subtraction is performed by subtracting the normalised XPD data of the clean Cu(110) sample from the normalised sample data. As explained in the part on experimental considerations, information on the Cu atoms interacting with the oxygen atoms of TA can either be contained in the XPD data collected at 932.8 eV (channel 1) or in the XPD data collected at 934.1 eV (channel 4). Therefore, the normalisation of the sample data can either be done using channel 1 or channel 4 as primary source of information.

In Figure 9.5 data of (*R*,*R*)-TA and (*S*,*S*)-TA acquired using channel 1 and channel 4 are shown upon the subtraction of the substrate signal as previously described. The features in the stereographic representations are more pronounced when channel 4 as primary source of information is used. Therefore, both channels are used for further analysis.

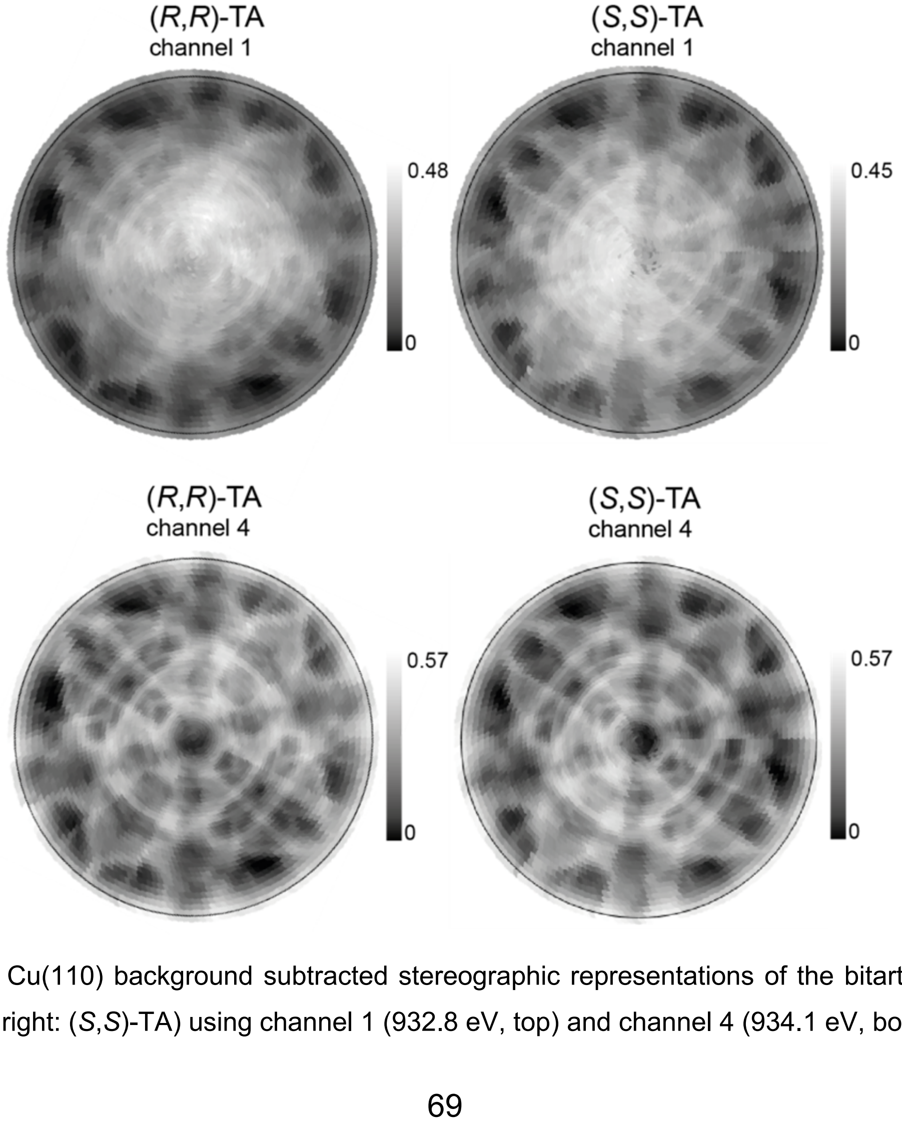

**Figure 9.5:** Cu(110) background subtracted stereographic representations of the bitartrate layers (left: (*R*,*R*)-TA; right: (*S*,*S*)-TA) using channel 1 (932.8 eV, top) and channel 4 (934.1 eV, bottom).

### 9.3.3 Discussion

The question is now if the features seen in the background corrected XPD images arise from the chiral imprinting of the TA enantiomers onto the first Cu(110) layer or if they arise from something else, e.g. slight rotation of the crystal in one experiment compared to the next one. A good way to check if the features in the images are real is to compare the subtraction images, *i.e.* the addition of the (*R*,*R*)-TA image to the reverse of the (*S*,*S*)-TA image. If this subtraction image is chiral, it is a good indication that the features are real. This subtraction image should then be compared to the subtraction image of the clean Cu(110) sample, *i.e.* the addition of the clean Cu(110) XPD to the inverse of that image which is rotated by 1° - 2°. The experimental setup allows for slight differences in alignment between the different experiments which include a relative rotation of the crystal by 1° - 2°. Figure 9.6 shows the sample subtraction image and the background subtraction image.

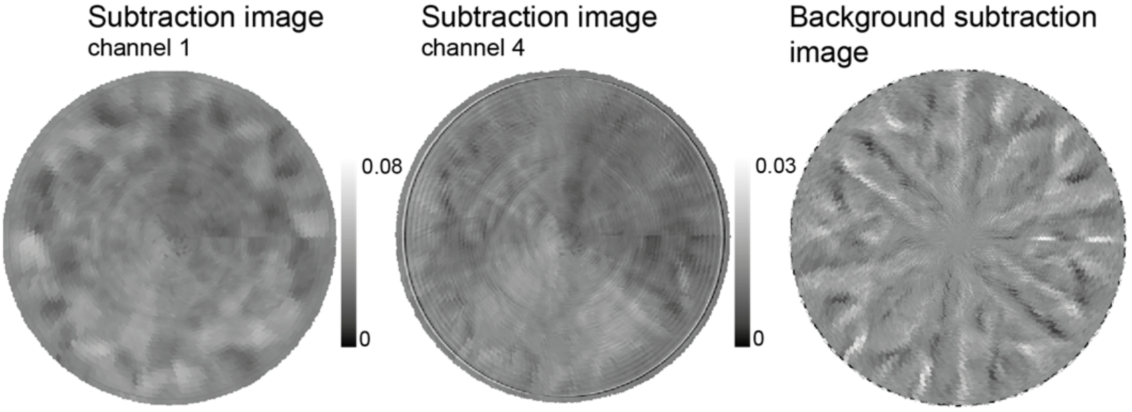

**Figure 9.6:** The subtraction images are shown: left the subtraction image of (*R*,*R*)-TA plus the inverse of (*S*,*S*)-TA using channel 1 and middle the same subtraction image using channel 4. Right: background subtraction image by the addition of the clean Cu(110) XPD to the inverse image of the same that is rotated by 2°. The contrast (right) is enhanced in favour of better visibility.

The features that are seen in the subtraction images are only up to 8% of the intensity of the clean Cu(110) surface in the case where channel 1 is used as information carrier and in the case of channel 4 the features are even less intense (3%). In the background subtraction image the contrast is enhanced for better visibility of the features that appear due to the rotation of one image by 2° compared to the other. These features look similar to the features seen in the subtraction images using channels 1 and 4. Therefore, if there is some signal arising from the chiral imprinting it might be hidden in the signal arising from the alignment mismatch.

## 9.4 Conclusion and Outlook

We used the X-ray photoelectron diffraction (XPD) method aiming to see whether the adsorption of the chiral enantiomers of tartaric acid imprints its chirality onto the first layer of a Cu(110) crystal. Without performing mathematical operations no differences between a clean Cu(110) sample and an adsorbed monolayer of TA on Cu(110) can be seen at 932.8 eV which is the energy of the Cu $2p_{3/2}$ peak. After background subtraction was performed, some features became visible, however their origin is not completely clear. After the analysis described in the discussion part, it seems that the features seen in the XPD experiments do not arise from the chiral imprinting of the TA enantiomers on the first Cu(110) layer. Their origin seems to be the mismatch in sample position, especially rotation of the crystal in the different experiments. The fact that the effect of chirally imprinted Cu is not observed in these experiments does not mean that it is not present. Additional experiments would have to be undertaken in order to tackle this effect.

There are several ways how these experiments can be improved. One option would be to create a thin layer of pseudo-Cu(110) on a Pd(110) crystal [125] and repeat the adsorption experiments of a monolayer of chiral bitartrate on this thin layer. This reduces the signal measured from the bulk Cu and makes seeing the shift of Cu due to the interaction with oxygen much easier. Though it has to be taken into account that the adsorption of TA on such a pseudo-Cu(110) surface might be different than on a normal Cu(110) surface due to lattice mismatch which results in different distances between the adsorbed TA molecules than on the normal Cu(110) surface.

Another reason for not seeing the shift in the Cu spectrum induced by the interaction of Cu with oxygen is that this shift is smaller than the binding energy difference of the channels in this experimental setup which is 1.3 eV. Therefore, the next experiments could be conducted with the main channel set on a higher binding energy until the oxygen induced shift is found. Another idea is to conduct XPD experiments over a range of a few eV until the effect of chiral imprinting is found.

This though means that the measurement time increases a lot. One XPD experiment ran for 8.5 h and if XPD experiments are performed every 0.5 eV in a range of 5 eV this leads to a measurement duration of nearly 4 days. In such an experiment beam damage becomes of increasing importance.

# 10 Summary and Outlook

This thesis concentrated on the interactions between metals and organic molecules on metal surfaces in UHV. The first investigated topic (chapter 6) is the metalation of the molecule pyrphyrin and the thereby induced scission of its cyano groups on Ag(111). We showed that upon annealing on Ag(111) pyrphyrin loses its two cyano groups as HCN. Upon annealing the nitrogen atoms of the inner macrocycle coordinate to an Ag atom of the metal surface and the hydrogen atoms of the iminic nitrogen atoms is released. This atomic hydrogen induces the loss of the cyano groups as HCN. The resulting molecule is a formal dicarbene. The decyanisation reaction can be suppressed by the metalation of pyrphyrin with Fe prior to the annealing step. The metalation of phyrphyrin with Fe happens at a lower temperature, therefore the hydrogen atoms leave the molecule before they can dissociate the cyano groups as HCN.

The topic of chapter 7 is the exchange of central metal ions in pyrphyrin. The metals of choice are Cu, Ni and Fe. Cu in the cavity of pyrphyrin (CuPyr) can be exchanged by Ni, giving NiPyr, and Ni can be exchanged by Fe (FePyr). This gives the following order of stability: FePyr is more stable than NiPyr which is more stable than CuPyr. These experiments show that some metal-organic complexes are preferred in formation over other metal-organic complexes. And special care must be taken when handling porphyrin-like molecules on a surface in UHV in the presence of weak, such as Cu or Zn, and strong binding metals, such as Ni or Fe, so that the metal of choice is ligated by the macrocycle.

Chapters 8 and 9 focus on the effect of the metal surface on the chemistry of the adsorbate and of the adsorbate on the metal surface. The metal surface geometry is found to have indeed an influence on the chemical and physical properties of the adsorbate. In chapter 8, tartaric acid (TA) was adsorbed on a Cu(111) surface and its adsorption and desorption properties are compared to the adsorption and desorption properties of TA on a Cu(110) surface. The results are that the geometry of the Cu surface does not have an effect on the adsorption properties of the TA diastereomers. The desorption properties on the other hand are different on Cu(110) than on Cu(111). On Cu(110) *rac*-TA the autocatalytic decomposition happens at lower temperature than the chiral TA and meso TA diastereomers. On Cu(111) on the other hand all the diastereomers of TA decompose autocatalytically at the same temperature. This indicates that the surface geometry enforces a difference in the assembly of the TA molecules which leads to the same surface explosion temperature for all three diastereomers on Cu(111).

Chapter 9 focusses on the assumed surface reconstruction enforced by TA adsorbed on a Cu(110) surface. X-ray photoelectron diffraction was chosen for the investigation of the reconstruction of the top layer of the Cu(110) crystal. This effect is expected to be small. The resulting stereographic representations show some features though the origin of these features is assumed to lie more in experimental alignment mismatch than in the real chiral imprinting effect. Therefore, more experiments should be undertaken in order to find the effect of the chiral imprinting of TA onto the Cu surface.

Some questions remain unanswered after this thesis. It would be interesting to experiment further on metalation of pyrphyrin, namely checking if other central metal atoms have an influence on the decyanisation process as well. Then, the formally dicarbene species is an interesting precursor for further coupling reactions and the rich carbine chemistry.

Concerning the metalation and atom exchange experiments it would be interesting to check other transition metals such as Ti, Cr or Mn to complete the list of stabilities. It would be also very interesting to check how well heavier transition metals such as Zr, Ru or Pd can be ligated into the cavity of the pyrphyrin molecule.

Concerning the tartaric acid (TA) on Cu(111) experiments it remains unclear why the amount of carboxylic acid is roughly half the expected amount of carboxylic acid. Further experiments need to be conducted in order to find an answer to that problem which appears to also exist in the literature but remains unaddressed [61].

The results concerning the chiral imprinting of TA onto the top layer of Cu atoms remain inconclusive as a lot of the background Cu signal had to be subtracted. Therefore, the outlook in this topic is to eliminate the signal from the bulk Cu. A good way to do this is to grow a thin layer of Cu (up to 5 monolayers of Cu) on a Pd(110) crystal giving a pseudo-Cu(110) surface. On this pseudo-Cu(110) surface chiral TA should be adsorbed as bitartrate and the X-ray photoelectron diffraction experiments should be repeated. Thus the XP signal from the bulk Cu is eliminated and the effect of the chiral imprinting of TA onto the top Cu layer should be visible. Though it has to be kept in mind, that a pseudo-Cu(110) surface has different strains which might lead to a different surface assembly of TA than on Cu(110). Furthermore, it would help the experiment tremendously if the XPD experiments were repeated on the binding energy to which the oxygen interacting Cu atoms from the top Cu layer are shifted. At this binding energy the effect of chiral imprinting should be seen the best.

# 11 References

[1] Kalinowski, J.; Cocchi, M.; Virgili, D.; Di Marco, P.; Fattori, V. Magnetic Field Effects on Emission and Current in Alq3-Based Electroluminescent Diodes. *Chem. Phys. Lett.* **2003**, *380*, 710–715, DOI:10.1016/j.cplett.2003.09.086.

[2] Wen, S.-W.; Lee, M.-T.; Chen, C. H. Recent Development of Blue Fluorescent OLED Materials and Devices. *J. Disp. Technol.* **2005**, *1*, 90–99, DOI:10.1109/JDT.2005.852802.

[3] Stewart, M.; Howell, R. S.; Pires, L.; Hatalis, M. K.; Howard, W.; Prache, O. Polysilicon VGA Active Matrix OLED Displays-Technology and Performance. In; IEEE, 1998; pp. 871–874.

[4] Vivo, P.; Jukola, J.; Ojala, M.; Chukharev, V.; Lemmetyinen, H. Influence of Alq3/Au Cathode on Stability and Efficiency of a Layered Organic Solar Cell in Air. *Sol. Energy Mater. Sol. Cells* **2008**, *92*, 1416–1420, DOI:10.1016/j.solmat.2008.06.002.

[5] Chamberlain, G. A. Organic Solar Cells: A Review. *Sol. Cells* **1983**, *8*, 47–83, DOI:10.1016/0379-6787(83)90039-X.

[6] Hoppe, H.; Sariciftci, N. S. Organic Solar Cells: An Overview. *J. Mater. Res.* **2004**, *19*, 1924–1945, DOI:10.1557/JMR.2004.0252.

[7] Ma, D.; Cai, Q.; Zhang, H. Mild Method for Ullmann Coupling Reaction of Amines and Aryl Halides. *Org. Lett.* **2003**, *5*, 2453–2455, DOI:10.1021/ol0346584.

[8] Beletskaya, I. P.; Cheprakov, A. V. Copper in Cross-Coupling Reactions. *Coord. Chem. Rev.* **2004**, *248*, 2337–2364, DOI:10.1016/j.ccr.2004.09.014.

[9] Hassan, J.; Sévignon, M.; Gozzi, C.; Schulz, E.; Lemaire, M. Aryl−Aryl Bond Formation One Century after the Discovery of the Ullmann Reaction. *Chem. Rev.* **2002**, *102*, 1359–1470, DOI:10.1021/cr000664r.

[10] Zhang, W.-J. A Review of the Electrochemical Performance of Alloy Anodes for Lithium-Ion Batteries. *J. Power Sources* **2011**, *196*, 13–24, DOI:10.1016/j.jpowsour.2010.07.020.

[11] Etacheri, V.; Haik, O.; Goffer, Y.; Roberts, G. A.; Stefan, I. C.; Fasching, R.; Aurbach, D. Effect of Fluoroethylene Carbonate (FEC) on the Performance and Surface Chemistry of Si-Nanowire Li-Ion Battery Anodes. *Langmuir* **2012**, *28*, 965–976, DOI:10.1021/la203712s.

[12] Kravchyk, K.; Protesescu, L.; Bodnarchuk, M. I.; Krumeich, F.; Yarema, M.; Walter, M.; Guntlin, C.; Kovalenko, M. V. Monodisperse and Inorganically Capped Sn and Sn/SnO2 Nanocrystals for High-Performance Li-Ion Battery Anodes. *J. Am. Chem. Soc.* **2013**, *135*, 4199–4202, DOI:10.1021/ja312604r.

[13] Liu, N.; Wu, H.; McDowell, M. T.; Yao, Y.; Wang, C.; Cui, Y. A Yolk-Shell Design for Stabilized and Scalable Li-Ion Battery Alloy Anodes. *Nano Lett.* **2012**, *12*, 3315–3321, DOI:10.1021/nl3014814.

[14] Cai, J.; Ruffieux, P.; Jaafar, R.; Bieri, M.; Braun, T.; Blankenburg, S.; Muoth, M.; Seitsonen, A. P.; Saleh, M.; Feng, X.; *et al.* Atomically Precise Bottom-up Fabrication of Graphene Nanoribbons. *Nature* **2010**, *466*, 470–473, DOI:10.1038/nature09211.

[15] Talirz, L.; Söde, H.; Cai, J.; Ruffieux, P.; Blankenburg, S.; Jafaar, R.; Berger, R.; Feng, X.; Müllen, K.; Passerone, D.; *et al.* Termini of Bottom-Up Fabricated Graphene Nanoribbons. *J. Am. Chem. Soc.* **2013**, *135*, 2060–2063, DOI:10.1021/ja311099k.

[16] Orzeł, Ł.; van Eldik, R.; Fiedor, L.; Stochel, G. Mechanistic Information on Cu $^{II}$ Metalation and Transmetalation of Chlorophylls. *Eur. J. Inorg. Chem.* **2009**, *2009*, 2393–2406, DOI:10.1002/ejic.200800662.

[17] Lingenfelder, M. A.; Spillmann, H.; Dmitriev, A.; Stepanow, S.; Lin, N.; Barth, J. V.; Kern, K. Towards Surface-Supported Supramolecular Architectures: Tailored Coordi-

nation Assembly of 1,4-Benzenedicarboxylate and Fe on Cu(100). *Chem. - Eur. J.* **2004**, *10*, 1913–1919, DOI:10.1002/chem.200305589.

[18] Stepanow, S.; Lin, N.; Payer, D.; Schlickum, U.; Klappenberger, F.; Zoppellaro, G.; Ruben, M.; Brune, H.; Barth, J. V.; Kern, K. Surface-Assisted Assembly of 2D Metal–Organic Networks That Exhibit Unusual Threefold Coordination Symmetry. *Angew. Chem.* **2007**, *119*, 724–727, DOI:10.1002/ange.200603644.

[19] Stepanow, S.; Strunskus, T.; Lingenfelder, M.; Dmitriev, A.; Spillmann, H.; Lin, N.; Barth, J. V.; Wöll, C.; Kern, K. Deprotonation-Driven Phase Transformations in Terephthalic Acid Self-Assembly on Cu(100). *J. Phys. Chem. B* **2004**, *108*, 19392–19397, DOI:10.1021/jp046766t.

[20] Tait, S. L.; Langner, A.; Lin, N.; Chandrasekar, R.; Fuhr, O.; Ruben, M.; Kern, K. Assembling Isostructural Metal-Organic Coordination Architectures on Cu(100), Ag(100) and Ag(111) Substrates. *ChemPhysChem* **2008**, *9*, 2495–2499, DOI:10.1002/cphc.200800575.

[21] Hipps, K. W.; Xing Lu, X. D. W.; Mazur, U. Metal D-Orbital Occupation-Dependent Images in the Scanning Tunneling Microscopy of Metal Phthalocyanines. *J Phys Chem* **1996**, *100*, 11207–11210, DOI:10.1021/jp960422o.

[22] Lu, X.; Hipps, K. W. Scanning Tunneling Microscopy of Metal Phthalocyanines: D6 and D8 Cases. *J. Phys. Chem. B* **1997**, *101*, 5391–5396, DOI:10.1021/jp9707448.

[23] Gottfried, J. M.; Flechtner, K.; Kretschmann, A.; Lukasczyk, T.; Steinrück, H.-P. Direct Synthesis of a Metalloporphyrin Complex on a Surface. *J. Am. Chem. Soc.* **2006**, *128*, 5644–5645, DOI:10.1021/ja0610333.

[24] Buchner, F.; Schwald, V.; Comanici, K.; Steinrück, H.-P.; Marbach, H. Microscopic Evidence of the Metalation of a Free-Base Porphyrin Monolayer with Iron. *ChemPhysChem* **2007**, *8*, 241–243, DOI:10.1002/cphc.200600698.

[25] Bai, Y.; Buchner, F.; Wendahl, M. T.; Kellner, I.; Bayer, A.; Steinrück, H.-P.; Marbach, H.; Gottfried, J. M. Direct Metalation of a Phthalocyanine Monolayer on Ag(111) with Coadsorbed Iron Atoms. *J. Phys. Chem. C* **2008**, *112*, 6087–6092, DOI:10.1021/jp711122w.

[26] Gottfried, M.; Marbach, H. Surface-Confined Coordination Chemistry with Porphyrins and Phthalocyanines: Aspects of Formation, Electronic Structure, and Reactivity. *Z. Für Phys. Chem.* **2009**, *223*, 53–74, DOI:10.1524/zpch.2009.6024.

[27] Diller, K.; Papageorgiou, A. C.; Klappenberger, F.; Allegretti, F.; Barth, J. V.; Auwärter, W. In Vacuo Interfacial Tetrapyrrole Metallation. *Chem Soc Rev* **2016**, *45*, 1629–1656, DOI:10.1039/C5CS00207A.

[28] Gottfried, J. M. Surface Chemistry of Porphyrins and Phthalocyanines. *Surf. Sci. Rep.* **2015**, *70*, 259–379, DOI:10.1016/j.surfrep.2015.04.001.

[29] Smykalla, L.; Shukrynau, P.; Zahn, D. R. T.; Hietschold, M. Self-Metalation of Phthalocyanine Molecules with Silver Surface Atoms by Adsorption on Ag(110). *J. Phys. Chem. C* **2015**, *119*, 17228–17234, DOI:10.1021/acs.jpcc.5b04977.

[30] Sperl, A.; Kröger, J.; Berndt, R. Controlled Metalation of a Single Adsorbed Phthalocyanine. *Angew. Chem. Int. Ed.* **2011**, *50*, 5294–5297, DOI:10.1002/anie.201100950.

[31] Shen, K.; Narsu, B.; Ji, G.; Sun, H.; Hu, J.; Liang, Z.; Gao, X.; Li, H.; Li, Z.; Song, B.; *et al.* On-Surface Manipulation of Atom Substitution between Cobalt Phthalocyanine and the Cu(111) Substrate. *RSC Adv* **2017**, *7*, 13827–13835, DOI:10.1039/C7RA00636E.

[32] Ogawa, S.; Narushima, R.; Arai, Y. Aza Macrocylce That Selectively Binds Lithium Ion with Color Change. *J Am Chem Soc* **1984**, *106*, 5760–5762, DOI:10.1021/ja00331a074.

[33] Gurdal, Y.; Luber, S.; Hutter, J.; Iannuzzi, M. Non-Innocent Adsorption of Co-Pyrphyrin on Rutile(110). *Phys Chem Chem Phys* **2015**, *17*, 22846–22854, DOI:10.1039/C5CP02767E.

[34] Gurdal, Y.; Hutter, J.; Iannuzzi, M. Insight into (Co)Pyrphyrin Adsorption on Au(111): Effects of Herringbone Reconstruction and Dynamics of Metalation. *J. Phys. Chem. C* **2017**, *121*, 11416–11427, DOI:10.1021/acs.jpcc.7b02069.

[35] Li, J.; Wäckerlin, C.; Schnidrig, S.; Joliat, E.; Alberto, R.; Ernst, K.-H. On-Surface Metalation and 2D Self-Assembly of Pyrphyrin Molecules Into Metal-Coordinated Networks on Cu(111). *Helv. Chim. Acta* **2017**, *100*, e1600278, DOI:10.1002/hlca.201600278.

[36] Mette, G.; Sutter, D.; Gurdal, Y.; Schnidrig, S.; Probst, B.; Iannuzzi, M.; Hutter, J.; Alberto, R.; Osterwalder, J. From Porphyrins to Pyrphyrins: Adsorption Study and Metalation of a Molecular Catalyst on Au(111). *Nanoscale* **2016**, *8*, 7958–7968, DOI:10.1039/C5NR08953K.

[37] Boucher, L. J.; Katz, J. J. The Infrared Spectra of Metalloporphyrins (4000-160 Cm-1)1. *J Am Chem Soc* **1967**, *89*, 1340–1345, DOI:10.1021/ja00982a011.

[38] Grant, C.; Hambright, P. Kinetics of Electrophyilic Substitution Reactions Involving Metal Ions in Metalloporphyrins. *J Am Chem Soc* **1969**, *91*, 4195–4198, DOI:10.1021/ja01043a030.

[39] Auwärter, W.; Weber-Bargioni, A.; Brink, S.; Riemann, A.; Schiffrin, A.; Ruben, M.; Barth, J. V. Controlled Metalation of Self-Assembled Porphyrin Nanoarrays in Two Dimensions. *ChemPhysChem* **2007**, *8*, 250–254, DOI:10.1002/cphc.200600675.

[40] Buchner, F.; Flechtner, K.; Bai, Y.; Zillner, E.; Kellner, I.; Steinrück, H.-P.; Marbach, H.; Gottfried, J. M. Coordination of Iron Atoms by Tetraphenylporphyrin Monolayers and Multilayers on Ag(111) and Formation of Iron-Tetraphenylporphyrin. *J. Phys. Chem. C* **2008**, *112*, 15458–15465, DOI:10.1021/jp8052955.

[41] Chen, M.; Feng, X.; Zhang, L.; Ju, H.; Xu, Q.; Zhu, J.; Gottfried, J. M.; Ibrahim, K.; Qian, H.; Wang, J. Direct Synthesis of Nickel(II) Tetraphenylporphyrin and Its Interaction with a Au(111) Surface: A Comprehensive Study. *J. Phys. Chem. C* **2010**, *114*, 9908–9916, DOI:10.1021/jp102031m.

[42] Diller, K.; Klappenberger, F.; Marschall, M.; Hermann, K.; Nefedov, A.; Wöll, C.; Barth, J. V. Self-Metalation of 2H-Tetraphenylporphyrin on Cu(111): An x-Ray Spectroscopy Study. *J. Chem. Phys.* **2012**, *136*, 014705, DOI:10.1063/1.3674165.

[43] Auwärter, W.; Écija, D.; Klappenberger, F.; Barth, J. V. Porphyrins at Interfaces. *Nat. Chem.* **2015**, *7*, 105–120, DOI:10.1038/nchem.2159.

[44] Franke, M.; Marchini, F.; Jux, N.; Steinrück, H.-P.; Lytken, O.; Williams, F. J. Zinc Porphyrin Metal-Center Exchange at the Solid-Liquid Interface. *Chem. - Eur. J.* **2016**, *22*, 8520–8524, DOI:10.1002/chem.201600634.

[45] Lavallee, D. K. Kinetics and Mechanisms of Metalloporphyrin Reactions. *Coord. Chem. Rev.* **1984**, *61*, 55–96, DOI:10.1016/0010-8545(85)80002-3.

[46] Zhou, Z.; Shen, M.; Cao, C.; Liu, Q.; Yan, Z. Opposing Influences of Ruffling and Doming Deformation on the 4-N Cavity Size of Porphyrin Macrocycles: The Role of Heme Deformations Revealed. *Chem. - Eur. J.* **2012**, *18*, 7675–7679, DOI:10.1002/chem.201200722.

[47] Doyle, C. M.; Cunniffe, J. P.; Krasnikov, S. A.; Preobrajenski, A. B.; Li, Z.; Sergeeva, N. N.; Senge, M. O.; Cafolla, A. A. Ni-Cu Ion Exchange Observed for Ni(II)-Porphyrins on Cu(111). *Chem. Commun.* **2014**, *50*, 3447, DOI:10.1039/c3cc48913b.

[48] Ortega Lorenzo, M.; Haq, S.; Bertrams, T.; Murray, P.; Raval, R.; Baddeley, C. J. Creating Chiral Surfaces for Enantioselective Heterogeneous Catalysis: R,R-Tartaric Acid on Cu(110). *J. Phys. Chem. B* **1999**, *103*, 10661–10669, DOI:10.1021/jp992188i.

[49] Ortega Lorenzo, M.; Baddeley, C. J.; Muryn, C.; Raval, R. Extended Surface Chirality from Supramolecular Assemblies of Adsorbed Chiralmolecules. *Nature* **2000**, *404*, 376–379, DOI:10.1038/35006031.

[50] Ortega Lorenzo, M.; Humblot, V.; Murray, P.; Baddeley, C. J.; Haq, S.; Raval, R. Chemical Transformations, Molecular Transport, and Kinetic Barriers in Creating the

Chiral Phase of (R,R)-Tartaric Acid on Cu(110). *J. Catal.* **2002**, *205*, 123–134, DOI:10.1006/jcat.2001.3422.

[51] Darling, G. R.; Forster, M.; Lin, C.; Liu, N.; Raval, R.; Hodgson, A. Chiral Segregation Driven by a Dynamical Response of the Adsorption Footprint to the Local Adsorption Environment: Bitartrate on Cu(110). *Phys Chem Chem Phys* **2017**, *19*, 7617–7623, DOI:10.1039/C7CP00622E.

[52] Barbosa, L. A. M. M.; Sautet, P. Stability of Chiral Domains Produced by Adsorption of Tartaric Acid Isomers on the Cu(110) Surface: A Periodic Density Functional Theory Study. *J. Am. Chem. Soc.* **2001**, *123*, 6639–6648, DOI:10.1021/ja004336k.

[53] Hermse, C. G. M.; van Bavel, A. P.; Jansen, A. P. J.; Barbosa, L. A. M. M.; Sautet, P.; van Santen, R. A. Formation of Chiral Domains for Tartaric Acid on Cu(110): A Combined DFT and Kinetic Monte Carlo Study. *J. Phys. Chem. B* **2004**, *108*, 11035–11043, DOI:10.1021/jp0490195.

[54] Humblot, V.; Haq, S.; Muryn, C.; Hofer, W. A.; Raval, R. From Local Adsorption Stresses to Chiral Surfaces: (R,R)-Tartaric Acid on Ni(110). *J. Am. Chem. Soc.* **2002**, *124*, 503–510, DOI:10.1021/ja012021e.

[55] Hofer, W. A.; Humblot, V.; Raval, R. Conveying Chirality onto the Electronic Structure of Achiral Metals: (R,R)-Tartaric Acid on Nickel. *Surf. Sci.* **2004**, *554*, 141–149, DOI:10.1016/j.susc.2003.12.060.

[56] Humblot, V.; Haq, S.; Muryn, C.; Raval, R. (R,R)-Tartaric Acid on Ni(110): The Dynamic Nature of Chiral Adsorption Motifs. *J. Catal.* **2004**, *228*, 130–140, DOI:10.1016/j.jcat.2004.08.023.

[57] Romer, S.; Behzadi, B.; Fasel, R.; Ernst, K.-H. Homochiral Conglomerates and Racemic Crystals in Two Dimensions: Tartaric Acid on Cu(110). *Chem. - Eur. J.* **2005**, *11*, 4149–4154, DOI:10.1002/chem.200400962.

[58] Behzadi, B.; Romer, S.; Fasel, R.; Ernst, K.-H. Chiral Recognition in Surface Explosion. *J. Am. Chem. Soc.* **2004**, *126*, 9176–9177, DOI:10.1021/ja048206d.

[59] Parschau, M.; Behzadi, B.; Romer, S.; Ernst, K.-H. Stereoisomeric Influence on 2D Lattice Structure: Achiralmeso-Tartaric Acidversus Chiral Tartaric Acid. *Surf. Interface Anal.* **2006**, *38*, 1607–1610, DOI:10.1002/sia.2426.

[60] Parschau, M.; Kampen, T.; Ernst, K.-H. Homochirality in Monolayers of Achiral Meso Tartaric Acid. *Chem. Phys. Lett.* **2005**, *407*, 433–437, DOI:10.1016/j.cplett.2005.03.117.

[61] Baldanza, S.; Ardini, J.; Giglia, A.; Held, G. Stereochemistry and Thermal Stability of Tartaric Acid on the Intrinsically Chiral Cu{531} Surface. *Surf. Sci.* **2016**, *643*, 108–116, DOI:10.1016/j.susc.2015.08.021.

[62] Mhatre, B. S.; Pushkarev, V.; Holsclaw, B.; Lawton, T. J.; Sykes, E. C. H.; Gellman, A. J. A Window on Surface Explosions: Tartaric Acid on Cu(110). *J. Phys. Chem. C* **2013**, *117*, 7577–7588, DOI:10.1021/jp3119378.

[63] Makeev, A. G.; Nieuwenhuys, B. E. Mathematical Modeling of the NO+H2/Pt(100) Reaction: “Surface Explosion,” Kinetic Oscillations, and Chaos. *J. Chem. Phys.* **1998**, *108*, 3740–3749, DOI:10.1063/1.475767.

[64] Mccarty, J. Decomposition of Formic Acid on Ni(110) I. Flash Decomposition from the Clean Surface and Flash Desorption of Reaction Products. *J. Catal.* **1973**, *30*, 235–249, DOI:10.1016/0021-9517(73)90070-5.

[65] Falconer, J.; Mccarty, J.; Madix, R. J. The Explosive Decomposition of Formic Acid on Clean Ni(110). *Jpn. J. Appl. Phys.* **1974**, *13*, DOI:10.7567/JJAPS.2S2.525.

[66] Falconer, J. L.; Madix, R. J. The Kinetics and Mechanism of the Autocatalytic Decomposition of HCOOH on Clean Ni(110). *Surf. Sci.* **1974**, *46*, 473–504, DOI:10.1016/0039-6028(74)90321-5.

[67] Therrien, A. J.; Lawton, T. J.; Mernoff, B.; Lucci, F. R.; Pushkarev, V. V.; Gellman, A. J.; Sykes, E. C. H. Chiral Nanoscale Pores Created during the Surface Explosion of Tartaric Acid on Cu(111). *Chem Commun* **2016**, *52*, 14282–14285, DOI:10.1039/C6CC05820E.

[68] Yan, H.-J.; Wang, D.; Han, M.-J.; Wan, L.-J.; Bai, C.-L. Adsorption and Coordination of Tartaric Acid Enantiomers on Cu(111) in Aqueous Solution. *Langmuir* **2004**, *20*, 7360–7364, DOI:10.1021/la035283y.

[69] Baird, R. J.; Wagner, L. F.; Fadley, C. S. Angular Dependence of X-Ray-Photoemitted Valence-Electron Spectra from Single-Crystal Gold. *Phys. Rev. Lett.* **1976**, *37*, 111–114, DOI:10.1103/PhysRevLett.37.111.

[70] Siegbahn, K.; Gelius, U.; Siegbahn, H.; Olson, E. Angular Distribution of Electrons in ESCA Spectra from a Single Crystal. *Phys. Scr.* **1970**, *1*, 272–276, DOI:10.1088/0031-8949/1/5-6/017.

[71] McFeely, F. R.; Stöhr, J.; Apai, G.; Wehner, P. S.; Shirley, D. A. D-Orbital-Directed Photoemission from Silver and Gold. *Phys. Rev. B* **1976**, *14*, 3273–3276, DOI:10.1103/PhysRevB.14.3273.

[72] Muntwiler, M.; Auwärter, W.; Baumberger, F.; Hoesch, M.; Greber, T.; Osterwalder, J. Determining Adsorbate Structures from Substrate Emission X-Ray Photoelectron Diffraction. *Surf. Sci.* **2001**, *472*, 125–132, DOI:10.1016/S0039-6028(00)00928-6.

[73] Fasel, R.; Aebi, P.; Agostino, R. G.; Naumovic, D.; Osterwalder, J.; Santaniello, A.; Schlapbach, L. Orientation of Adsorbed C60 Molecules Determined via X-Ray Photoelectron Diffraction. *Phys. Rev. Lett.* **1996**, *76*, 4733–4736, DOI:10.1103/PhysRevLett.76.4733.

[74] Kim, Y. J.; Westphal, C.; Ynzunza, R. X.; Wang, Z.; Galloway, H. C.; Salmeron, M.; Van Hove, M. A.; Fadley, C. S. The Growth of Iron Oxide Films on Pt(111): A Combined XPD, STM, and LEED Study. *Surf. Sci.* **1998**, *416*, 68–111, DOI:10.1016/S0039-6028(98)00506-8.

[75] Fasel, R.; Wider, J.; Quitmann, C.; Ernst, K.-H.; Greber, T. Determination of the Absolute Chirality of Adsorbed Molecules. *Angew. Chem. Int. Ed.* **2004**, *43*, 2853–2856, DOI:10.1002/anie.200353311.

[76] Vickerman, J. C.; Gilmore, I. S. *Surface Analysis - The Principal Techniques*; 2.; John Wiley & Sons Ltd: West Sussex, United Kingdom, 2009.

[77] Oura, K.; Lifshits, V. G.; Saranin, A. A.; Zotov, A. V.; Katayama, M. *Surface Science - An Introduction*; Springer-Verlag: Berlin/Heidelberg, 2004.

[78] Osterwalder, J. Structural Effects in XPS and AES: Diffraction. In *Surface Analysis by Auger and X-ray Photoelectron Spectroscopy*; IM Publications and SurfaceSpectra Limited: Physik-Institut, Universität Zürich, 2003; pp. 557–586.

[79] Kuznetsov, M. V.; Ogorodnikov, I. I.; Vorokh, A. S. X-Ray Photoelectron Diffraction and Photoelectron Holography as Methods for Investigating the Local Atomic Structure of the Surface of Solids. *Russ. Chem. Rev.* **2014**, *83*, 13–37, DOI:10.1070/RC2014v083n01ABEH004400.

[80] Winkelmann, A.; Schröter, B.; Richter, W. Electron Diffraction Methods for the Analysis of Silicon Carbide Surfaces and the Controlled Growth of Polytype Heterostructures. *J. Phys. Condens. Matter* **2004**, *16*, S1555–S1578, DOI:10.1088/0953-8984/16/17/008.

[81] Horcas, I.; Fernández, R.; Gómez-Rodríguez, J. M.; Colchero, J.; Gómez-Herrero, J.; Baro, A. M. WSXM: A Software for Scanning Probe Microscopy and a Tool for Nanotechnology. *Rev. Sci. Instrum.* **2007**, *78*, 013705, DOI:10.1063/1.2432410.

[82] Rieger, A.; Schnidrig, S.; Probst, B.; Ernst, K.-H.; Wäckerlin, C. Identification of On-Surface Reaction Mechanism by Targeted Metalation. *J. Phys. Chem. C* **2017**, *121*, 27521–27527, DOI:10.1021/acs.jpcc.7b10019.

[83] Lukasczyk, T.; Flechtner, K.; Merte, L. R.; Jux, N.; Maier, F.; Gottfried, J. M.; Steinrück, H.-P. Interaction of Cobalt(II) Tetraarylporphyrins with a Ag(111) Surface Studied with Photoelectron Spectroscopy. *J. Phys. Chem. C* **2007**, *111*, 3090–3098, DOI:10.1021/jp0652345.

[84] Wurster, B.; Grumelli, D.; Hötger, D.; Gutzler, R.; Kern, K. Driving the Oxygen Evolution Reaction by Nonlinear Cooperativity in Bimetallic Coordination Catalysts. *J. Am. Chem. Soc.* **2016**, *138*, 3623–3626, DOI:10.1021/jacs.5b10484.

[85] Wäckerlin, C.; Chylarecka, D.; Kleibert, A.; Müller, K.; Iacovita, C.; Nolting, F.; Jung, T. A.; Ballav, N. Controlling Spins in Adsorbed Molecules by a Chemical Switch. *Nat. Commun.* **2010**, *1*, 1–7, DOI:10.1038/ncomms1057.

[86] Zhou, X.-L.; White, J. M.; Koel, B. E. Chemisorption of Atomic Hydrogen on Clean and Cl-Covered Ag(111). *Surf. Sci.* **1989**, 201–210, DOI:10.1016/0039-6028(89)90627-4.

[87] Hayashi, H.; Yamaguchi, J.; Jippo, H.; Hayashi, R.; Aratani, N.; Ohfuchi, M.; Sato, S.; Yamada, H. Experimental and Theoretical Investigations of Surface-Assisted Graphene Nanoribbon Synthesis Featuring Carbon–Fluorine Bond Cleavage. *ACS Nano* **2017**, *11*, 6204–6210, DOI:10.1021/acsnano.7b02316.

[88] Röckert, M.; Franke, M.; Tariq, Q.; Lungerich, D.; Jux, N.; Stark, M.; Kaftan, A.; Ditze, S.; Marbach, H.; Laurin, M.; *et al.* Insights in Reaction Mechanistics: Isotopic Exchange during the Metalation of Deuterated Tetraphenyl-21,23D-Porphyrin on Cu(111). *J. Phys. Chem. C* **2014**, *118*, 26729–26736, DOI:10.1021/jp507303h.

[89] Bronner, C.; Björk, J.; Tegeder, P. Tracking and Removing Br during the On-Surface Synthesis of a Graphene Nanoribbon. *J. Phys. Chem. C* **2015**, *119*, 486–493, DOI:10.1021/jp5106218.

[90] Graf, M.; Mette, G.; Leuenberger, D.; Gurdal, Y.; Iannuzzi, M.; Zabka, W.-D.; Schnidrig, S.; Probst, B.; Hutter, J.; Alberto, R.; *et al.* The Impact of Metalation on Adsorption Geometry, Electronic Level Alignment and UV-Stability of Organic Macrocycles on $TiO_2$ (110). *Nanoscale* **2017**, *9*, 8756–8763, DOI:10.1039/C7NR02317K.

[91] Joliat, E.; Schnidrig, S.; Probst, B.; Bachmann, C.; Spingler, B.; Baldridge, K. K.; von Rohr, F.; Schilling, A.; Alberto, R. Cobalt Complexes of Tetradentate, Bipyridine-Based Macrocycles: Their Structures, Properties and Photocatalytic Proton Reduction. *Dalton Trans* **2016**, *45*, 1737–1745, DOI:10.1039/C5DT04426J.

[92] Wiengarten, A.; Seufert, K.; Auwärter, W.; Ecija, D.; Diller, K.; Allegretti, F.; Bischoff, F.; Fischer, S.; Duncan, D. A.; Papageorgiou, A. C.; *et al.* Surface-Assisted Dehydrogenative Homocoupling of Porphine Molecules. *J. Am. Chem. Soc.* **2014**, *136*, 9346–9354, DOI:10.1021/ja501680n.

[93] He, Y.; Garnica, M.; Bischoff, F.; Ducke, J.; Bocquet, M.-L.; Batzill, M.; Auwärter, W.; Barth, J. V. Fusing Tetrapyrroles to Graphene Edges by Surface-Assisted Covalent Coupling. *Nat. Chem.* **2016**, DOI:10.1038/nchem.2600.

[94] Zhang, Y.-Q.; Kepčija, N.; Kleinschrodt, M.; Diller, K.; Fischer, S.; Papageorgiou, A. C.; Allegretti, F.; Björk, J.; Klyatskaya, S.; Klappenberger, F.; *et al.* Homo-Coupling of Terminal Alkynes on a Noble Metal Surface. *Nat. Commun.* **2012**, *3*, 1286, DOI:10.1038/ncomms2291.

[95] Shen, K.; Narsu, B.; Ji, G.; Sun, H.; Hu, J.; Liang, Z.; Gao, X.; Li, H.; Li, Z.; Song, B.; *et al.* On-Surface Manipulation of Atom Substitution between Cobalt Phthalocyanine and the Cu(111) Substrate. *RSC Adv* **2017**, *7*, 13827–13835, DOI:10.1039/C7RA00636E.

[96] Lawton, E. A. The Thermal Stability of Copper Phthalocyanine. *J Phys Chem* **1958**, *62*, 384–384, DOI:10.1021/j150561a051.

[97] Schreiver, I.; Hutzler, C.; Laux, P.; Berlien, H.-P.; Luch, A. Formation of Highly Toxic Hydrogen Cyanide upon Ruby Laser Irradiation of the Tattoo Pigment Phthalocyanine Blue. *Sci. Rep.* **2015**, *5*, DOI:10.1038/srep12915.

[98] Ciftlikli, E. Z.; Lee, E. Y. M.; Lallo, J.; Rangan, S.; Senanayake, S. D.; Hinch, B. J. Implementation of New TPD Analysis Techniques in the Evaluation of Second Order Desorption Kinetics of Cyanogen from Cu(001). *Langmuir* **2010**, *26*, 18742–18749, DOI:10.1021/la102304m.

[99] Rieger, A.; Schnidrig, S.; Probst, B.; Ernst, K.-H.; Wäckerlin, C. Ranking the Stability of Transition Metal Complexes by On-Surface Atom Exchange. *J. Phys. Chem. Lett.* **2017**, *8*, 6193–6198, DOI:10.1021/acs.jpclett.7b02834.

[100] Liao, M.-S.; Scheiner, S. Electronic Structure and Bonding in Metal Porphyrins, Metal=Fe, Co, Ni, Cu, Zn. *J. Chem. Phys.* **2002**, *117*, 205–219, DOI:10.1063/1.1480872.

[101] Feixas, F.; Solà, M.; Swart, M. Chemical Bonding and Aromaticity in Metalloporphyrins. *Can. J. Chem.* **2009**, *87*, 1063–1073, DOI:10.1139/V09-037.

[102] Shubina, T. E.; Marbach, H.; Flechtner, K.; Kretschmann, A.; Jux, N.; Buchner, F.; Steinrück, H.-P.; Clark, T.; Gottfried, J. M. Principle and Mechanism of Direct Porphyrin Metalation: Joint Experimental and Theoretical Investigation. *J. Am. Chem. Soc.* **2007**, *129*, 9476–9483, DOI:10.1021/ja072360t.

[103] Madura, P.; Scheidt, W. R. Stereochemistry of Low-Spin Cobalt Porphyrins 8. α,β,γ,δ- Tetraphenylporphinatocobalt(II). *Inorg Chem* **1976**, *15*, 3182–3184, DOI:10.1021/ic50166a056.

[104] Doyle, Catherine. An Investigation of the Structural and Electronic Properties of Covalently Bonded Molecular Networks on Metal Surfaces Formed Through Debromination Reactions. Chemistry, Dublin City University: Dublin.

[105] Dong, L.; Liu, P. N.; Lin, N. Surface-Activated Coupling Reactions Confined on a Surface. *Acc. Chem. Res.* **2015**, *48*, 2765–2774, DOI:10.1021/acs.accounts.5b00160.

[106] Rumble, J. R.; Lide, D. R.; Bruno, T. J. CRC Handbook of Chemistry and Physics: A Ready-Reference Book of Chemical and Physical Data. *Product. Press* **2017**.

[107] Nowakowski, J.; Wäckerlin, C.; Girovsky, J.; Siewert, D.; Jung, T. A.; Ballav, N. Porphyrin Metalation Providing an Example of a Redox Reaction Facilitated by a Surface Reconstruction. *Chem. Commun.* **2013**, *49*, 2347, DOI:10.1039/c3cc39134e.

[108] Wäckerlin, A.; Fatayer, S.; Nijs, T.; Nowakowska, S.; Mousavi, S. F.; Popova, O.; Ahsan, A.; Jung, T. A.; Wäckerlin, C. Molecular Chessboard Assemblies Sorted by Site-Specific Interactions of Out-of-Plane d-Orbitals with a Semimetal Template. *Nano Lett.* **2017**, *17*, 1956–1962, DOI:10.1021/acs.nanolett.6b05344.

[109] Hipps, K. W. Scanning Tunneling Spectroscopy (STS). In *Handbook of Applied Solid State Spectroscopy*; Vij, D. R., Ed.; Springer-Verlag, 2006.

[110] Doyle, C. M.; Krasnikov, S. A.; Sergeeva, N. N.; Preobrajenski, A. B.; Vinogradov, N. A.; Sergeeva, Y. N.; Senge, M. O.; Cafolla, A. A. Evidence for the Formation of an Intermediate Complex in the Direct Metalation of Tetra(4-Bromophenyl)-Porphyrin on the Cu(111) Surface. *Chem. Commun.* **2011**, *47*, 12134, DOI:10.1039/c1cc15241f.

[111] Marbach, H. Surface-Mediated in-Situ Metalation of Porphyrins at the Solid–Vacuum Interface. *Acc. Chem. Res.* **2015**, *48*, 2649–2658, DOI:10.1021/acs.accounts.5b00243.

[112] Vijayaraghavan, S.; Auwärter, W.; Ecija, D.; Seufert, K.; Rusponi, S.; Houwaart, T.; Sautet, P.; Bocquet, M.-L.; Thakur, P.; Stepanow, S.; *et al.* Restoring the Co Magnetic Moments at Interfacial Co-Porphyrin Arrays by Site-Selective Uptake of Iron. *ACS Nano* **2015**, *9*, 3605–3616, DOI:10.1021/nn507346x.

[113] Rieger, A.; Sax, C.; Bauert, T.; Wäckerlin, C.; Ernst, K.-H. Chiral Molecules Adsorbed on a Solid Surface: Tartaric Acid Diastereomers and Their Surface Explosion on Cu(111). *Chirality* **2018**, DOI:10.1002/chir.22819.

[114] Lawton, T. J.; Pushkarev, V.; Wei, D.; Lucci, F. R.; Sholl, D. S.; Gellman, A. J.; Sykes, E. C. H. Long Range Chiral Imprinting of Cu(110) by Tartaric Acid. *J. Phys. Chem. C* **2013**, *117*, 22290–22297, DOI:10.1021/jp402015r.

[115] Parschau, M.; Romer, S.; Ernst, K.-H. Induction of Homochirality in Achiral Enantiomorphous Monolayers. *J. Am. Chem. Soc.* **2004**, *126*, 15398–15399, DOI:10.1021/ja044136z.

[116] Gellman, A. J.; Huang, Y.; Feng, X.; Pushkarev, V. V.; Holsclaw, B.; Mhatre, B. S. Superenantioselective Chiral Surface Explosions. *J. Am. Chem. Soc.* **2013**, *135*, 19208–19214, DOI:10.1021/ja408659v.

[117] Lemieux, R. P. Chirality Transfer in Ferroelectric Liquid Crystals. *Acc. Chem. Res.* **2001**, *34*, 845–853, DOI:10.1021/ar9901164.

[118] Roth, C.; Parschau, M.; Ernst, K.-H. Chiral Reconstruction of a Metal Surface by Adsorption of Racemic Malic Acid. *ChemPhysChem* **2011**, *12*, 1572–1577, DOI:10.1002/cphc.201000961.

[119] Roth, C.; Passerone, D.; Merz, L.; Parschau, M.; Ernst, K.-H. Two-Dimensional Self-Assembly of Chiral Malic Acid on Cu(110). *J. Phys. Chem. C* **2011**, *115*, 1240–1247, DOI:10.1021/jp106575g.
[120] Hildreth, O. J.; Fedorov, A. G.; Wong, C. P. 3D Spirals with Controlled Chirality Fabricated Using Metal-Assisted Chemical Etching of Silicon. *ACS Nano* **2012**, *6*, 10004–10012, DOI:10.1021/nn303680k.
[121] Baddeley, C. J.; Richardson, N. V. Chirality at Metal Surfaces. In *Scanning Tunneling Microscopy in Surface Science, Nanoscience and Catalysis*; WILEY-VCH: Weinheim, 2010; pp. 1–27.
[122] Karageorgaki, C.; Passerone, D.; Ernst, K.-H. Chiral Reconstruction of Cu(110) after Adsorption of Fumaric Acid. *Surf. Sci.* **2014**, *629*, 75–80, DOI:10.1016/j.susc.2014.01.010.
[123] Wagner, C. D.; Davis, L. E.; Riggs, W. M. The Energy Dependence of the Electron Mean Free Path. *Surf. Interface Anal.* **1980**, *2*, 53–55, DOI:10.1002/sia.740020204.
[124] Appendix E: Parameter Tables of Crystals. In *Crystallography and Surface Structure*; Wiley-VCH Verlag GmbH & Co. KGaA: Weinheim, Germany, 2011; pp. 265–266.
[125] Hahn, E.; Kampshoff, E.; Fricke, A.; Bucher, J.-P.; Kern, K. Pseudomorphic Growth of Thin Cu Films on Pd(110). *Surf. Sci.* **1994**, *319*, 277–286, DOI:10.1016/0039-6028(94)90595-9.

# 12 Appendix

**Table 12.1:** Summary of the scanning tunnelling conductions of all the STM images in this thesis.

| Figure | Bias Voltage [V] | Current Set-Point [pA] | Temperature [K] |
|---|---|---|---|
| Figure 6.1a | -1.16 | - 130 | 298 |
| Figure 6.1 (inset) | 0.014 | 3000 | 298 |
| Figure 6.1b | -1.20 | - 420 | 298 |
| Figure 6.1c | -1.16 | - 70 | 298 |
| Figure 6.1d | -1.16 | - 170 | 298 |
| Figure 6.1e | -1.20 | - 380 | 298 |
| Figure 6.1f | -1.16 | - 330 | 298 |
| Figure 6.5a | -1.16 | - 130 | 298 |
| Figure 6.5b | -1.20 | - 420 | 298 |
| Figure 6.5c | -1.16 | - 90 | 298 |
| Figure 6.5d | -1.20 | - 90 | 298 |
| Figure 6.5e | -1.24 | - 210 | 298 |
| Figure 6.5f | -1.16 | - 100 | 298 |
| Figure 6.5g | -1.24 | - 90 | 298 |
| Figure 6.5h | -1.28 | - 80 | 298 |
| Figure 6.5i | -1.28 | - 80 | 298 |
| Figure 6.6a | -1.20 | - 90 | 298 |
| Figure 6.6b | -1.25 | - 100 | 298 |
| Figure 6.7a | -1.24 | - 120 | 298 |
| Figure 6.7b | -1.24 | - 90 | 298 |
| Figure 6.7c | -1.24 | - 160 | 298 |
| Figure 6.7d | -1.13 | - 380 | 298 |
| Figure 7.1a | -0.94 | - 100 | 298 |
| Figure 7.1b | -1.06 | - 90 | 298 |
| Figure 7.1c | -1.24 | - 100 | 298 |
| Figure 7.3a | -0.2 | - 220 | 298 |
| Figure 7.3b | -0.07 | - 1040 | 298 |
| Figure 7.5a | -1.06 | - 70 | 298 |
| Figure 7.5b | -1.16 | - 70 | 298 |

| | | | |
|---|---|---|---|
| Figure 7.11a | -0.05 | –500 | 298 |
| Figure 7.11b | -1.03 | –90 | 298 |
| Figure 7.7a | -0.09 | –820 | 298 |
| Figure 7.7b | -1.13 | –130 | 298 |
| Figure 7.7c | -1.24 | –60 | 298 |
| Figure 7.7d | -1.03 | –110 | 298 |

# 13 List of Publications

Relevant for the thesis

2018 **Rieger, A**.; Sax, C.; Bauert, T.; Wäckerlin, C.; Ernst, K.-H. Chiral Molecules Adsorbed on a Solid Surface; Tartaric Acid Diastereomers and their Surface Explosion on Cu(111), *Chirality* **2018**, 1, 1-9 DOI: 10.1002/chir.22819.[113]

2017 **Rieger, A**.; Schnidrig, S.; Probst, B.; Ernst, K.-H.; Wäckerlin, C. Ranking the Stability of Transition-Metal Complexes by On-Surface Atom Exchange, *J. Phys. Chem. Lett.* **2017**, *24*, 6193-6198, DOI:10.1021/acs.jpclett.7b02834. [99]

2017 **Rieger, A**.; Schnidrig, S.; Probst, B.; Ernst, K.-H., Wäckerlin, C. Identification of On-Surface Reaction Mechanism by Targeted Metalation, *J. Phys. Chem. C* **2017**, *49*, 27521-27527, DOI:10.1021/acs.jpcc.7b10019. [82]

Previously published

2015 Uhl, A.; Fuchs, P.; **Rieger, A**.; Pianezzi, F.; Sutter-Fella, C.; Kranz, L.; Keller, D.; Hagendorfer, H.; Romanyuk, Y.; LaMattina, F.; Yoon, S.; Karvonen, L.; Magorian-Friedlmeier, T.; Ahlswede, E.; VanGenechten, D.; Stassin, F.; Tiwari, A. Liquid-Selenium-Enhanced Grain Growth of Nanoparticle Precursor Layers for $CuInSe_2$ Solar Cell Absorbers, *Prog. Photovolt: Res. Appl.* **2015**, *23*, 1110-1119, DOI: 10.1002/pip.2529

# 14 Curriculum Vitae

**Alexandra Rieger**

Birth: 10.08.1990, Zurich
Nationality: Swiss
Civil status: Married to Carlos Horn
Adress: Dörflistrasse 28
8192 Zweidlen
email: alexandra.rieger@adikom.ch

**2014 - 2018** PhD in molecular surface science at Empa Dübendorf. The focus of the study lies on interactions between metals and organic molecules with respect to the change of chemical and physical properties of either of the reagents when the metal attaches itself on the inside of a molecule or on the outside of it. These topics were investigated in ultra-high vacuum using scanning tunnelling microscopy (STM), X-ray absorption spectroscopy (XPS), X-ray photoelectron diffraction (XPD) and thermal desorption spectroscopy (TDS). All the experiments were performed in-house at Empa Dübendorf.

**2013 - 2014** Scientist at Functional Inorganic Materials group of Prof. Kovalenko at Empa Dübendorf investigating the changes of impedance in nanoparticle batteries over charging and discharging time.

**2012 - 2013** Master of Science, ETH Zurich

Focussing on functional inorganic chemistry

- Four months master thesis on "*Spray pyrolysis of* $In_2S_3$ *and ZnS buffer layers for thin film solar cells*", Prof. Tiwari, Abteilung für Dünnfilme und Photovoltaik, Empa Dübendorf

Spray pyrolysis of solutions containing Indium, Sulfur and Zinc precursors was investigated for its applicability as a replacement of the sputter process that is usually employed in scientific solar cell production for creating the mentioned buffer layers.

**2009 - 2012** Bachelor of Science, ETH Zurich

Focussing on electrochemistry and crystallography

- Three months of semester project focussing on nanoparticle batteries "*Tin oxide nanoparticles as anode materials for Lithium-ion battery application*", Prof. Kovalenko, Functional Inorganic Materials, Empa Dübendorf.

Tin oxide nanoparticles were investigated regarding their stability and overall reproducibility over a battery lifetime with many charging and discharging loops.

- Three months of semester project focussing on ambient pressure production of thin film solar cells*: "Rapid thermal processing of nanoparticle precursors for* $Cu(In,Ga)Se_2$ *solar cell absorbers*", Prof. Tiwari, Abteilung für Dünnfilme und Photovoltaik, Empa Dübendorf

A process was developed how thin film solar cells could be made using the new RTP machine giving the same homogeneity and efficiency as thin film solar cells made by sputter processes.

**2003 - 2009** Matura, language profile, bilingual classes (English and German), Kantonsschule Rhychenberg, Winterthur

# 15 Acknowledgements

Here, I would like to acknowledge and thank all the people who helped me during my doctoral thesis and supported my through this time.

First of all, I want to thank my professor Karl-Heinz Ernst for giving me the opportunity to conduct this work in his group. I am thankful of Christian Wäckerlin for his supervision, the discussions on scientific results and scientific writing. Ultra-high vacuum machines are prone to bugging, therefore I am grateful for the help and support that Sasa Vranjkovic and Manfred Parschau gave me.

For the time I spent in the Functional Polymers laboratory at Empa in the group of Frank Nüesch making organic solar cells I want to thank especially Roland Hany and Sandra Jenatsch for their explanations, their support and the scientific discussions we had.

The XPD experiments were conducted in the nanotech@surfaces group at Empa. I would like to thank Roland Widmer and Samuel Stolz for time they took to explain me the XPD method and the machine. I am thankful for the support of the technician Lukas Rotach because also ultra-high vacuum machines in other laboratories are prone to bugging. And I am grateful of Oliver Gröning for the explanations on the usage of the XPD analysis software.

I would also like to acknowledge the graduate school of chemical and molecular sciences at the University of Zurich (CMSZH) for the range of courses that I could attend as a student of this graduate school.

Special thanks go to the surface science group: Jingyi Li, Anaïs Mairena and Gitika Srivastava for the mutual help and encouragement, the funny lunch breaks and the good dinners. I also thank my husband, Carlos Horn, for the house, the help and support and especially for telling me not to take work too serious and I deeply thank my two cats, Mina und Luna, for mental support while writing this thesis.

CMSZH

CHEMICAL MOLECULAR SCIENCES ZURICH

GRADUATE SCHOOL